University of Alberta

Use of Diffusion Tensor Imaging Toward the Detection of Annulus Fibrosus Tears within the Cadaveric Porcine Intervertebral Disc

by

Jason Alexander Haynes Pearman

A thesis submitted to the Faculty of Graduate Studies and Research
in partial fulfillment of the requirements for the degree of

Master of Science

Department of Biomedical Engineering

Edmonton, Alberta
Fall 2007

Library and Archives Canada

Published Heritage Branch

395 Wellington Street
Ottawa ON K1A 0N4
Canada

Bibliothèque et Archives Canada

Direction du Patrimoine de l'édition

395, rue Wellington
Ottawa ON K1A 0N4
Canada

Your file Votre référence
ISBN: 978-0-494-33324-2
Our file Notre référence
ISBN: 978-0-494-33324-2

NOTICE:
The author has granted a non-exclusive license allowing Library and Archives Canada to reproduce, publish, archive, preserve, conserve, communicate to the public by telecommunication or on the Internet, loan, distribute and sell theses worldwide, for commercial or non-commercial purposes, in microform, paper, electronic and/or any other formats.

The author retains copyright ownership and moral rights in this thesis. Neither the thesis nor substantial extracts from it may be printed or otherwise reproduced without the author's permission.

AVIS:
L'auteur a accordé une licence non exclusive permettant à la Bibliothèque et Archives Canada de reproduire, publier, archiver, sauvegarder, conserver, transmettre au public par télécommunication ou par l'Internet, prêter, distribuer et vendre des thèses partout dans le monde, à des fins commerciales ou autres, sur support microforme, papier, électronique et/ou autres formats.

L'auteur conserve la propriété du droit d'auteur et des droits moraux qui protège cette thèse. Ni la thèse ni des extraits substantiels de celle-ci ne doivent être imprimés ou autrement reproduits sans son autorisation.

In compliance with the Canadian Privacy Act some supporting forms may have been removed from this thesis.

While these forms may be included in the document page count, their removal does not represent any loss of content from the thesis.

Conformément à la loi canadienne sur la protection de la vie privée, quelques formulaires secondaires ont été enlevés de cette thèse.

Bien que ces formulaires aient inclus dans la pagination, il n'y aura aucun contenu manquant.

Canada

"The scientific man does not aim at an immediate result. He does not expect that his advanced ideas will be readily taken up. His work is like that of a planter – for the future. His duty is to lay the foundation for those who are to come and point the way. He lives and labors and hopes."

~ Nikola Tesla

So what do I feel…? *Elation… Confidence… Anticipation… Nervousness… Panic… Relief… Reality… Astonishment… Gratefulness… All of these in one…* ***For those who soothed, for those who taught, for those who judged, for those who came before and showed the way****, thank you. Thank you for taking me under your wings and staying with me as I found my path.* ***Thank you lord for again*** *taking me into your care;* ***sending me lanterns to light the way…***

Abstract:

Introduction: This study sought to determine the sensitivity of Diffusion Tensor Imaging (DTI) to annular tears.

Methods: Tears were generated in porcine discs. Using a 1.5 Tesla Magnetic Resonance Imaging (MRI) unit, DTI and clinical scans were taken under two load conditions. A comparison of MRI sequence injury visualization, a quantitative comparison between tears and nucleus pulposus DTI data, and the effect of loading on injury detection were assessed.

Results: Using DTI maps, injuries were visualized significantly more often than with clinical sequences. A significant difference existed between the injury and nucleus DTI data. Dynamic loading increased injury detection in all sequences.

Conclusion: In cadaveric porcine discs, tears in the annulus are significantly more conspicuous using DTI than conventional MRI. Data from DTI can also differentiate these injuries from nuclear regions. Increased detection of injury through DTI could be used to evaluate correlations between annular tears and low back pain.

TABLE OF CONTENTS:

CHAPTER 1: INTRODUCTION.....1

1.1 BACKGROUND AND RATIONALE:.....1

Burdens of low back pain.....1

Causes of low back pain and the intervertebral disc.....2

The intervertebral disc.....2

Tears in the annulus fibrosus and low back pain.....3

1.2 CLINICAL ANNULUS FIBROSUS TEAR DETECTION: CURRENT TECHNIQUES AND THEIR DEFICIENCIES.....3

1.3 NEW MRI TECHNIQUES FOR IMAGING ANNULUS FIBROSUS TEARS: POSSIBILITIES AND LIMITATIONS.....5

Diffusion MRI.....5

Dynamic MRI.....5

Diffusion paired with dynamic MRI.....6

1.4 STATEMENT OF THE PROBLEM:.....7

1.5 OBJECTIVES:.....7

1.6 HYPOTHESES:.....8

1.7 LIMITATIONS:.....8

1.8 ETHICAL CONSIDERATIONS:.....9

1.9 SIGNIFICANCE OF THE STUDY:.....9

CHAPTER 2: LITERATURE REVIEW.....15

2.1 ANATOMY OF THE INTERVERTEBRAL DISC:.....15

Nucleus pulposus.....16

Annulus fibrosus.....18

Cartilage endplate.....21

2.2 FUNCTION OF THE INTERVERTEBRAL DISC:.....21

Mechanical Systems:.....22

Hydrostatic System:.....25

2.3 INJURY TO THE INTERVERTEBRAL DISC:.....28

AGEING AND DEGENERATION 29
Tears of the annulus fibrosus 31
Injury models 33
2.4 MRI DETECTION OF INTERVERTEBRAL DISC TEARS: 33
Annulus Fibrosus tear detection 34
MRI contrast basics 34
Clinical MRI protocol of the IVD 39
Clinical AF tear detection - deficiencies 41
2.5 IMPROVING TEAR DETECTION USING MRI: 42
Magic angle 43
Ultra Short TE 43
Quantitative T2 44
2.6 FUNCTIONAL AF TEAR DETECTION: 44
Diffusion MRI basics 45
Apparent Diffusion Coefficient maps 46
The Diffusion tensor 47
2.7 DIFFUSION MRI OF THE IVD: 48
Challenges regarding the use of Diffusion MRI 50
Echo Planar Imaging 51
Parallel Imaging (SENSE) 52
2.8 DYNAMIC MRI: 55
2.9 LITERATURE REVIEW SUMMARY: 56
CHAPTER 3: RESEARCH METHODS 67
3.1 GENERAL METHODS: 67
Specimen retrieval 67
Sample preparation 68
Specimen mounting for MRI 69
Imaging hardware 69
Tissue storage 70
Anatomical sections for dye enhanced visualization 70

Tissue disposal 70
3.2 Preliminary Experimentation: 71
3.2.1 Pneumatic injury and preliminary selection of imaging sequences: 71
3.2.2 Stab injury, continued selection and refinement of imaging protocol: 77
3.2.3 Radial cores with MRI sequence refinement, synchronization, and inclusion of loading protocol 79
3.3 Final thesis study: conventional MRI versus DTI injury visualization of 2mm core and 12GA stab injuries, without and with dynamic loading 87
Qualitative injury visualization analysis 90
Quantitative injury visualization analysis 92
CHAPTER 4: RESULTS 94
4.1 Study specimens: 95
4.2 Qualitative injury visualization analysis: 95
Qualitative results 96
4.3 Quantitative injury visualization analysis: 101
Descriptive statistics 103
Statistical analysis considerations: 106
Quantitative results 107
2mm core versus 12GA stab injury 118
CHAPTER 5: DISCUSSION 126
5.1 Hypothesis 1: 126
Comparison to other literature 127
Discussion 129
5.2 Hypothesis 2: 132
Comparison to other literature 133
Discussion 135
5.3 Hypothesis 3 138
Qualitative Results: 138

Comparison to other literature 139
Discussion 140
Quantitative Results 141
Comparison to other literature 143
Discussion 144
5.4 Strengths and weaknesses 147
Strengths: 147
Weaknesses: 148
5.5 Clinical Potential / Research Significance 149
CHAPTER 6: CONCLUSION 153
6.1 Hypothesis One 153
6.2 Hypothesis Two 154
6.3 Hypothesis Three 154
6.4 Thesis recommendation 155
6.5 Thesis relevance 156
6.6 Directions for the future 156

Appendix A: Ethics Protocols 158
Appendix B: Pther531 Directed Study Final Report 163
Appendix C: Experimental and Imaging Protocols 179
Appendix D: Example of Results from Imaging Protocol of One IVD 182
Appendix E: Final Results ("on" slices) from Imaging Protocol 188
Appendix F: Diffusion Weighting and Contrast to Noise Measurements 201
Appendix G: Statistical Considerations for Quantitative Analysis 209

List of tables:

Table 1. Example of relaxation times for various tissues. Single * denotes T1 and T2 relaxation times from Chiu *et al.* (Chiu *et al.*, 2001), the remainder of relaxation times are from http://en.wikibooks.org/wiki/Basic_Physics_of_Nuclear_Medicine/MRI_&_Nuclear_Medicine). 36

Table 2. Experiment 1 imaging protocol. 72

Table 3. Experiment 2 imaging protocol. 78

Table 4. Experiment 3 imaging protocol. 85

Table 5. Final experiment imaging protocol, beginning with DTI-mSense IPat sequence. 90

Table 6. Combined "on" and "off" slice injury visualization for each MRI category. A single * denotes injury observation significantly less than DTI sequences for a given injury and load condition. A double ** denotes a significant increase in injury observation with dynamic loading for an individual MRI category. Significance is at the $p < 0.05$ level. 96

Table 7. Visual observation of the 2mm core injury with axial MRI scans (clinical, proton density and DTI). Each row of the table corresponds to a common MRI slice shared by each of the axial MRI sequences. Absolute number and percentage of successful injury observations are reported for each MRI category. A single * denotes injury observation significantly less than DTI sequences for a given slice plane. Significance is at the $p < 0.05$ level. 97

Table 8. Visual observation results of 12GA stab injury on axial MRI scans (clinical, proton density and DTI). Each row of the table corresponds to a common MRI slice shared by each of the axial MRI sequences. Absolute number and percentage of successful injury observations are reported for each MRI category. A single * denotes injury observation significantly less than DTI sequences for a given slice plane. Significance is at the $p < 0.05$ level..... 98

Table 9. Visual observation results of 2mm core injury with compressive load on axial MRI scans (clinical, proton density and DTI). Each row of the table corresponds to a common MRI slice shared by each of the axial MRI sequences. Absolute number and percentage of successful injury observations are reported for each MRI category. A single * denotes injury observation significantly less than DTI sequences for a given slice plane. A double ** denotes significant increase in injury observation with dynamic loading for an individual MRI category. Significance is at the $p < 0.05$ level. 100

Table 10. Visual observation results of 12GA stab injury with compressive load on axial MRI scans (clinical, proton density and DTI). Each row of the table corresponds to a common MRI slice shared by each of the axial MRI sequences. Absolute number and percentage of successful injury observations are reported for each MRI category. A single * denotes injury observation significantly less than DTI sequences for a given slice plane. A double ** denotes significant increase in injury observation with dynamic loading for an individual MRI category (no significant difference in detection with loading observed). Significance is at the $p < 0.05$ level..... 101

Table 11. Summary of no load and load results from the 2x5 MANOVA of 2mm core – NP, and 12GA stab - NP DTI data. A single * denotes a significant difference between the DTI measures of the injury and NP ROIs, a double ** denotes a significant difference between DTI measures of the "on" and "off" injury Slice Planes (no significant difference between averages with loading observed), and a triple *** is for a significant interaction between the ROI and Slice Plane factors. Significance was considered to be at the $p < 0.05$ levels. 102

Table 12. Summary of no load and load results from the 2x5 MANOVA of the 2mm core – 12GA stab DTI data. A single * denotes a significant difference between the DTI measures of the injury ROIs, a double ** denotes a significant difference between DTI measures of the "on" and "off" injury Slice Planes, and a triple *** is for a significant interaction between the ROI and Slice Plane factors. Significance was considered to be at the $p < 0.05$ levels..... 102

TABLE 13. DESCRIPTIVE STATISTICS FOR DTI MEASURES FROM 2MM CORE, 12GA STAB INJURIES, AND NP ROIS. 104
TABLE 14. DESCRIPTIVE STATISTICS FOR DTI MEASURES FROM 2MM CORE, 12GA STAB INJURIES, AND NP ROIS UNDER LOAD CONDITIONS. 105
TABLE 15. OVERALL TESTS OF UNIVARIATE MODELS FOR FIXED EFFECTS MANOVA OF DTI VALUES FOR 2MM CORE INJURY AND NP ROIS; "ON" AND "OFF" SLICE PLANES. A SINGLE * DENOTES A SIGNIFICANT FACTOR AT THE $P < 0.05$ LEVEL. 107
TABLE 16. TESTS OF UNIVARIATE EFFECTS FOR FIXED EFFECTS MANOVA OF DTI VALUES FOR 2MM CORE INJURY AND NP ROIS; "ON" AND "OFF" SLICE PLANES. A SINGLE * DENOTES SIGNIFICANCE AT THE $P < 0.05$ LEVEL. 108
TABLE 17. OVERALL TESTS OF UNIVARIATE MODELS FOR FIXED EFFECTS MANOVA OF DTI VALUES FOR 12GA STAB INJURY AND NP ROIS; "ON" AND "OFF" SLICE PLANES. A SINGLE * DENOTES A SIGNIFICANT FACTOR AT THE $P < 0.05$ LEVEL. 110
TABLE 18. TESTS OF UNIVARIATE EFFECTS FOR FIXED EFFECTS MANOVA OF DTI VALUES FOR 12GA STAB INJURY AND NP ROIS; "ON" AND "OFF" SLICE PLANES. A SINGLE * DENOTES SIGNIFICANCE AT THE $P < 0.05$ LEVEL. 111
TABLE 19. OVERALL TESTS OF UNIVARIATE MODELS FOR FIXED EFFECTS MANOVA OF DTI VALUES FOR 2MM CORE INJURY AND NP ROIS; "ON" AND "OFF" SLICE PLANES UNDER PHYSIOLOGICAL LOADING CONDITIONS. A SINGLE * DENOTES A SIGNIFICANT FACTOR AT THE $P < 0.05$ LEVEL. 113
TABLE 20. TESTS OF UNIVARIATE EFFECTS FOR FIXED EFFECTS MANOVA OF DTI VALUES FOR 2MM CORE INJURY AND NP ROIS; "ON" AND "OFF" SLICE PLANES UNDER PHYSIOLOGICAL LOADING. A SINGLE * DENOTES SIGNIFICANCE AT THE $P < 0.05$ LEVEL. 114
TABLE 21. OVERALL TESTS OF UNIVARIATE MODELS FOR FIXED EFFECTS MANOVA OF DTI VALUES FOR 12GA STAB INJURY AND NP ROIS; "ON" AND "OFF" SLICE PLANES UNDER PHYSIOLOGICAL LOADING CONDITIONS. A SINGLE * DENOTES A SIGNIFICANT FACTOR AT THE $P < 0.05$ LEVEL. 116
TABLE 22. TESTS OF UNIVARIATE EFFECTS FOR FIXED EFFECTS MANOVA OF DTI VALUES FOR 12GA STAB INJURY AND NP ROIS; "ON" AND "OFF" SLICE PLANES UNDER PHYSIOLOGICAL LOADING. A SINGLE * DENOTES SIGNIFICANCE AT THE $P < 0.05$ LEVEL. 117

TABLE 23. OVERALL TESTS OF UNIVARIATE MODELS FOR FIXED EFFECTS MANOVA OF DTI VALUES FOR 2MM CORE AND 12GA STAB INJURY ROIS; "ON" AND "OFF" SLICE PLANES. A SINGLE * DENOTES A SIGNIFICANT FACTOR AT THE $P < 0.05$ LEVEL. 119

TABLE 24. TESTS OF UNIVARIATE EFFECTS FOR FIXED EFFECTS MANOVA OF DTI VALUES FOR 2MM CORE AND 12GA STAB INJURY ROIS; "ON" AND "OFF" SLICE. A SINGLE * DENOTES SIGNIFICANCE AT THE $P < 0.05$ LEVEL. 120

TABLE 25. OVERALL TESTS OF UNIVARIATE MODELS FOR FIXED EFFECTS MANOVA OF DTI VALUES FOR 2MM CORE AND 12GA STAB INJURY ROIS; "ON" AND "OFF" SLICE PLANES UNDER PHYSIOLOGICAL LOADING CONDITIONS. A SINGLE * DENOTES A SIGNIFICANT FACTOR AT THE $P < 0.05$ LEVEL. 122

TABLE 26. TESTS OF UNIVARIATE EFFECTS FOR FIXED EFFECTS MANOVA OF DTI VALUES FOR 2MM CORE AND 12GA STAB INJURY ROIS; "ON" AND "OFF" SLICE PLANES UNDER PHYSIOLOGICAL LOADING. A SINGLE * DENOTES SIGNIFICANCE AT THE $P < 0.05$ LEVEL. 123

TABLE 27. PERCENTAGE OF RADIAL TEAR DETECTION. CONVENTIONAL MRI RADIAL TEAR DETECTION REPORTED FROM A NUMBER OF STUDIES COMPARED TO THE DTI AND CONVENTIONAL MRI DETECTION RATES FROM THIS STUDY. 128

TABLE 28. EIGENVALUES (MM^2/S) FOR THE NP FROM DREW *ET AL.* (DREW ET AL., 2004), CHIU *ET AL.* (CHIU ET AL., 2001), AND THIS STUDY. 134

TABLE 29. DTI MEANS FROM EXPERIMENT 4, FOR THE 2MM CORE, 12GA STAB, AND NP. NO LOAD. 136

TABLE 30. EIGENVALUES (MM^2/S) FOR THE NP FROM CHIU *ET AL.* (CHIU ET AL., 2001). DYNAMIC LOAD CONDITIONS. 143

TABLE 31. DTI MEANS FROM EXPERIMENT 4, FOR THE 2MM CORE, 12GA STAB, AND NP. DYNAMIC LOADING. 146

List of figures:

Figure 1. The major structures of the spine surrounding the IVD, including an axial view that describes the arrangement of the NP and AF (image from www.wolfhouse.dk/articles/images/img_fce_figure1.jpg) 16

Figure 2. Anatomical observation of NP denoted by arrow in the sagittal plane (Yu et al., 2003). 16

Figure 3. Anatomical observation of NP denoted by arrow in the transverse plane (Yu et al., 2003). 17

Figure 4. A section of NP depicted as containing proteoglycan aggregates entrapped in a collagen fiber network. Proteoglycan aggregates are (dashed line) replaced with aggrecan molecules possessing a central core protein (open line) and glycosaminoglycan side chains (solid lines). The hydration properties of the glycosaminoglycan chains of aggrecan cause the tissue to swell until an equilibrium is reached, in which the swelling potential is balanced by tensile forces in the collagen network (Adams and Roughley, 2006). 18

Figure 5. Mid-sagittal section of cadaveric IVD showing NP and distinct radial layers of the AF. The transition zone of the AF is the portion interfacing with the NP (A), and the inner AF constitutes the middle portion of the entire AF (B), while the outer AF is the portions furthest away from the NP (C) (Adams and Roughley, 2006) 19

Figure 6. An in plane representation of the collagen fibre bundles comprising a length of lamella (Marchand and Ahmed, 1990). 20

Figure 7. A circumferential section of AF with alternating fibre angles of α = approximately 30°(Adams and Roughley, 2006) 20

Figure 8. The stress, strains and hydrostatic pressure distribution of longitudinal compression forces (Setton and Chen, 2006) 22

Figure 9. Structures in motion unit that deform to facilitate movement. A) Anterior longitudinal ligament and AF, B) apophyseal joint, C) facet capsulary ligament, D) posterior longitudinal ligament (Adams and Dolan, 2005). 23

Figure 10. Circumferential tension or 'hoop stress' maintains containment of the NP (Adams and Dolan, 2005). 24

FIGURE 11. THE CORRELATION BETWEEN WATER CONTENT AND DIRECTIONAL PERMEABILITY (GU ET AL., 1999). 27

FIGURE 12. STRESS CONCENTRATION CHANGES DUE TO ABNORMAL DISCS (POLLINTINE ET AL., 2004). 30

FIGURE 13. RADIAL TEAR WITH AXIAL AND SAGITTAL REPRESENTATIONS. WHITE BEING THE AF, BLACK BEING THE DISRUPTED TISSUE, AND GREY BEING THE NP (ADAMS AND ROUGHLEY, 2006). 31

FIGURE 14. CIRCUMFERENTIAL TEAR WITH AXIAL AND SAGITTAL REPRESENTATIONS. WHITE BEING THE AF, BLACK BEING THE DISRUPTED TISSUE, AND GREY BEING THE NP (ADAMS AND ROUGHLEY, 2006). 32

FIGURE 15. TRANSVERSE TEAR WITH AXIAL AND SAGITTAL REPRESENTATIONS. WHITE BEING THE AF, BLACK BEING THE DISRUPTED TISSUE, AND GREY BEING THE NP (ADAMS AND ROUGHLEY, 2006) 32

FIGURE 16. TRANSVERSE (MXY) AND LONGITUDINAL (MZ) MAGNETIZATIONS ABOUT THE STATIC FIELD AXIS (IMAGE FROM HTTP://EN.WIKIBOOKS.ORG/WIKI/IMAGE.EXCITATION3_1.JPG) 35

FIGURE 17. T2 WEIGHTED (T2W) (TOP) AND T1 WEIGHTED (T1W) (BOTTOM) MRI CONTRAST GENERATING SCHEMES BETWEEN 2 DIFFERENT TISSUES (TISSUE A, TISSUE B). DIFFERENT LEVELS OF CONTRAST GENERATION BETWEEN TISSUES A AND B ARE ACHIEVED BY SAMPLING SIGNALS AT DIFFERENT TES (MS) DENOTED AS T2 (ORANGE) AND T2 (YELLOW), T1 (RED) AND T1 (MAROON) (IMAGES FROM HTTP://WWW.E-MRI.ORG/COURS/MODULE_4_SIGNAL/T2.GIF). 37

FIGURE 18. 2 CANINE SPECIMEN IMAGED 15 DAYS FOLLOWING STAB INJURY AND NUCLEAR MATERIAL EXTRACTION (TOP AND BOTTOM ROWS). THE IMAGING PROTOCOL INCLUDED T1W (500 MSEC TR, 20MSEC TE, 2AVG) (A), T1W FOLLOWING CONTRAST INJECTION (B), T2W SCAN (2000 MSEC TR, 88MSEC TE, 2AVG) (C). NO CHANGE FROM BASELINE FOR THE FIRST ANIMAL, NOTICEABLE CHANGE THROUGH HIZ VISUALIZATION IN THE SECOND ANIMAL IDENTIFIED BY ARROWS (NGUYEN-MINH ET AL., 1997). 40

FIGURE 19. DIFFUSION GRADIENTS AND PHASE ACCUMULATION OF MOVING PROTONS (IMAGE FROM HTTP://WWW.RSIERRA.COM/DA/) 45

FIGURE 20. COMPARISON OF A PROTON DENSITY WITH DIFFUSION WEIGHTED MRI AND ADC VISUALIZATION OF ISCHEMIC STROKE (THOMAS ET AL., 2000). 47
FIGURE 21. *IN SITU* SAMPLE OF AF IMAGED USING DWI AT 7.1T MAGNET. ABLE TO GENERATE DTI SET FOR DIFFUSION DIRECTION INFORMATION (HSU AND SETTON, 1999).. 49
FIGURE 22. EPI GRADIENT SCHEME. BETWEEN MULTIPLE READOUTS PHASE ENCODES ALLOW SIGNAL TO BE STEPPED THROUGH K-SPACE (IMAGE FROM HTTP.//BITC.BME.EMORY.EDU/IMAGES/EPI_PT_1.JPG). 52
FIGURE 23. AN EXAMPLE OF A 4 CHANNEL SPINAL ARRAY WHERE EACH COIL ACQUIRED A PARTIAL DATA SET WHICH WAS USED TO CONSTRUCT THE FINAL IMAGE ON A PIXEL BY PIXEL BASIS (LARKMAN AND NUNES, 2007). 54
FIGURE 24. THE USE OF SENSE ENCODING FURTHER IMPROVED ON THE UNIQUE ADVANTAGES OF APPLYING EPI TO DIFFUSION-WEIGHTED SEQUENCE. A) CONVENTIONAL EPI DIFFUSION PULSE SEQUENCE. B) ALTERED SEQUENCE FOR SENSE APPLICATION. THE EPI ECHO TRAIN IS FURTHER REDUCED WITH SENSE AND A MUCH SHORTER TE FOR A GIVEN DIFFUSION ATTENUATION IS POSSIBLE. (BAMMER ET AL., 2002) 55
FIGURE 25. LUMBAR SPINE SEGMENTS HARVESTED *EN BLOCK* FROM 200KG SOW (LEFT), AND SEGMENT FOLLOWING SPECIMEN PREPARATION PRIOR TO SPECIMEN MOUNTING (RIGHT)... 68
FIGURE 26. POTS (ARROWS) FIXED TO SPINE SEGMENT IN LOADING RIG FIXTURES. IMAGE IS FROM FINAL EXPERIMENT. 69
FIGURE 27. ANATOMICAL SECTION SHOWING INJURIES FROM FINAL EXPERIMENT. 70
FIGURE 28. SCREEN SHOT OF THE INJURED IVD SLICE (B0) AND MRVISION'S ROI MEASUREMENT TOOL GENERATING AN SI PROFILE FROM PLACEMENT OF THE 'LINE ROI' ACROSS THE ANTERIOR AF. POSITIONS A, B, C REFLECT USG, AF, AND AF INJURY SI ALONG THE LINE ROI. IMAGE IS FROM FINAL EXPERIMENT. 74
FIGURE 29. SCREEN SHOT OF B0 AND 6 DWIS FROM THE SAME SLICE PRIOR TO BEING FITTED TO THRESHOLD ADC MAPS USING MRVISION'S IMAGE FITTING TOOL. IMAGE IS FROM FINAL EXPERIMENT. 75
FIGURE 30. AXIAL HIRESAXT2, AND DTI (FA AND TRACEADC) MAPS OF PNEUMATIC INJURY WHERE CATHETER TIP CAME TO REST IN NP VERSUS THE AF. 76

Figure 31. Axial HiResAxT2, and optimized (Threshold at 52SI) DTI (FA and TraceADC) maps of stab injury (white arrow) where injury propagates diagonally through AF and NP. 79
Figure 32. MRI safe rig used by Oliphant et al. (Oliphant, Frayne, & Kawchuk, 2005) (left), and 8-channel head coil (right). 80
Figure 33. The modified loading rig. 82
Figure 34. Pressure sensor and load cell calibration curve from final experiment, with curve equation (y) and coefficient of determination (R^2). 83
Figure 35. Wooden spine attached to specimen, with glass plugs in guides. The three different plug sizes are displayed on top of wooden spine. 84
Figure 36. Axial HiResAxT2, and optimized (Threshold at 80SI) DTI (FA and TraceADC) maps of 5mm (centre left) and 2mm (centre right) core injuries. Injury propagates anterior-posterior through AF and NP. Drill press drilled further than called for in experimental protocol for 5mm core injury. 86
Figure 37. Cross-section of IVD showing progressive schematic of injury protocol. The top two panels describe 2mm core injury generation, and the bottom two panels relate to the 12GA stab injury protocol. The position of the two injuries alternated between adjacent IVDs. A) Small gauge needle advances through the IVD. B) Bead is advanced over the protruding needle and glued to the posterior IVD tissue. C) 2mm core from the AF is taken. D) Second bead is glued above injury site. E) 12GA puncture needle is inserted diagonally through the IVD. F) Beads are glued to the entrance and exit wounds of the stab injury. Background IVD image from Adams *et al.* (2005) (Adams and Dolan, 2005)..... 88
Figure 38. Thesholded (64 SI) TraceADC map (left), with 2mm core injury ROI boundary (right). 92
Figure 39. Final experiment's axial imaging protocol, "on" slice. 2mm core injury left of centre, and 12GA stab right of centre. Clinical (A), proton density (B) sequences, and DTI maps (C) were scored as having positive 2mm core injury visualization (left arrow). Only DTI maps (C) were scored as having positive 12GA visualization (right arrow). 97

FIGURE 40. DIFFUSION TENSOR RESULTS FOR 2MM CORE INJURY AND NP WITH STANDARD ERROR BARS. TRACEADC AND EIGENVALUEVALUES 1, 2 AND 3 ARE IN UNITS OF MM^2 /SEC, AND FRACTIONAL ANISOTROPY IS A RATIO BETWEEN 1 AND 0. A SINGLE * DENOTES A SIGNIFICANT DIFFERENCE BETWEEN THE DTI MEASURES OF THE INJURY AND NP ROIS, A DOUBLE ** DENOTES A SIGNIFICANT DIFFERENCE BETWEEN THE SLICE PLANES OF EACH INDIVIDUAL ROI, AND A TRIPLE *** DENOTES A SIGNIFICANT INTERACTION BETWEEN THE ROI AND SLICE PLANE FACTORS. SIGNIFICANCE WAS CONSIDERED TO BE AT THE $p < 0.05$ LEVEL. 109

FIGURE 41. DIFFUSION TENSOR RESULTS FOR 12GA STAB INJURY AND NP WITH STANDARD ERROR BARS. TRACEADC AND EIGENVALUEVALUES 1, 2 AND 3 ARE IN UNITS OF MM^2 /SEC, AND FRACTIONAL ANISOTROPY IS A RATIO BETWEEN 1 AND 0. A SINGLE * DENOTES A SIGNIFICANT DIFFERENCE BETWEEN THE DTI MEASURES OF THE INJURY AND NP ROIS, A DOUBLE ** IS SIGNIFICANT DIFFERENCE BETWEEN THE SLICE PLANES OF EACH INDIVIDUAL ROI, AND A TRIPLE *** IS FOR A SIGNIFICANT INTERACTION BETWEEN THE ROI AND SLICE PLANE FACTORS. SIGNIFICANCE WAS CONSIDERED TO BE AT THE $p < 0.05$ LEVEL..... 112

FIGURE 42. DIFFUSION TENSOR RESULTS FOR 2MM CORE INJURY AND NP UNDER LOADING CONDITIONS, WITH STANDARD ERROR BARS. TRACEADC AND EIGENVALUEVALUES 1, 2 AND 3 ARE IN UNITS OF MM^2 /SEC, AND FRACTIONAL ANISOTROPY IS A RATIO BETWEEN 1 AND 0. A SINGLE * DENOTES A SIGNIFICANT DIFFERENCE BETWEEN THE DTI MEASURES OF THE INJURY AND NP ROIS, A DOUBLE ** IS SIGNIFICANT DIFFERENCE BETWEEN THE SLICE PLANES OF EACH INDIVIDUAL ROI, AND A TRIPLE *** IS FOR A SIGNIFICANT INTERACTION BETWEEN THE ROI AND SLICE PLANE FACTORS. SIGNIFICANCE WAS CONSIDERED TO BE AT THE $p < 0.05$ LEVEL. 115

FIGURE 43. DIFFUSION TENSOR RESULTS FOR 12GA STAB INJURY AND NP UNDER LOADING CONDITIONS, WITH STANDARD ERROR BARS. TRACEADC AND EIGENVALUEVALUES 1, 2 AND 3 ARE IN UNITS OF MM^2 /SEC, AND FRACTIONAL ANISOTROPY IS A RATIO BETWEEN 1 AND 0. A SINGLE * DENOTES A SIGNIFICANT DIFFERENCE BETWEEN THE DTI MEASURES OF THE INJURY AND NP ROIS, A DOUBLE ** IS SIGNIFICANT DIFFERENCE BETWEEN THE SLICE PLANES OF EACH INDIVIDUAL ROI, AND A TRIPLE *** IS FOR A SIGNIFICANT INTERACTION BETWEEN THE ROI AND SLICE PLANE FACTORS. SIGNIFICANCE WAS CONSIDERED TO BE AT THE $p < 0.05$ LEVEL. 118

FIGURE 44. DIFFUSION TENSOR RESULTS FOR 2MM CORE AND 12GA STAB INJURIES WITH STANDARD ERROR BARS. TRACEADC AND EIGENVALUEVALUES 1, 2 AND 3 ARE IN UNITS OF MM^2 /SEC, AND FRACTIONAL ANISOTROPY IS A RATIO BETWEEN 1 AND 0. A SINGLE * DENOTES A SIGNIFICANT DIFFERENCE BETWEEN THE DTI MEASURES OF THE INJURY AND NP ROIS, A DOUBLE ** IS SIGNIFICANT DIFFERENCE BETWEEN THE SLICE PLANES OF EACH INDIVIDUAL ROI, AND A TRIPLE *** IS FOR A SIGNIFICANT INTERACTION BETWEEN THE ROI AND SLICE PLANE FACTORS. SIGNIFICANCE WAS CONSIDERED TO BE AT THE $p < 0.05$ LEVEL 121

FIGURE 45. DIFFUSION TENSOR RESULTS FOR 2MM CORE AND 12GA STAB INJURIES UNDER LOAD CONDITIONS, WITH STANDARD ERROR BARS. TRACEADC AND EIGENVALUEVALUES 1, 2 AND 3 ARE IN UNITS OF MM^2 /SEC, AND FRACTIONAL ANISOTROPY IS A RATIO BETWEEN 1 AND 0. A SINGLE * DENOTES A SIGNIFICANT DIFFERENCE BETWEEN THE DTI MEASURES OF THE INJURY AND NP ROIS, A DOUBLE ** IS SIGNIFICANT DIFFERENCE BETWEEN THE SLICE PLANES OF EACH INDIVIDUAL ROI, AND A TRIPLE *** IS FOR A SIGNIFICANT INTERACTION BETWEEN THE ROI AND SLICE PLANE FACTORS. SIGNIFICANCE WAS CONSIDERED TO BE AT THE $p < 0.05$ LEVEL. 124

FIGURE 46. SIGNIFICANT INTERACTION BETWEEN ROI AND SLICE PLANE FOR THE EIGENVALUE 1 DATA OF THE 2MM CORE AND NP ROIS 133

FIGURE 47. SIGNIFICANT INTERACTION BETWEEN ROI AND SLICE PLANE FOR TRACEADC DATA OF INJURIES AND NP DURING COMPRESSIVE LOADING 142

FIGURE 48. SIGNIFICANT INTERACTION BETWEEN ROI AND SLICE PLANE FOR THE EIGENVALUE 3 FOR 2MM CORE AND NP ROIS DURING COMPRESSIVE LOADING 142

LIST OF EQUATIONS:

$A = A_0 e^{-D\gamma^2 G^2 \delta^2 (\Delta - \delta/3)}$ (1) 46

$A = A_0 e^{-bD}$ (2) 46

$\ln \frac{S(TE,b)}{S(TE,0)} = -bD$ (3) 46

LIST OF ABBREVIATIONS:

LBP – Low back pain

AF – Annulus fibrosus

IVD – Intervertebral disc

MRI – Magnetic resonance imaging

NP – Nucleus pulposus

RF – Radio-frequency

SNR – Signal to Noise ratio

DTI – Diffusion tensor imaging

CSF – Cerebrospinal fluid

HIZ – High intensity zone

FOV – Field of view

T2W – Transverse relaxation rate weighted scan

T1W – Longitudinal relaxation rate weighted scan

PFG – Pulse field gradient

USG – Ultrasound contrast gel

SI – Signal intensity

MANOVA - multivariate analysis of variance

Chapter 1: Introduction

Overview

Low back pain (LBP) is a disease with significant personal and societal costs (Gray et al., 2003, Luo et al., 2004). One explanation for these costs is that a definitive cause of LBP has yet to be identified. Although not yet confirmed, tears in the annulus fibrosus (AF) of the intervertebral disc (IVD) have been speculated to be contributors to LBP as well as potential initiators of disc degeneration (Kakitsubata et al., 2003, Munter et al., 2002, Yu et al., 2003). At present, the diagnosis of IVD tearing is dependent on medical imaging that can visualize only the largest of anatomical tears (Kakitsubata et al., 2003, Morgan and Saifuddin, 1999, Videman and Nurminen, 2004). One possible way to better diagnose IVD tears is to utilize novel magnetic resonance imaging (MRI) protocols that move beyond imaging anatomical structures, and instead visualize structural function (Dong et al., 2004, Malko, Hutton, & Fajman, 1999). These techniques include diffusion MRI, a well-developed tool that permits visualization of fluid diffusion within tissues (Bammer and Fazekas, 2003, Rowley, Grant, & Roberts, 1999), and dynamic MRI, which introduces physiological movement during imaging (Vedi et al., 1999). Given this background, this thesis has been designed to assess the sensitivity of diffusion MRI in recognizing tears in the AF. By comparing the AF tear sensitivities of diffusion and conventional MRI, then comparing these same techniques with the addition of dynamic loading, it may be possible to develop new diagnostic techniques capable of characterizing IVD function.

1.1 *Background and rationale:*

Burdens of low back pain

The incidence of LBP in the adult population has been reported to be as high as 80% (Andersson, 1997). Of those, 15% to 20% are expected to experience a reoccurrence within a year (Andersson, 1997). This incidence, in part, has resulted in enormous LBP health care expenditures, which have reached as high as $90.7 billion per year in the

United States alone. These costs make LBP one of the most expensive health conditions in North America (Luo et al., 2004). Included in these costs are significant expenses related to spinal imaging which may surpass $300 USD per MRI LBP investigation (Gray et al., 2003). The diagnostic yield from clinical imaging techniques is low (Gilbert et al., 2004b), and limited treatment options following injury detection, as well as large asymptomatic populations, continue to generate questions regarding the value of IVD imaging (Gilbert et al., 2004a, Gilbert et al., 2004b).

Causes of low back pain and the intervertebral disc

Only 15% of LBP cases can be attributed to a specific pathology (Jackson, 2004). This small percentage is associated typically with acute trauma such as overt fracture and/or neolastic processes (Jackson, 2004). The remaining 85% of LBP cases are of unknown origins, a situation that contributes to an abundance of theories about the causes of LBP. As a major functional component in the low back, the IVD is often implicated as a potential factor in the presence of LBP. This implication is a result of the IVD's role in facilitating the complex movements of the spine and dampening compressive loads (Asano et al., 1992, Wilke et al., 1999).

The intervertebral disc

Three main structures are what allow the IVD to perform its tasks. The nucleus pulposus (NP) is a uniformly gelatinous material at the centre of the IVD with a tremendous ability to bind with water. Because the AF and cartilaginous endplates encapsulate the NP, the healthy NP is under significant pressure. The presence of this high-pressured zone in the middle of the IVD is what creates enough room for adjacent vertebral structures to articulate (Brinkmann, Frobin, & Leivseth, 2002). The AF on the other hand facilitates IVD movement by redistributing the pressure emanating from the NP in radial directions (Asano et al., 1992, Haughton, Lim, & An, 1999). The AF also restricts the NP's ability to bulge in any one direction (Pollintine et al., 2004). Because the NP is under such high pressure, the multiple radial fibre layers that make up the AF exhibit considerable tensile strength (Brinkman, Frobin, & Leivseth, 2002). Finally, as the spine's shock absorber, axial compression induces fluid outflow from the NP. The endplates, which are fused to

the boney ends of vertebrae and attached to the AF and NP, serve as the major conduit for this fluid flow out of the IVD (Rajasekaran et al., 2004).

Tears in the annulus fibrosus and low back pain

Given the potential role of the IVD in LBP, and more specifically, the role of the AF in containing the NP under high pressure, defining the modes of AF failure is of great interest to scientists who study the causes of back pain. Radial, circumferential and transverse fissures are commonly found propagating across, or separating multiple fibre layers in the AF (Iatridis and Gwynn, 2004), and large examples of these types of failures are known as tears. The resulting type, size and location of these tears may have a considerable impact on the presence of pain (Morgan and Saifuddin, 1999, Munter et al., 2002), although the connection between tears and pain is neither understood nor absolute. Tears may weaken the AF (Iatridis and Gwynn, 2004) contributing to a reduction in the high-pressured environment of an otherwise healthy NP. This could result in joint instability, endplate failure, or in the worse case scenario, nerve root compression (Brinkman, Frobin, & Leivseth, 2002, Hickey and Hukins, 1980, Sasaki, 1995). Changes in the uniform pressure environment (Pollintine et al., 2004) of the NP may also alter its water content and matrix composition (Acaroglu et al., 1995). Therefore disruptions to the AF may intensify the normal IVD dehydration processes indicative of IVD degeneration (Kraemer, Kolditz, & Gowin, 1985, Masuda et al., 2005). Though IVD structural changes and degeneration are well detected by CT and MRI, tears within the AF have yet to be reliably diagnosed by either modality. This deficiency has led to difficulties in assessing the role tears have in IVD pathology and LBP (Gilbert et al., 2004b, Kakitsubata et al., 2003, Morgan and Saifuddin, 1999).

1.2 *Clinical annulus fibrosus tear detection: current techniques and their deficiencies*

As noted, medical imaging has allowed for the clinical detection of a number of IVD pathologies, with x-ray discography continuing to enjoy support as the gold standard for the detection of tears in the AF. In this procedure, iodinated contrast dye is injected into

the NP and then diffuses into existing tears in the AF. This technique yields excellent radial tear visualization with CT (Lander, 2005), but overall, AF tear detection is largely dependant on those injuries that propagate from the NP or epidural space (Kakitsubata et al., 2003, Osti and Fraser, 1992). Those tears that do not communicate with the NP are not visualized by discography. In contrast, MRI tear detection is being used more frequently to detect AF tears due to its noninvasive nature, its ability to visualize soft-tissue and the capacity to generate variable slice planes (Gilbert et al., 2004a, Haughton, 2004, Hensley, 1997). In this technique, material from the NP that migrates into the AF through tears, or excess fluid pooling in tears from the outer AF results in strong signal sources. This creates contrast because normal AF tissue exhibits very low signal in clinical MRI (Morgan and Saifuddin, 1999, Osti and Fraser, 1992). Unfortunately, like CT, the clinical reality remains; MRI detection of AF tears is dependant on large injuries that propagate from the NP or epidural space (Kakitsubata et al., 2003, Osti and Fraser, 1992). Clinicians are dependent on these MRI images to associate the onset of pain with AF damage (Gilbert et al., 2004a). This reality makes it especially difficult to study the mechanisms for AF failure and injury propagation (Munter et al., 2002), and the role of AF tears in IVD degeneration (Osti and Fraser, 1992) and LBP.

It has been suggested that asymptomatic low-grade AF injuries may develop into the larger detectable symptomatic tears (Fujita, Duncan, & Lotz, 1997, Videman et al., 2003), but the direct visualization of these low-grade injuries may be beyond the capabilities of clinical MRI. Because these small disruptions in the AF may still have significant impacts on AF function (Gu et al., 1999), alternatives to the visualization of anatomical structures are of interest. Two potential alternative MRI techniques include diffusion and dynamic MRI, and both generate contrast based on the functional properties of tissue structures.

1.3 *New MRI techniques for imaging annulus fibrosus tears: possibilities and limitations*

Diffusion MRI

Diffusion MRI capitalizes on the differences in diffusion characteristics between tissue structures by generating contrast in MRI based on varying levels of fluid diffusion within body tissues (Basser, 1995, Le Bihan, 1991). Initial clinical and research successes using diffusion MRI in the visualization of brain pathologies and brain structures have lead to an explosion of exploratory applications with other tissues (Rowley, Grant, & Roberts, 1999). Examples include the assessment of cardiac tissue viability following global ischemia (Collins et al., 2007), identification of normal diffusion characteristics in the human optic nerve for pathology detection (Wheeler-Kingshott et al., 2002), and the continued study of disease within the spinal cord (Holder, 2000).

It has been recognized that diffusion MRI may offer an excellent opportunity for improving the current state of AF tear detection (Haughton, 2004). Studies have been performed using diffusion MRI to describe quantitatively the fluid properties of healthy and degenerated IVDs. To date, these studies focused primarily on diffusion in the NP (Antoniou et al., 2004, Kealey et al., 2005, Kerttula et al., 2001). The most powerful form of diffusion MRI, diffusion tensor imaging (DTI), has successfully visualized healthy individual fibre layers of the AF at high magnetic fields (Hsu and Setton, 1999), but unfortunately, the results at these high fields are quite inconsistent with the quality of images available at clinical levels (Cihangiroglu et al., 2004) limiting the clinical applications for AF tear detection. Unlike the other diffusion MRI sequences, DTI yields directional information on the degree of water diffusion in addition to rotationally invariant quantitative data. These properties of DTI allow for the long-term comparison of data in a clinical environment (Dong et al., 2004, Rowley, Grant, & Roberts, 1999).

Dynamic MRI

Dynamic MRI improves the diagnostic capabilities of conventional MRI for the evaluation of structures in the body involved in some form of movement, through initiating functional movement during imaging (Chu et al., 2007, Hiwatashi et al., 2004,

Vedi et al., 1999). Compressive loading during MRI of the lumbar spine to evaluate spinal cord compression under loads is one such example (Hiwatashi et al., 2004).

The functional role of the IVD to manage compressive loads makes the IVD an ideal candidate for dynamic MRI. Recognizing this, a number of researchers have incorporated compressive loading into their MRI studies of healthy and injured spines (Hiwatashi et al., 2004, Kingma et al., 2000, Saifuddin, McSweeney, & Lehovsky, 2003, Yu et al., 2003). These studies have also focused on the NP as a region of interest for both quantitative measurements (Kingma et al., 2000, Yu et al., 2003), and anatomical responses to loads such as IVD height and outer AF bulging (Hiwatashi et al., 2004). One study in particular focused on the presence of AF tears and found that their visualization increased under loading conditions (Saifuddin, McSweeney, & Lehovsky, 2003). Unfortunately, it has already been described that conventional MRI visualization of IVD pathology has low diagnostic yield. Yet this observation demonstrates that a functional component may be required for AF tear detection. Recalling that fluid flows out of the NP during compression of the IVD, AF tears may induce a functional change in this process given adequate physiological loading. This has not yet been investigated via diffusion MRI measurements.

Diffusion paired with dynamic MRI

Given the above, there is real potential for the use of these alternative forms of MRI in the augmentation of existing conventional MRI IVD injury detection protocols. To date, diffusion MRI has provided insight into the fluid properties of the NP, and dynamic MRI has further added to that quantitative information through measurements taken during physiological conditions. Unfortunately, by focusing on the NP of healthy or degenerated IVDs, these studies stopped short of evaluating the potential contribution that diffusion and/or dynamic MRI could make to AF tear detection. Imaging at higher fields is one potential solution to boost signal availability in the AF for tear visualization, but dynamic loading at clinical magnet strengths may also improve signal availability through initiating fluid movement in the AF or by forcing nuclear material to migrate into low-level AF tears. Given adequate signal, DTI holds promise for AF tear detection,

treatment evaluation, and the further study of AF injury progression. Though there has been work published regarding diffusion MRI results from dynamic imaging studies (Chiu et al., 2001, Drew et al., 2004), DTI has only been utilized at stronger than clinical magnetic strengths, and the results from the AF were not reported due to poor signal levels in the AF (Drew et al., 2004).

1.4 *Statement of the problem:*

Current MRI protocols have been unable to consistently visualize sites that are presumed to be contributors to LBP. This situation creates uncertainty in diagnosis and treatment of LBP. Unlike conventional imaging, techniques that generate contrast based on tissue function (e.g. diffusion and dynamic MRI) offer promise in detecting annular injury.

1.5 *Objectives:*

The objectives of this thesis are as follows:

1. Determine if DTI maps improve MRI detection of artificial AF tears in the IVD of an excised porcine model.

2. Determine if DTI quantitative data can differentiate artificial AF tears from other regions in the IVD.

3. Determine if dynamic compression alters the sensitivity of DTI maps and DTI quantitative data to artificial AF tears in the IVD.

1.6 *Hypotheses:*

The following research hypotheses were derived from the available literature, and the experience of the author from earlier pilot work:

1. DTI quantitative maps will enable the visualization of artificially generated AF tears of magnitudes that will be inconspicuous to conventional MRI IVD injury detection protocols.

2. DTI AF tear measurements (TraceADC, diffusivity along principle eigenvector directions (eigenvalues 1-3), and Fractional Anisotropy) will be significantly different from that of the NP.

3. Dynamic compression will improve DTI's detection of artificially induced AF tears.

1.7 *Limitations:*

This study is limited in several ways. First, the DTI sequence used could only be implemented on radio-frequency (RF) coils with parallel imaging capabilities. Of the RF coils available, one designed specifically for cerebral imaging was best suited for the DTI sequence. As this research called for the comparison of conventional and DTI MRI in AF tear detection, this coil was used to generate all the images in the study. Because this coil was not optimized for spinal imaging, visualization of the IVD for all MRI sequence was of a reduced quality. Second, inherent low signal to noise ratio (SNR) in this anatomical region (Holder, 2000) compromised the validity of the quantitative numbers acquired from regions in the AF. DTI maps are strongly dependent on a minimum signal to noise level (Bammer et al., 2002, Drew et al., 2004), which may not be possible with clinically available MRI hardware. Lastly, the use of swine as an animal model for the human IVD has been well documented (Bass et al., 1997), however, there will be no immediate crossover to human populations from this *in vitro* study.

1.8 *Ethical considerations:*

This study utilized porcine lumbar spine segments acquired from the University of Alberta Swine Research and Technology Centre. The NMR Research Committee approved the use of its facilities for animal testing, and the Faculty Animal Welfare and Policy Committee approved this study. Ethics protocols are located in Appendix A.

1.9 *Significance of the study:*

DTI and dynamic imaging are new protocols that have demonstrated numerous successes in visualizing pathologies, as well as contributing new knowledge of tissue microstructure and function. This project seeks to develop an experimental protocol that will effectively assess not only DTI's ability to identify tears in the AF, but also what impact dynamic loading has on DTI tear sensitivity. Because clinical imaging has not reached sensitivities where AF failures are identified consistently (Gilbert et al., 2004a, Gray et al., 2003, Kakitsubata et al., 2003, Munter et al., 2002), the results from this study will comment on the relevance of DTI sequences augmenting existing MRI IVD protocols. Given that current MRI LBP indicators of disc height narrowing, annular tears, and NP signal intensity have low sensitivities (Videman et al., 2003), the rotationally invariant quantitative measures of DTI sequences may provide more meaningful information regarding the relationship between IVD function and LBP. Finally, the last experiment in this study may serve as a relevant experimental protocol to assess changes in IVD function following injury and/or treatments of animal models.

Chapter 1 references

Acaroglu, E.R., Iatridis, J.C., Setton, L.A., Foster, R.J., Mow, V.C., Weidenbaum, M., 1995. Degeneration and aging affect the tensile behavior of human lumbar anulus fibrosus. Spine. 2024, 2690-2701.

Andersson, G., 1997. The epidemiology of spinal disorders in: Frymoyer, J., (Ed), The Adult Spine: Principles and Practices, 2nd ed. Lippincott-Raven, Philadelphia, pp. 93-141.

Antoniou, J., Demers, C.N., Beaudoin, G., Goswami, T., Mwale, F., Aebi, M., Alini, M., 2004. Apparent diffusion coefficient of intervertebral discs related to matrix composition and integrity. Magn. Reson. Imaging. 227, 963-972.

Asano, S., Kaneda, K., Umehara, S., Tadano, S., 1992. The mechanical properties of the human L4-5 functional spinal unit during cyclic loading. The structural effects of the posterior elements. Spine. 1711, 1343-1352.

Bammer, R., Auer, M., Keeling, S.L., Augustin, M., Stables, L.A., Prokesch, R.W., Stollberger, R., Moseley, M.E., Fazekas, F., 2002. Diffusion tensor imaging using single-shot SENSE-EPI. Magn. Reson. Med. 481, 128-136.

Bammer, R., Fazekas, F., 2003. Diffusion imaging of the human spinal cord and the vertebral column. Top. Magn. Reson. Imaging. 146, 461-476.

Bass, E.C., Duncan, N.A., Hariharan, J.S., Dusick, J., Bueff, H.U., Lotz, J.C., 1997. Frozen storage affects the compressive creep behavior of the porcine intervertebral disc. Spine. 2224, 2867-2876.

Basser, P.J., 1995. Inferring microstructural features and the physiological state of tissues from diffusion-weighted images. NMR Biomed. 87-8, 333-344.

Brinkman, P., Frobin, W., Leivseth, G., 2002. Mechanical Aspects of the Lumbar Spine in:

Chiu, E.J., Newitt, D.C., Segal, M.R., Hu, S.S., Lotz, J.C., Majumdar, S., 2001. Magnetic resonance imaging measurement of relaxation and water diffusion in the human lumbar intervertebral disc under compression in vitro. Spine. 2619, E437-44.

Chu, W.C., Tam, Y.H., Lam, W.W., Ng, A.W., Sit, F., Yeung, C.K., 2007. Dynamic MR assessment of the anorectal angle and puborectalis muscle in pediatric patients with anismus: Technique and feasibility. J. Magn. Reson. Imaging.

Cihangiroglu, M., Yildirim, H., Bozgeyik, Z.B., Senol, U.S., Ozdemir, H., Topsakal, C., Yilmaz, S., 2004. Observer variability based on the strength of MR scanners in the assessment of lumbar degenerative disc disease. Eur. J. Radiol. 513, 202-208.

Collins, M.J., Ozeki, T., Zhuo, J., Gu, J., Gullapalli, R., Pierson, R.N., Griffith, B.P., Fedak, P.W., Poston, R.S., 2007. Use of diffusion tensor imaging to predict myocardial viability after warm global ischemia: possible avenue for use of non-beating donor hearts. J. Heart Lung Transplant. 264, 376-383.

Dong, Q., Welsh, R.C., Chenevert, T.L., Carlos, R.C., Maly-Sundgren, P., Gomez-Hassan, D.M., Mukherji, S.K., 2004. Clinical applications of diffusion tensor imaging. J. Magn. Reson. Imaging. 191, 6-18.

Drew, S.C., Silva, P., Crozier, S., Pearcy, M.J., 2004. A diffusion and T2 relaxation MRI study of the ovine lumbar intervertebral disc under compression in vitro. Phys. Med. Biol. 4916, 3585-3592.

Fujita, Y., Duncan, N.A., Lotz, J.C., 1997. Radial tensile properties of the lumbar annulus fibrosus are site and degeneration dependent. J. Orthop. Res. 156, 814-819.

Gilbert, F.J., Grant, A.M., Gillan, M.G., Vale, L., Scott, N.W., Campbell, M.K., Wardlaw, D., Knight, D., McIntosh, E., Porter, R.W., 2004a. Does early imaging influence management and improve outcome in patients with low back pain? A pragmatic randomised controlled trial. Health Technol. Assess. 817, iii, 1-131.

Gilbert, F.J., Grant, A.M., Gillan, M.G., Vale, L.D., Campbell, M.K., Scott, N.W., Knight, D.J., Wardlaw, D., Scottish Back Trial Group, 2004b. Low back pain: influence of early MR imaging or CT on treatment and outcome--multicenter randomized trial. Radiology. 2312, 343-351.

Gray, D.T., Hollingworth, W., Blackmore, C.C., Alotis, M.A., Martin, B.I., Sullivan, S.D., Deyo, R.A., Jarvik, J.G., 2003. Conventional radiography, rapid MR imaging, and conventional MR imaging for low back pain: activity-based costs and reimbursement. Radiology. 2273, 669-680.

Gu, W.Y., Mao, X.G., Foster, R.J., Weidenbaum, M., Mow, V.C., Rawlins, B.A., 1999. The anisotropic hydraulic permeability of human lumbar anulus fibrosus. Influence of age, degeneration, direction, and water content. Spine. 2423, 2449-2455.

Haughton, V., 2004. Medical imaging of intervertebral disc degeneration: current status of imaging. Spine. 2923, 2751-2756.

Haughton, V.M., Lim, T.H., An, H., 1999. Intervertebral disk appearance correlated with stiffness of lumbar spinal motion segments. AJNR Am. J. Neuroradiol. 206, 1161-1165.

Hensley, S., 1997. MRI renaissance. Mod. Healthc. 274, 56.

Hickey, D.S., Hukins, D.W., 1980. Relation between the structure of the annulus fibrosus and the function and failure of the intervertebral disc. Spine. 52, 106-116.

Hiwatashi, A., Danielson, B., Moritani, T., Bakos, R.S., Rodenhause, T.G., Pilcher, W.H., Westesson, P.L., 2004. Axial loading during MR imaging can influence treatment decision for symptomatic spinal stenosis. AJNR Am. J. Neuroradiol. 252, 170-174.

Holder, C.A., 2000. MR diffusion imaging of the cervical spine. Magn. Reson. Imaging Clin. N. Am. 83, 675-686.

Hsu, E.W., Setton, L.A., 1999. Diffusion tensor microscopy of the intervertebral disc anulus fibrosus. Magn. Reson. Med. 415, 992-999.

Iatridis, J.C., ap Gwynn, I., 2004. Mechanisms for mechanical damage in the intervertebral disc annulus fibrosus. J. Biomech. 378, 1165-1175.

Jackson, K.C.,2nd, 2004. Pharmacotherapy in lower back pain. Drugs Today (Barc). 409, 765-772.

Kakitsubata, Y., Theodorou, D.J., Theodorou, S.J., Trudell, D., Clopton, P.L., Donich, A.S., Lektrakul, N., Resnick, D., 2003. Magnetic resonance discography in cadavers: tears of the annulus fibrosus. Clin. Orthop. Relat. Res. (407)407, 228-240.

Kealey, S.M., Aho, T., Delong, D., Barboriak, D.P., Provenzale, J.M., Eastwood, J.D., 2005. Assessment of apparent diffusion coefficient in normal and degenerated intervertebral lumbar disks: initial experience. Radiology. 2352, 569-574.

Kerttula, L., Kurunlahti, M., Jauhiainen, J., Koivula, A., Oikarinen, J., Tervonen, O., 2001. Apparent diffusion coefficients and T2 relaxation time measurements to evaluate disc degeneration. A quantitative MR study of young patients with previous vertebral fracture. Acta Radiol. 426, 585-591.

Kingma, I., van Dieen, J.H., Nicolay, K., Maat, J.J., Weinans, H., 2000. Monitoring water content in deforming intervertebral disc tissue by finite element analysis of MRI data. Magn. Reson. Med. 444, 650-654.

Kraemer, J., Kolditz, D., Gowin, R., 1985. Water and electrolyte content of human intervertebral discs under variable load. Spine. 101, 69-71.

Lander, P.H., 2005. Lumbar discography: current concepts and controversies. Semin. Ultrasound CT MR. 262, 81-88.

Le Bihan, D., 1991. Molecular diffusion nuclear magnetic resonance imaging. Magn. Reson. Q. 71, 1-30.

Luo, X., Pietrobon, R., Sun, S.X., Liu, G.G., Hey, L., 2004. Estimates and patterns of direct health care expenditures among individuals with back pain in the United States. Spine. 291, 79-86.

Malko, J.A., Hutton, W.C., Fajman, W.A., 1999. An in vivo magnetic resonance imaging study of changes in the volume (and fluid content) of the lumbar intervertebral discs during a simulated diurnal load cycle. Spine. 2410, 1015-1022.

Masuda, K., Aota, Y., Muehleman, C., Imai, Y., Okuma, M., Thonar, E.J., Andersson, G.B., An, H.S., 2005. A novel rabbit model of mild, reproducible disc degeneration by an anulus needle puncture: Correlation between the degree of disc injury and radiological and histological appearances of disc degeneration. Spine. 301, 5-14.

Morgan, S., Saifuddin, A., 1999. MRI of the lumbar intervertebral disc. Clin. Radiol. 5411, 703-723.

Munter, F.M., Wasserman, B.A., Wu, H.M., Yousem, D.M., 2002. Serial MR Imaging of Annular Tears in Lumbar Intervertebral Disks. AJNR Am. J. Neuroradiol. 237, 1105-1109.

Osti, O.L., Fraser, R.D., 1992. MRI and discography of annular tears and intervertebral disc degeneration. A prospective clinical comparison. J. Bone Joint Surg. Br. 743, 431-435.

Rajasekaran, S., Babu, J.N., Arun, R., Armstrong, B.R., Shetty, A.P., Murugan, S., 2004. ISSLS prize winner: A study of diffusion in human lumbar discs: a serial magnetic resonance imaging study documenting the influence of the endplate on diffusion in normal and degenerate discs. Spine. 2923, 2654-2667.

Rowley, H.A., Grant, P.E., Roberts, T.P., 1999. Diffusion MR imaging. Theory and applications. Neuroimaging Clin. N. Am. 92, 343-361.

Saifuddin, A., McSweeney, E., Lehovsky, J., 2003. Development of lumbar high intensity zone on axial loaded magnetic resonance imaging. Spine. 2821, E449-51; discussion E451-2.

Sasaki, K., 1995. Magnetic resonance imaging findings of the lumbar root pathway in patients over 50 years old. Eur. Spine J. 42, 71-76.

Vedi, V., Williams, A., Tennant, S.J., Spouse, E., Hunt, D.M., Gedroyc, W.M.W., 1999. Meniscal movement - An in-vivo study using dynamic MRI. Journal of Bone and Joint Surgery-British Volume. 81B1, 37-41.

Videman, T., Battie, M.C., Gibbons, L.E., Maravilla, K., Manninen, H., Kaprio, J., 2003. Associations between back pain history and lumbar MRI findings. Spine. 286, 582-588.

Videman, T., Nurminen, M., 2004. The occurrence of anular tears and their relation to lifetime back pain history: a cadaveric study using barium sulfate discography. Spine. 2923, 2668-2676.

Wheeler-Kingshott, C.A., Parker, G.J., Symms, M.R., Hickman, S.J., Tofts, P.S., Miller, D.H., Barker, G.J., 2002. ADC mapping of the human optic nerve: increased resolution, coverage, and reliability with CSF-suppressed ZOOM-EPI. Magn. Reson. Med. 471, 24-31.

Wilke, H.J., Neef, P., Caimi, M., Hoogland, T., Claes, L.E., 1999. New in vivo measurements of pressures in the intervertebral disc in daily life. Spine. 248, 755-762.

Yu, C.Y., Tsai, K.H., Hu, W.P., Lin, R.M., Song, H.W., Chang, G.L., 2003. Geometric and morphological changes of the intervertebral disc under fatigue testing. Clin. Biomech. (Bristol, Avon). 186, S3-9.

Chapter 2: Literature Review

Overview

This literature review will provide the detail needed to appreciate why diffusion MRI is of such interest in the study of LBP, specifically the characterization of fluid diffusion within injuries to the IVD. Both the structures of the IVD and their function will be discussed in detail, as well as the impact that annular tears and other injuries may have on IVD function and how these injuries may change fluid diffusion in the IVD. The basic challenges of clinical MRI toward the detection of IVD injuries will also be highlighted as a backdrop to the potential use of diffusion MRI in the study of LBP. Finally, contemporary MRI techniques (parallel and echo planar imaging (EPI)) will be introduced, and then described in terms of how they have made diffusion MRI a potentially viable tool toward generating new knowledge regarding IVD function and its relation to LBP.

2.1 *Anatomy of the Intervertebral disc:*

Though the morphology of the IVD is not constant and changes with age, injury, and degeneration, the general form is two heterogeneous and distinct structures (Figure 1). Both the NP and AF are comprised of cells that are embedded in extracelluar matrixes of primarily proteoglycans, collagen and water, and both these structures interact with adjacent vertebrae through their attachment to the cartilaginous endplates. The basic form of the lumbar IVD is consistent with IVDs in the other regions of the spine. The larger compressive loads experienced by these IVDs does tend to result in larger dimensions than their superior counterparts (Coventry, Ghormley, & Kernohan, 1945). Finally, the healthy IVD only has limited vasculature and/or innervation at its periphery (Adams and Roughley, 2006).

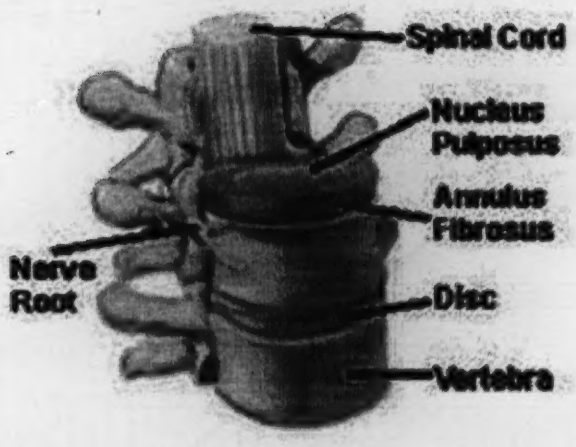

Figure 1. The major structures of the spine surrounding the IVD, including an axial view that describes the arrangement of the NP and AF (image from www.wolfhouse.dk/articles/images/img_fce_figure1.jpg)

Nucleus pulposus

The NP is spherical, gelatinous material, which radially transitions into the inner AF, and is bound by the cartilaginous endplates of adjacent vertebral bodies (Figures 2 and 3).

Figure 2. Anatomical observation of NP denoted by arrow in the sagittal plane (Yu et al., 2003).

Figure 3. Anatomical observation of NP denoted by arrow in the transverse plane (Yu et al., 2003).

The gel-like matrix of the NP is a result of a vast type II collagen network that loosely entraps proteoglycan aggregates and water (Adams and Roughley, 2006, Roberts, 2002) (Figure 4). NP cells are generally oval in shape and synthesize collagen II under loading conditions (Adams and Roughley, 2006). The NP has one of the lowest cell densities of any structure in the body, and there is little to no vasculature or innervation in this region. (Adams and Roughley, 2006).

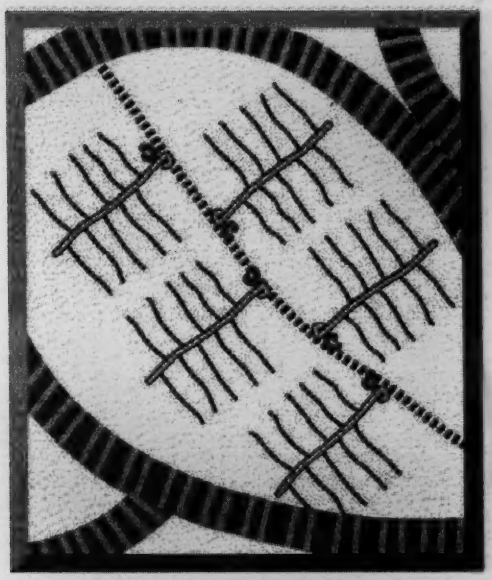

Figure 4. A section of NP depicted as containing proteoglycan aggregates entrapped in a collagen fiber network. Proteoglycan aggregates are (dashed line) replaced with aggrecan molecules possessing a central core protein (open line) and glycosaminoglycan side chains (solid lines). The hydration properties of the glycosaminoglycan chains of aggrecan cause the tissue to swell until an equilibrium is reached, in which the swelling potential is balanced by tensile forces in the collagen network (Adams and Roughley, 2006).

While there is a clear transition from cartilage endplate to the NP, the transition of the NP to the inner AF has no definite boundary and is poorly defined (Cassidy, Hiltner, & Baer, 1989). The layers of the AF begin to gradually replace nuclear material as proximity to the centre of the IVD increases radially (Cassidy, Hiltner, & Baer, 1989, Marchand and Ahmed, 1990), however the position of this relative boundary has been shown to change due to degeneration and ageing (Marchand and Ahmed, 1990).

Annulus fibrosus

The AF consists of a series of concentric fibre layers, which contain the NP. It has three regions (Figure 5) that transition directly from the NP to the paravertebral soft tissue that line the exterior of the IVD (Fujita, Duncan, & Lotz, 1997). Generally, the individual layers of the AF, or lamellae, are distinct and separate (Cassidy, Hiltner, & Baer, 1989),

and are anchored to the cartilaginous endplates of adjacent vertebral bodies (Cassidy, Hiltner, & Baer, 1989) (Figure 5). The nerve fibres and vasculature that do develop in the IVD are present in the outer few fibres of the AF, at the IVD's periphery (Roberts, 2002).

Figure 5. Mid-sagittal section of cadaveric IVD showing NP and distinct radial layers of the AF. The transition zone of the AF is the portion interfacing with the NP (A), and the inner AF constitutes the middle portion of the entire AF (B), while the outer AF is the portions furthest away from the NP (C) (Adams and Roughley, 2006).

An estimated 15- 25 distinct lamellar fibre layers comprise the radial thickness of the AF, and the thickness of these layers has been shown to range from 0.14 to 0.66 mm (Marchand and Ahmed, 1990). Considering only the anterior aspect of the IVD, individual lamellae are found to be most distinct in the outer annulus, and less so towards the centre of the IVD (Marchand and Ahmed, 1990). Conversely, layer thickness increases as proximity to the NP increases (Marchand and Ahmed, 1990). Despite the increased layer thickness in the inner and middle annulus, most of this increased width is occupied by gel-like ground substance, and 40-80% these inner layers are tortuous and incomplete (Marchand and Ahmed, 1990). As noted, the inner AF also encompasses a portion of the transition layer between the AF and NP, making definitive structural observations of this region of the AF problematic (Cassidy, Hiltner, & Baer, 1989). Variations in lamellae arrangement and size have been noted depending on location in IVD, and the posterior and lateral aspects of the IVD tend to have thinner laminar layers, and do not vary significantly along a radial path as in the anterior AF (Cassidy, Hiltner, & Baer, 1989). Also, though upon general observation the layers of the IVD seem continuous, nearly half are not continuous over a 20° circumferential sector of AF

(Marchand and Ahmed, 1990). In fact, lamellar layers are often incomplete, ending abruptly between two adjacent layers, or splitting an existing layer causing it to fork (Marchand and Ahmed, 1990). Lamellae have also been shown to not always extend from endplate to endplate (Marchand and Ahmed, 1990).

Individual lamellae fibre layers consist of tightly packed collagen type 1 fibre bundles suspended in a gel-like ground substance (Marchand and Ahmed, 1990) (Figure 6). The orientation of these fibre bundles also alternates between adjacent layers creating a criss-cross pattern with an average fibre bundle angle of ± 30° to the transverse plane (Adams and Roughley, 2006, Marchand and Ahmed, 1990) (Figure 7). These fibre angles can vary quite significantly over an area given laminate irregularities (Marchand and Ahmed, 1990), radial position within the AF (Cassidy, Hiltner, & Baer, 1989), or proximity to supporting structures like ligaments or pedicles in the outer AF (Marchand and Ahmed, 1990). Between the laminar layers, aggregated proteoglycans and elastin are found in abundance (Fujita, Duncan, & Lotz, 1997, Roberts, 2002).

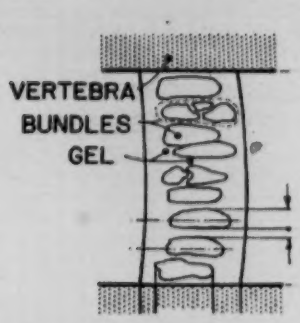

Figure 6. An in plane representation of the collagen fibre bundles comprising a length of lamella (Marchand and Ahmed, 1990).

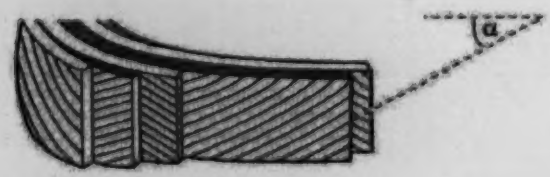

Figure 7. A circumferential section of AF with alternating fibre angles of α = approximately 30°(Adams and Roughley, 2006).

AF cells are found mostly parallel to the collagen fibres in the lamellae, resulting in thinner, more elongated cell bodies than NP cells (Roberts, 2002). Under tensile deformation these cells causes synthesis of collagen type 1 (Adams and Roughley, 2006). The cell density in the AF is also quite low, making the mature IVD one of least cellular tissues in the body (Roughley, 2004).

The morphology of the AF is not constant, even without trauma changes are observed (Roberts, 2002). Movement and loading contributes to the adaptive remodeling of collagen fibre directions in the various regions of the disc (Adams and Roughley, 2006). Age has also been found to change the structure of the IVD, significantly reducing the number of distinct layers within the AF, yet further increasing the thickness of individual layers (Marchand and Ahmed, 1990).

Cartilage endplate

Fixated to the AF, the cartilage endplates complete the encapsulation of the high-pressured NP. Consisting of hyaline cartilage (Coventry, Ghormley, & Kernohan, 1945), this structure is weekly bonded to the vertebral bodies (Adams and Roughley, 2006), allowing the functional pairing of the IVD and vertebra for the dynamic movement of the spine. Porous in nature, nutrients and waste pass through the endplate to and from the IVD and vasculature in the porous cortical bone of vertebrae (Adams and Roughley, 2006, Gu et al., 1999, Roberts, Menage, & Eisenstein, 1993).

2.2 *Function of the intervertebral disc:*

In addition to facilitating movement between adjacent vertebral bodies, the structures of the IVD makes it well adapted to dampening compressive forces traveling through the spine. The longitudinal components of compressive loads are almost entirely transmitted through the IVD (Brinkmann, Frobin, & Leivseth, 2002), and in order to compensate for average daily compressive forces of 0.1 - 2.30MPa or 10 N/cm^2 – 230 N/cm^2 (Wilke et al., 1999), the IVD relies on a system of fluid exudation and uptake, which is coupled with the viscoelastic properties of the AF and NP (Broberg, 1993, Fujita, Iatridis et al., 1997, Ohshima et al., 1989, Wilke et al., 1999, Williams, Natarajan, & Andersson, 2006) (Figure 8).

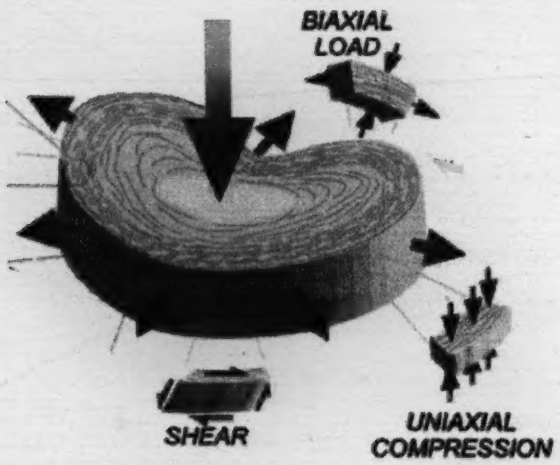

Figure 8. The stress, strains and hydrostatic pressure distribution of longitudinal compression forces (Setton and Chen, 2006).

Mechanical Systems:

To distribute the pressure uniformly over the surface of the endplates and to keep the joint mobile, the IVD tissue must be able to shift a certain amount within the disc space. In the healthy IVD, the NP is prevented from squeezing out of the disc space by the tensile forces of the outer AF. Moderate degeneration doesn't dramatically alter the uniform pressure distribution when endplates of adjacent discs are not parallel, but serious degeneration will cause increased pressure where the endplates are closest (Adams and Roughley, 2006, Brinkmann, Frobin, & Leivseth, 2002).

1) Movement

Movement of the vertebra-IVD-vertebra motion unit over a limited range is possible due to the deformation properties of the IVD, the presence of ligaments and the shape of the articulating bone structure of the vertebral bodies (Brinkmann, Frobin, & Leivseth, 2002) (Figure 9).

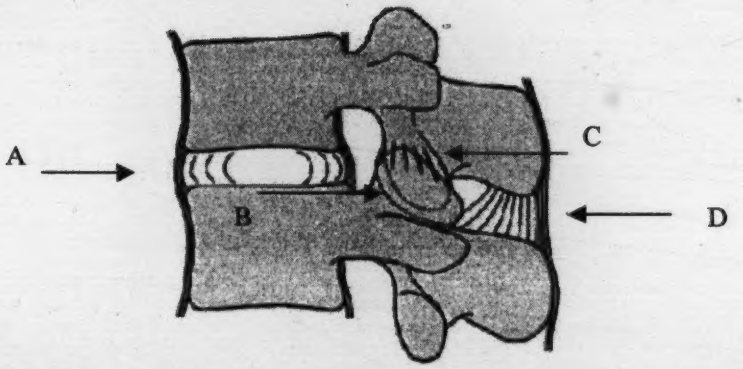

Figure 9. Structures in motion unit that deform to facilitate movement. A) Anterior longitudinal ligament and AF, B) apophyseal joint, C) facet capsulary ligament, D) posterior longitudinal ligament (Adams and Dolan, 2005).

The radial fibres of the AF allow for torsional movement, however the orientation of the apophyseal joints creates bony compaction (position B on Figure 9) and IVD ligaments are substantially stretched after 1-3° of axial rotation (position A, C and D on Figure 9) (Adams, 2004). In flexion-extension the NP migrates away from the direction of motion (Fazey et al., 2006), reducing the pressure resisting the motion of the vertebral bodies (Brinkmann, Frobin, & Leivseth, 2002, Fazey et al., 2006). Like in torsion, the presence of the IVD ligaments in conjunction with the apophyseal joints and neural arches limits the range of flexion-extension motion to about 12° (Brinkmann, Frobin, & Leivseth, 2002).

2) Viscoelastic response to load

The NP is characterized as being a non-compressible fluid under significant pressure (Adams, 2004, Brinkmann, Frobin, & Leivseth, 2002). In the healthy disc, the pressure distribution throughout the NP is uniform, and the AF is loaded in tension to maintain radial NP containment (Adams, 2004, Brinkmann, Frobin, & Leivseth, 2002). As discussed, the superior and inferior endplate complete the NP containment, but because the AF dictates the IVDs viscoelastic response to loads (Markolf and Morris, 1974), it will be the focus of this section.

The perpetual compressive forces acting on the static lumbar spine through body weight and internal muscle force results in the bulging of the AF into the paravertebral space, up to 1mm (Brinckmann et al., 1983, Brinckmann and Horst, 1985) (see position A, Figure 9). Any additional compressive force experienced by the IVD must be accommodated through generating additional 'hoop stress' in the AF and increased bulging (Adams, 2004) (Figure 10). Increased AF bulging also results in a gradual reduction in IVD height, but as load is reduced the height of the AF returns to equilibrium, tightening the AF fibres (Brinkmann, Frobin, & Leivseth, 2002). The attachment of the lamellae to the adjacent endplates in tension maintains the high intradiscal pressure of the NP even at low loads (Brinkmann, Frobin, & Leivseth, 2002).

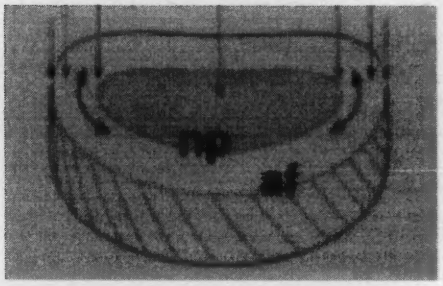

Figure 10. Circumferential tension or 'hoop stress' maintains containment of the NP (Adams and Dolan, 2005).

Though uniform pressure is experienced over the vertebral endplates, the radial stress in the AF is concentrated in its outer layers (Brinckmann et al., 1983, Brinckmann and Horst, 1985). In general, mechanical testing has shown a non-linear stress-strain curve for the IVD under load (Markolf and Morris, 1974). At small strains in the radial direction the elastic modulus is approximately 0.19MPa, however at higher strains, the radial behavior of the AF becomes increasingly non-linear, with the middle annulus being the stiffest of the three regions (Fujita, Duncan, & Lotz, 1997). The postero-lateral AF has also been determined to have a higher radial stiffness than the anterior region of the IVD (Fujita, Duncan, & Lotz, 1997).

The proportion of Type I collagen in the AF increases with distance from the NP and inner AF (Roughley, 2004). The modulus of elasticity for a single annulus layer along the axis of the spine has been shown to range from 60 – 140MPa (Skaggs et al., 1994), with the peripheral AF sections exhibiting a higher stiffness (Ebara et al., 1996, Skaggs et al., 1994). Significant differences in stiffness have also been found between the anterior and postero-lateral regions of the IVD with collagen fibres having a higher longitudinal tensile strength in the anterior regions (Ebara et al., 1996, Skaggs et al., 1994).

3) Mathematical modeling

Because the IVD exhibits non-linear elastic characteristics, the rate of load application and the magnitude of compression also influence its response to loads. Consistent with what is seen in a normal dashpot element, the viscous-response (restricted diffusion) is delayed in relation to rapid impact loads (Ohshima et al., 1989). During dynamic physiological loading situations, researchers have described the IVD's short-term deformation as being dominated by the AF (Broberg, 1993, Martinez, Oloyede, & Broom, 1997). Numerous models have been created to predict the IVDs response to physiological loading (Baer et al., 2003, Ferguson, Ito, & Nolte, 2004, Goel et al., 1995, Kingma et al., 2000, Malko, Hutton, & Fajman, 1999), yet the results using a single deformable solid, or fluidic-solid were inaccurate over varied loading schemes (Wilke et al., 1999). To understand and predict the general response of the IVD to load, one must acknowledge that the hydration of the IVD's structures has a direct impact on its viscoelastic properties (Natarajan, Williams, & Andersson, 2003/5, Williams, Natarajan, & Andersson, 2006), and thus, its ability to respond to complex movements and loading of the spine (Gu et al., 1999, Johannessen et al., 2004, Ohshima et al., 1989).

Hydrostatic System:

In general, the hydration of the IVD's structures has a direct impact on its viscoelastic properties, and thus, it's ability to respond to complex movements and loading of the spine (Adams, Dolan, & Hutton, 1987, Fujita, Duncan, & Lotz, 1997, Lee and Teo, 2004). Fluid is forced out of the disc when compressed, and imbibed when the load is removed (Kraemer, Kolditz, & Gowin, 1985). Both the NP and AF contain significant

amount of fluid, some of which is mobile, moving relative to the deformable solid components of the IVD (Martinez, Oloyede, & Broom, 1997). Very little fluid flow occurs during short term or fluctuating loading of the IVD (Lee and Teo, 2004, Malko, Hutton, & Fajman, 1999). Therefore, the initial phase of loading is dominated by the viscoelastic deformation of the AF (Broberg, 1993), but given sufficient axial compression and time, fluid outflow is induced via the hydrostatic stress generated mainly within the NP. In response to the hydrostatic force, the AF acts primarily in tension; deforming to contain this pressure front (Cassidy, Hiltner, & Baer, 1989, Hukins, 1992), but also restricting fluid flow in conjunction with the endplates as both structures are porous materials with direction dependent permeability properties (Bass et al., 1997, Gu et al., 1999, Ohshima et al., 1989).

The proteoglycans trapped within the collagen type 2 matrix in the amorphous NP have tremendous water binding properties, approximately 80% water in the healthy adult IVD (Bass et al., 1997, Kraemer, Kolditz, & Gowin, 1985). This ability to bind water is at its height under low pressure, but under increasing pressures the level of unbound water increases (Brinkmann, Frobin, & Leivseth, 2002) allowing diffusion to redistribute the fluid into the AF and through the endplates (Ayotte, Ito, & Tepic, 2001, Brinkmann, Frobin, & Leivseth, 2002, Broberg, 1993, Ferguson, Ito, & Nolte, 2004, Ohshima et al., 1989, Rajasekaran et al., 2004). As fluid is exuded out, the volume of the IVD is reduced, resulting in an overall reduction in IVD height and increase in AF bulge into the epidural space (Botsford, Esses, & Ogilvie-Harris, 1994). The AF also has interlaminar proteoglycans (Fujita, Duncan, & Lotz, 1997), which could suffer from reduced water affinity due to the increased pressure under load.

For the most part, it can be assumed that the permeability properties of the cartilage endplate are bi-directional (longitudinal), or fluid in and fluid out (Ayotte, Ito, & Tepic, 2001). Fluid diffusion through the AF on the other hand is multidirectional (radial, longitudinal, circumferential) (Figure 11) (Gu et al., 1999), and the inner, middle and outer regions of the AF exhibit different diffusion properties (Kusaka et al., 2001, Ohshima et al., 1989). *Ex vivo* data has shown that radial diffusion dominates at regions

in the AF with higher water contents like the inner annulus, but that axial and circumferential diffusion begin to dominate towards the outer annulus where the water content is not as high (Gu et al., 1999, Ohshima et al., 1989).

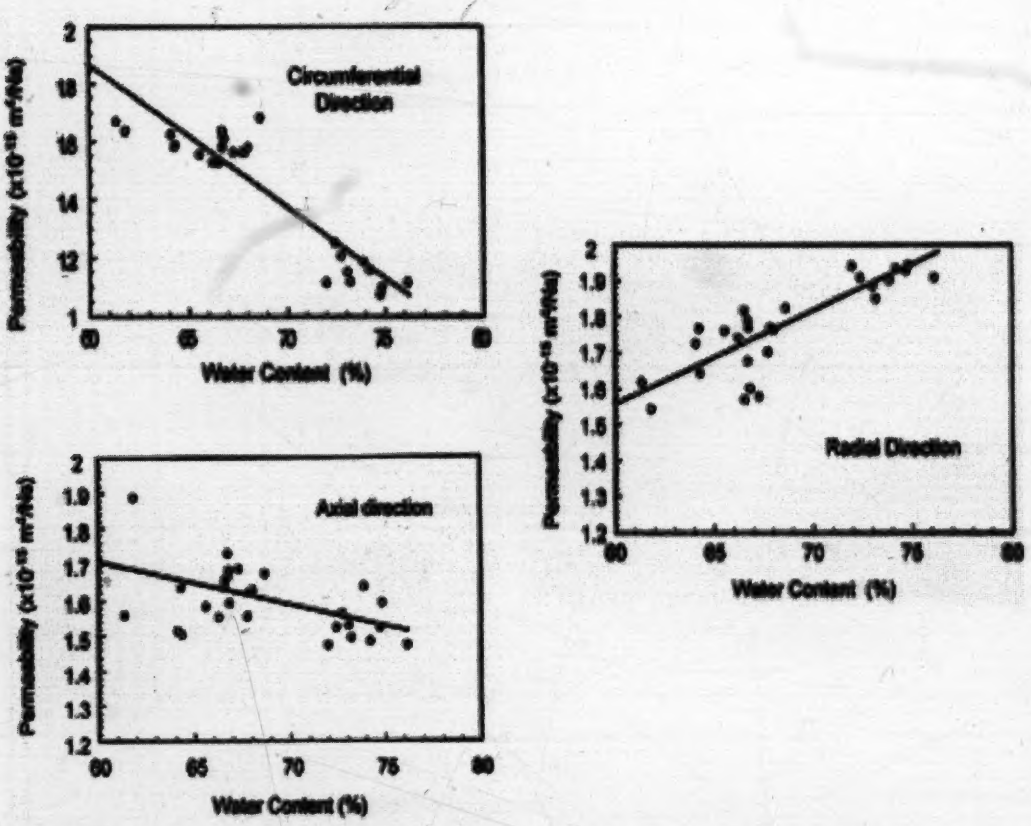

Figure 11. The correlation between water content and directional permeability (Gu et al., 1999).

Though there is general acceptance that the, NP, AF and endplates have directional diffusion properties, uncertainty remains regarding the actual direction of diffusion within these regions during load conditions (Ferguson, Ito, & Nolte, 2004).

1) Mathematical modeling

Because of the difficulty of measuring diffusion directions *in vivo* (van der Veen et al., 2005), mathematical models have been developed to predict the osmotic response to IVD loading (Ferguson, Ito, & Nolte, 2004, Lee and Teo, 2004). To generate results, early models had to apply assumptions that greatly simplified the mechanical behaviour of the IVD, using physiological load and deformation data collected from other unrelated studies as constants (Broberg, 1993, Hukins, 1992). The basic assumptions of these predictive mathematical models governed the results as there were large variations in the conclusions reached regarding the role of the osmotic system in loading, and the direction of fluid movement once initiated via loading (Lee and Teo, 2004). Now, with improved understanding of the fluid and solid phase displacements of the IVD (Kusaka et al., 2001, Lee and Teo, 2004), the new challenge is to generate IVD tissue properties in circumstances that closely approximate *in vivo* conditions (Ferguson, Ito, & Nolte, 2004, Gu et al., 1999, van der Veen et al., 2005). This will hopefully lead to models that can closer approximate when fluid movement is induced, in response to what pressures, and in what directions (Lee and Teo, 2004). Diffusion MRI through fibre tracking may also provide opportunities for tracing the path of bulk water movement in the IVD.

2.3 *Injury to the intervertebral disc:*

There are numerous forms of acute and chronic IVD injury that have been shown to cause pain in the immediate tissue area (Saifuddin, Mitchell, & Taylor, 1999), as well as injuries that have been shown to be completely asymptomatic (Buirski and Silberstein, 1993). Since IVD degeneration has been shown to be readily detectable using MRI and CT (Van Goethem et al., 2005), this pathology has traditionally dominated the explanation for pain in the lower back. Now, over the last few years radial, transverse and circumferential tears in the AF are described as significant contributors and potentially even initiators of some forms of LBP (Crock, 1986, Kakitsubata et al., 2003, Morgan and Saifuddin, 1999).

Ageing and degeneration

Even without trauma induced changes, the morphology of the IVD is not constant (Roberts, 2002), age has been found to change the structure of the IVD (Adams and Dolan, 2005). The IVD becomes increasingly dehydrated as age increases, having dramatic effect on the IVD structure. Kraemer *et al.* reported that the relative water content over an 80-year period of the NP goes from 90 % to 74 %, with the NP becoming increasingly fibrous, and the overall IVD height decreasing (Yu et al., 2003). The AF's water content falls from 80 % to 67% in the 30th year, yet rises again up to 72 % in the 80th year (Kraemer, Kolditz, & Gowin, 1985). This coincides with a significant reduction in the number of distinct layers within the AF through the thickening of the transition zone between the NP and AF, and the gradual loss of defined fibre structures in the inner AF (Marchand and Ahmed, 1990, Roberts, 2002). Yet overall, the naturally occurring change of state of the IVDs is not related to pain (Adams, 2004, Boden et al., 1990).

Degeneration of the IVD, while characterized by some of the same structural changes as ageing, also exhibits additional structural failures that have been found to destabilize the whole joint (Adams, 2004, Adams and Dolan, 2005, Brinkmann, Frobin, & Leivseth, 2002). Degeneration reduces the uniform pressure distribution maintained by healthy IVDs (Adams, McNally, & Dolan, 1996), and disruptions in the AF, NP or endplate not seen in older IVDs result in stress concentrations that reduces the overall pressure generated in the IVD. Because the spinal motion unit is dependent on the IVD to distribute a uniform pressure, stress-shielding or the increased loading of adjacent healthy tissue occurs to compensate (Figure 12) resulting in ligamentous or vertebral damage and/or arthritis (An et al., 2004, Pollintine et al., 2004). Damage, especially to the vertebral body, can lead to pain directly, or through irritation of the nearby nervous tissue (Roberts, 2002). The changes in loading may also put the IVD at further risk for additional injury, and because of its avascular nature, there is very little chance of healing once damaged (Adams and Roughley, 2006, Roughley, 2004).

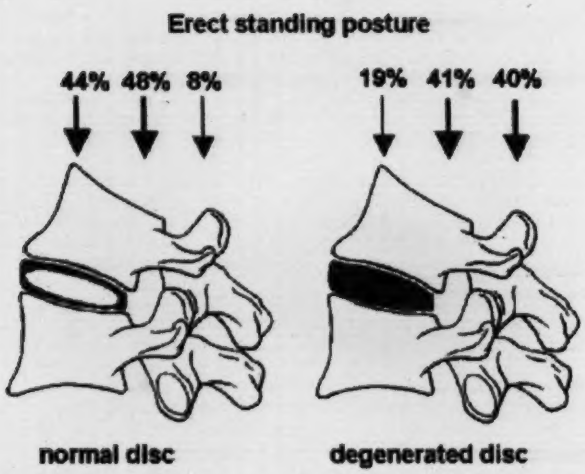

Figure 12. Stress concentration changes due to abnormal discs (Pollintine et al., 2004).

The overall change in load sharing of the lumbar spine due to degeneration is related directly to the local changes of the mechanical and osmotic systems within the IVD (An et al., 2004). Degeneration resulted in an average 30% decrease in yield and ultimate stress compared to healthy radial segments of the AF (Fujita, Duncan, & Lotz, 1997), and degenerative grade has been shown to affect the hydraulic permeability coefficient of AF samples significantly (Gu et al., 1999). The AF and NP are structures with very low cell densities, and very particular circumstances are required to stimulate the regeneration of the respective matrices. Any injury that would impair the local function of these tissues could indeed cause widespread degeneration in the entire IVD over time (Adams, 2004, Setton and Chen, 2006). Considering that small failures in the AF may sufficiently alter the local mechanical system potentially precipitating IVD degeneration, it would be worth considering an article by Fujita *et al.*, where the researchers suggested that interlaminar separation and matrix failure between lamellae may be a very relevant injury mechanism in comparison to larger failure models (Fujita, Duncan, & Lotz, 1997). Furthermore, returning to Marchand *et al.'s* description of the microstructure of the AF provides some evidence into the validity of a interlaminar separation and matrix failure between lamellae model of injury initiation (Marchand and Ahmed, 1990). In the short term, failure and propagation of tears can be initiated through mechanical overloading

(Adams et al., 2000, Yu et al., 2003), but barring the formation of an acute tear a slower process may be the destabilization of the local stress-strain properties in a section of AF.

Tears of the annulus fibrosus

Recall that lamellae are a combination of oval fibre bundles and gelatinous ground substance, often incomplete in both length and height. Marchand *et al.* further describes these fibre bundles as often being infiltrated with ground substances, further dividing the microstructure of these fibres (Marchand and Ahmed, 1990). Considering this morphology, there are many potential failure points between annular layers, and within individual lamellae. A rupture at the proper fault point may result in an injury that propagates across or separates multiple lamellae over a short or long period of time (Iatridis and ap Gwynn, 2004). Though micro-tears could indeed be the precursors to the larger tears in the annulus, at this point the presence of radial, circumferential and transverse tears are very real features detected in patients with LBP and IVD degeneration (Iatridis and ap Gwynn, 2004, Saifuddin, Mitchell, & Taylor, 1999).

Radial tears are defined as disruption of the annular fibers, which extends from the nucleus outward toward the periphery of the annulus (Adams and Roughley, 2006, Fardon DF, Millette PC (Chairpersons), 2001) (Figure 13). Though these tears are characterized as propagating radially from the NP, they are often found with transverse and circumferential components (Fardon DF, Millette PC (Chairpersons), 2001).

Figure 13. Radial tear with axial and sagittal representations. White being the AF, black being the disrupted tissue, and grey being the NP (Adams and Roughley, 2006).

Concentric tear are characterized by the separation and breaking of annular fibers in a plane roughly parallel to the curvature of the disc (Adams and Roughley, 2006, Fardon DF, Millette PC (Chairpersons), 2001) (Figure 14). Because these tears do not

communicate with the NP, interlaminar matrix fills the clefts creating fluid-filled spaces between separated lamellae. (Fardon DF, Millette PC (Chairpersons), 2001).

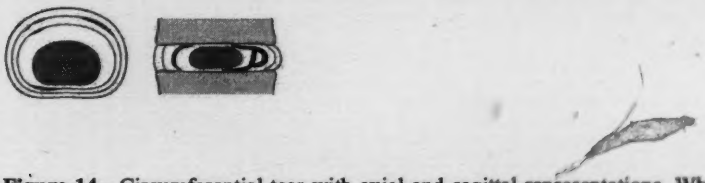

Figure 14. Circumferential tear with axial and sagittal representations. White being the AF, black being the disrupted tissue, and grey being the NP (Adams and Roughley, 2006).

Transverse tears are axial fissure of the annulus, usually limited to ruptures in the outer AF. These tears are usually small and are located at the junction of the AF and endplate (Adams and Roughley, 2006) (Figure 15). More severe radial tears may have transverse components (Fardon DF, Millette PC (Chairpersons), 2001), and nuclear material can move into these clefts as well as interlaminar matrix, extracellular fluid, and cerebrospinal fluid (CSF).

Figure 15. Transverse tear with axial and sagittal representations. White being the AF, black being the disrupted tissue, and grey being the NP (Adams and Roughley, 2006).

The healthy IVD is the largest avascular structure in the body in addition to having one of the lowest cell densities. Minor damage to the IVD takes an extremely long time to repair, and these even higher-level infarctions are not prone to healing (Adams and Dolan, 2005, Adams and Roughley, 2006, Roughley, Alini, & Antoniou, 2002). Also, despite the size of these injuries, inflammation within the IVD does not seem to occur (Roberts, 2002).

Because the morphology of the IVD dictates how the tissue performs physiologically, the presence of these tears affects the loading properties of the IVD (Roberts, 2002).

Injury models

Attempts to reproduce IVD injuries through various models have met with difficulties in controlling injury location and magnitude, as well as minimizing damage from external access to injury site. Two promising injury models have been recently developed. Masuda *et al.*, were able to generate reproducible IVD degeneration, measured in IVD height and MRI grade by using 16GA - 21GA needles to puncture the AF (Masuda et al., 2005). Degeneration results cannot be used to infer acute and asymptomatic disruptions, however, the major success of this study was the limited damage the external initiation of injury caused in comparison to the classical stab model, which was conducted as a comparison.

The second promising injury model was developed by Oliphant *et al.*, and created injuries of different size in the inner AF (Oliphant, Frayne, & Kawchuk, 2005). Compressed gas was introduced into the AF via a 20G catheter, and injury visualization was accomplished using gadolinium dye in MRI. This injury reflected internal disc disruptions, which have been described as disruptions of the internal architecture of the IVD without changes in the external shape (Crock, 1986). These kinds of fissures in the AF are rarely associated with pain until they propagate to the outer third of the annulus (Aprill and Bogduk, 1992). Because this is a promising injury generation technique characterization of the injury created using this protocol was further investigated by the author for use in this research (Appendix B).

2.4 *MRI detection of intervertebral disc tears:*

The distinct advantage of MRI over other imaging modalities for spinal imaging is its ability to generate excellent contrast between soft-tissues. Because of the high incidence of LBP, the lumbar spine is now one of the most frequently examined areas of the body using MRI (Morgan and Saifuddin, 1999).

Though annular failures have been extensively observed using MRI, their presence in both symptomatic and asymptomatic cases make it difficult to determine their relation to

LBP (Kakitsubata et al., 2003, Munter et al., 2002). Further, when successful, MRI detection of annular injury is limited by an ability to preferentially discriminate injuries with partial to full-thickness tears (Aprill and Bogduk, 1992, Kakitsubata et al., 2003, Munter et al., 2002), compromising the study of failure mechanisms and ensuing injury propagation. The optimization of clinical MRI for the spine is continually improving and the current state of *in vivo* detection of IVD injury is discussed in the following sections.

Annulus Fibrosus tear detection

Clinical use of MRI didn't evolve until the early 1980's, and at that point much of what could be diagnosed by abnormal MRI images was still unknown. Yu and Emans (1988) were one of the first groups to recognize annular tear morphology in MRI, and inspired Aprill and Bogduk (1992) to investigate what they defined as the High Intensity Zone (HIZ) appearance of annular tears in MRI scans (Yu et al., 1989, Aprill and Bogduk, 1992). Aprill and Bogduk (1992) prospectively assessed the sensitivity of MRI to annular tears by comparing MRI and CT-discography findings of patients referred for both diagnostic imaging modalities. Initial gains were achieved through specific MRI scanning protocols developed for annular tear detection, resulting in the detection of 54% of the tears detected by CT-discography, 63% of the IVDs that responded to CT-discography pain reproduction, and identification of 71% of IVDs with both CT-discographic tear detection *and* pain reproduction (Aprill and Bogduk, 1992). Though MRI was shown not to be as sensitive as CT-discography to tears in the AF, it did demonstrate the potential for strong diagnostic detection of disrupted and painful discs. The major limitations of this study, in addition to a number of other early attempts at detecting annular tears, were a function of mainly technological barriers (clinical MRI was still in its infancy) as well as a lack of experience in scanning the AF as opposed to the easier visualized NP (Osti and Fraser, 1992).

MRI contrast basics

To describe how MRI generates contrast between the structures of the IVD, the following section has been included to give an overview of MRI contrast basics.

Conventional MRI takes advantage of the large number of water molecules (H_2O) within the tissues of the body. The protons (H^+) of these water molecules are not static, and they are constantly spinning about a central axis, which corresponds to a general direction of magnetization. Because water is dipolar, these molecules will align themselves to a strong magnetic field. To be more specific, proton atoms in the body will spin, or *precess*, in a manner that preferentially aligns them parallel to a strong static magnetic field, polarizing the tissues within the field (Hashemi, Ray H., M.D., Bradley, & Lisanti, Christopher J., M.D., 2003) (Figure 16).

In MRI, the appropriate perturbation via gradients and RF coils can change (polarity/magnitude) the longitudinal and transverse components of proton precession about the static magnetic field (Figure 16). Any change in precession initiated through a perturbation of the system is temporary, and precession will eventually return to equilibrium. The return to equilibrium of the transverse component of proton precession creates a free induction decay that is captured by a RF coil, allowing for the production of signal in MRI (Hashemi, Ray H., M.D., Bradley, & Lisanti, Christopher J., M.D., 2003).

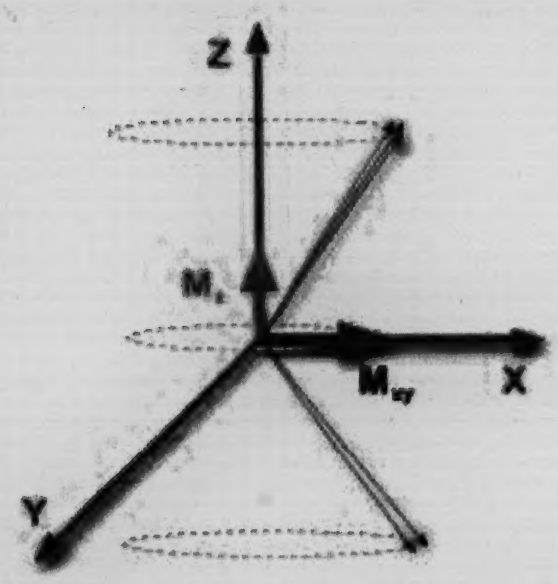

Figure 16. Transverse (Mxy) and longitudinal (Mz) magnetizations about the static field axis (image from http://en.wikibooks.org/wiki/Image:Excitation3_1.jpg)

Conventional means of generating contrast between tissue types in MRI is dependent on the rate of which a tissue's transverse (Mxy) and longitudinal (Mz) magnetizations return to equilibrium following a perturbation. These rates vary for biological materials (Table 1), and acquiring the signal generated by this return to equilibrium at different time intervals or echo times (TE) generate the contrast required to differentiate tissue types in MRI. Depending on what the tissue of interest is, contrast may be preferentially generated using transverse or T2 relaxation rates, or longitudinal or T1 relaxation rates (Hashemi, Ray H., M.D., Bradley, & Lisanti, Christopher J., M.D., 2003) (Figure 17). Generating contrast based on a tissues transverse, or longitudinal magnetization characteristics can lead to very different MRI visualization.

Tissue Type	T1 (msec)	T2 (msec)
Annulus Fibrosus	887	39*
Nucleus Pulposus	1179	56*
Liver	490	43
Muscle	870	47
Kidney	650	58
Lung	830	80
White Matter	790	92
Grey Matter	920	100
CSF	2 400	2 400

Table 1. Example of relaxation times for various tissues. Single * denotes T1 and T2 relaxation times from Chiu *et al.* (Chiu *et al.*, 2001), the remainder of relaxation times are from http.//en.wikibooks.org/wiki/Basic_Physics_of_Nuclear_Medicine/MRI_&_Nuclear_Medicine).

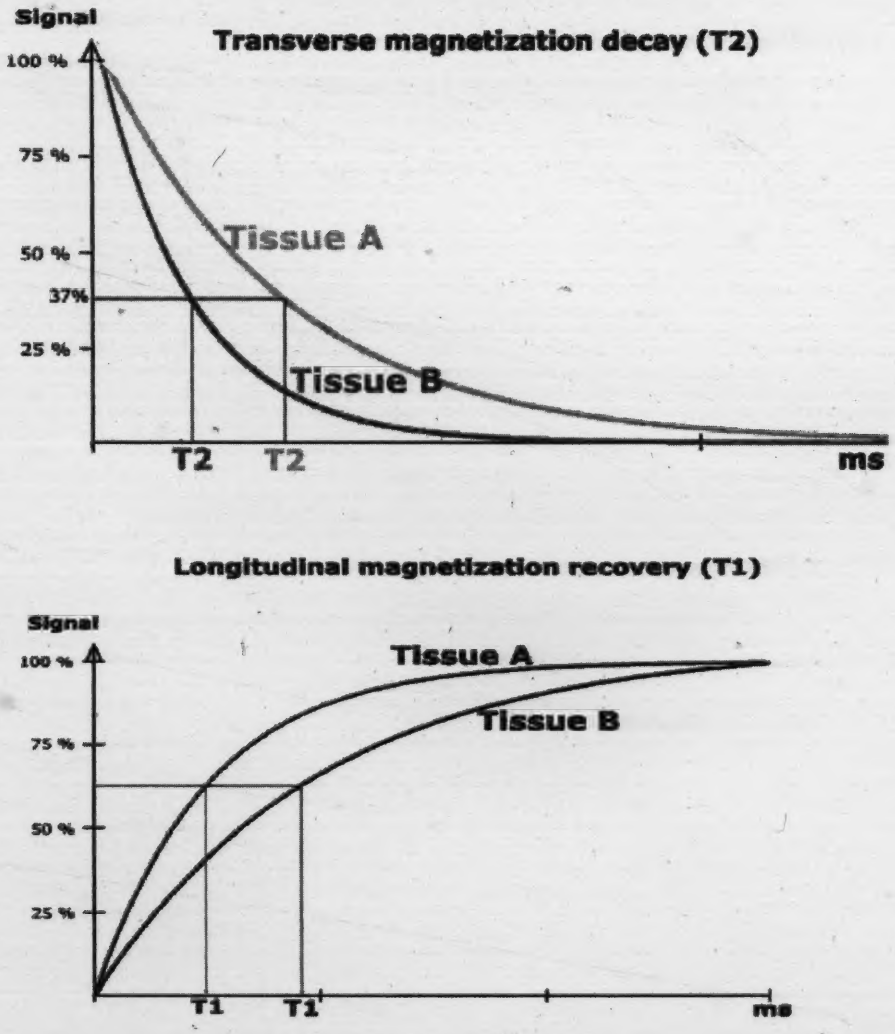

Figure 17. T2 weighted (T2W) (top) and T1 weighted (T1W) (bottom) MRI contrast generating schemes between 2 different tissues (Tissue A, Tissue B). Different levels of contrast generation between tissues A and B are achieved by sampling signals at different TEs (ms) denoted as T2 (dark) and T2 (light), T1 (light) and T1 (dark) (images from http.//www.e-mri.org/cours/Module_4_Signal/T2.gif).

Magnetic relaxation properties play an important role in the MRI visualization of different tissue types, but there are a number of other parameters that can make significant contributions to the differentiation of tissues (Hashemi, Ray H., M.D., Bradley, & Lisanti, Christopher J., M.D., 2003). Like CT, MRI generates images that are comprised of an array of pixels with a defined area and thickness, or voxels. The amount of signal available for MRI visualization is related to the volume of tissue visualized within these voxel, as well as the T1 and T2 relaxation rates. One potential issue with generating contrast between tissues is the size of these voxels. The presence of more than one tissue type within a voxel can lead to a problem called partial volume effects. This occurs when the visualization from a specific anatomical region is misrepresented because nearby tissue is included in the imaging voxel. To reduce the impact of partial volume effects, voxel sizes can be decreased, increasing image resolution, but resulting in less available signal for contrast generation. On the other hand, if resolution is decreased to improve signal availability, tissue visualization may be misleading (Hashemi, Ray H., M.D., Bradley, & Lisanti, Christopher J., M.D., 2003).

To maximize signal availability from target tissues, and limit the partial volume effects present in images, MRI slices can be oriented so that they fall directly on the tissues of interest. Despite the optimization of both voxel size and slice planes, MRI visualization of tissues may still exhibit low contrast. If this is the case, and the area of interest is stationary (e.g. no motion, pulsatile flow), multiple scans or "averages", can be taken and then combined to improve the signal acquired for tissue visualization, though improvements in signal strength may not yield considerable improvements in tissue contrast (Hashemi, Ray H., M.D., Bradley, & Lisanti, Christopher J., M.D., 2003).

Overall, the ability of MRI to generate contrast between tissues is dependent on how the imaging parameters influence signal availability, which is most often described through the Signal to Noise Ratio (SNR) and/or Contrast to Noise Ratio (CNR) (Hashemi, Ray H., M.D., Bradley, & Lisanti, Christopher J., M.D., 2003). Noise within MRI visualizations erodes the contrast between tissues, especially if there are low signal levels. Low SNR and CNR can be a result of the imaging parameters selected, or

sometimes it is caused by the signal availability from tissues of interest being low without significant noise components due to relaxation properties that are difficult for basic MRI to capture.

Clinical MRI protocol of the IVD

Returning to the MRI evaluation of IVDs, the normal clinical protocol for lumbar spine IVD visualization is a sagittal scan of the whole lumbar spine followed by an axial scan that encompasses the last three lumbar IVDs. This protocol is done with both T1 and T2 weighting.

The sagittal T1W scans do not differentiate between the NP and inner AF. Both appear like a singular entity; hyperintense compared to the outer AF (Figure 18). In healthy IVDs the exterior boundaries of the outer AF are delineated by the hyperintense Posterior and Anterior longitudinal ligaments, and the signal void of the endplates, providing a relatively clear image of the gross size of the IVD (Morgan and Saifuddin, 1999, Nguyen-minh et al., 1997). Aside from detectable injury induced geometric changes, T1W scans with gadolinium contrast agents result in hyperintense visualization of the NP and AF tears (Modic and Ross, 1991) (Figure 18).

Sagittal T2W images of the IVD show a hyperintense, yet indistinguishable NP and inner AF (Morgan and Saifuddin, 1999, Roberts et al., 1998). The outer AF has a very short transverse relaxation time leading to poor T2W visualization, yet it is distinguishable as a signal void surrounding the hyperintense NP/inner AF, and bound by the CSF on the posterior side of the IVD, and the paraspinal tissue on the anterior side of the IVD (Roberts et al., 1998) (Figure 18). Any increase in intradiscal water through trauma will cause a hyperintensity in T2W images. Corresponding to annular tears, HIZs are identifiable even at low magnet strengths using T2W scans (Aprill and Bogduk, 1992) (Figure 18). The results from Kakitsubata *et al.* suggest T1W gadolinium contrast enhancement HIZ detection is more sensitive to radial tears, and T2W transverse tear detection is more sensitive to transverse tears. Both T2W and T1W gadolinium enhanced detection of concentric tears is low (Kakitsubata et al., 2003).

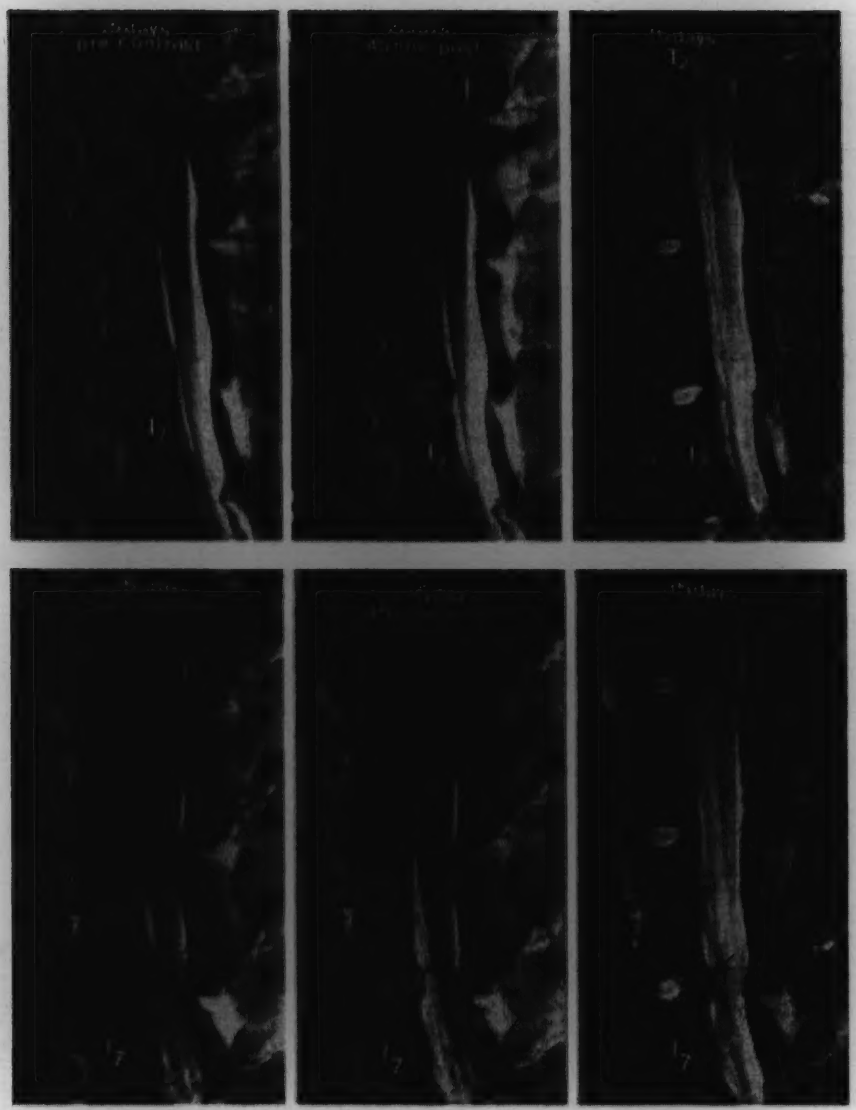

Figure 18. 2 canine specimen imaged 15 days following stab injury and nuclear material extraction (top and bottom rows). The imaging protocol included T1W (500 msec TR, 20msec TE, 2avg) (A), T1W following contrast injection (B), T2W scan (2000 msec TR, 88msec TE, 2avg) (C). No change from baseline for the first animal, noticeable change through HIZ visualization in the second animal identified by arrows (Nguyen-minh et al., 1997).

Axial T1W, and T2W images readily show the NP and inner AF, while the short TE of the outer AF makes its visualization very difficult, especially for T2W scans. Clinically, axial scans of the IVD are included in a spinal imaging protocol for the visualization of the dorsal and ventral roots of the spinal cord, but not for inspection of tears in the AF. In one of the few studies that include a axial plane evaluation of IVD injury specifically, Yu *et al.* were only able to identify changes to the NP and external boundaries of the IVD, where as sagittal images of the same discs identified changes within the NP and AF (Yu et al., 2003).

Clinical AF tear detection - deficiencies

Conventional MRI or T1W and T2W MRI images, readily show the NP and inner AF, however, there are still some considerable difficulties visualizing the middle and outer AF. A good T2W MRI signal from the AF is very difficult to achieve, because it has such a short transverse relaxation time, and the presence of HIZs indicating annular tears is usually dependent on other material from outside of the annulus filling these clefts (Osti and Fraser, 1992).

Yu *et al.* utilized cyclic loading to generate injuries in the AF of lumbar IVDs. Upon geometric measurements following dissection, multiple injuries were identified in the AF, of which only those that communicated with the NP were definitively detected using conventional MRI (Yu et al., 2003). To mimick the process of CT-discography tear enhancement, Kakitsubata *et al.* evaluated the diagnostic capabilities of MRI-discography using gadolinium (Kakitsubata et al., 2003). Compared to normal contrast enhanced T1W scans, MRI discography showed a further increase in signal from HIZ communicating with the NP. Though a significantly higher percentage of radial tears were detected (100%), just 57% of the transverse tears were detected and 21% of concentric tears (Kakitsubata et al., 2003), and these tears make up 2/3 of the histological identified tear types (Kakitsubata et al., 2003).

The importance of clinical MRI tear detection is coming under increasing skepticism. Not only does it seem as if *in vivo* tear detection is inconsistent, both asymptomatic and symptomatic populations can exhibit AF tear morphology (Boden et al., 1990, Munter et al., 2002). Despite improvements in HIZ resolution from better MRI technology and IVD specific MRI scanning sequences (Haughton, 2004), the detection of tears within the AF of IVDs using MRI is not improving. Given that the dominant mechanism of annular tear detection is the visualization of the material that has filled the tears over time (Modic and Ross, 1991), small faults in the AF could propagate over time and transform into the larger, MRI visible tears. If this is indeed the case, traditional clinically available MRI sequences for tear detection may not be able to reach a point of proficiency where small structural changes in the AF are visible. Yet these small tears may sufficiently destabilize the motion units causing pain. It is for these reasons that alternatives to conventional clinical MRI of the IVD must be routinely explored.

2.5 *Improving tear detection using MRI:*

In general, using MRI to generate images of the spine has traditionally introduced challenges. Because of differences in magnetic susceptibilities, the presence of bone as well as the proximity of air-tissue interfaces disturbs the uniform magnetic field about the IVD tissue. This disturbance introduces distortions into the MRI images. Also, the high collagen content in the AF is what reduces its transverse relaxation times, making it very difficult to visualize small morphological changes in the AF with MRI.

When considering tears in the AF, the focus must be on optimizing T2W imaging since T1W doesn't clearly differentiate between the NP and AF. Preliminary quantitative work by the authors is in agreement with reported values of the T2 relaxation time of AF tissue being approximately 35-40msec (Chiu et al., 2001, Drew et al., 2004), and this low T2 relaxation time introduces challenges, because the available TEs for most T2W based sequences on a clinical scanners do not normally reduce to this level. This results in very little signal available from the AF for conventional MRI visualization (Gatehouse and Bydder, 2003). The lack of signal can be beneficial when material with a longer T2

relaxation time infiltrates the annular space (Aprill and Bogduk, 1992, Saifuddin, McSweeney, & Lehovsky, 2003), but if no material has migrated, visualization of early onset of injury is highly unlikely.

Despite continual improvements in MRI hardware and magnet strength, neither traditional T1W nor T2W scanning protocols have been particularly sensitive to annular tears (Haughton, 2004). Innovative MRI techniques have been presented by a number of researchers as potential solutions to the low sensitivity in AF tear detection using MRI, and most of these techniques focus on improving the low signal availability from the AF. The following section is a summary of the 3 most promising techniques to date.

Magic angle

Signal from the collagen in cartilage and ligaments has been shown to have preferential orientation in a magnetic field, resulting in a spectrum of relaxation rates (Berendsen, 1962). Signal from these tissues are maximized when the normal to the tissue surface is ±55° degrees with respect to the static magnetic field (Fullerton, Cameron, & Ord, 1985, Henkelman, Stanisz, & Graham, 2001). Ignoring the structural variations in the AF, the annular fibres are reported to be inclined at approximately ±30° to the transverse plane; already placing most of the AF fibres within the optimal window.

Ultra Short TE

Depending on the percentage of long versus short T2 components of adjacent tissues, speed of acquisition can increase the conspicuity of the tissue of interest, or limit the signal from other tissues (Gatehouse and Bydder, 2003). Studies that have documented the detection of pathologies using Ultra Short Echo Time (UTE) imaging show increased conspicuity of tissues with shorter TEs. However, the loss of order in tissue and the increase in free water, such as in annular tears, have been hypothesized to decrease the short T2 components in an injury area (Gatehouse and Bydder, 2003). Given its purpose, in this potential application of UTE, to increase the available signal from the AF to detect annular tears may in fact inhibit tear detection.

Quantitative T2

Changes in water content, loss of order in tissue, or changes in macromolecular content through injury, may shift the amount of short and long T2 components in a tissue sufficiently to detect the overall change in T2 relaxation time (Boos et al., 1993, Gatehouse and Bydder, 2003). There has been some interest in quantitative T2 of the AF, but this has mostly been focused on compression schemes and how fluid flow from the NP into the AF affects T2 relaxation rates. Chiu *et al.* reported no significant change between the measured T2 of the AF in the loaded and unloaded states, whereas, Drew *et al.* did see an increase in T2 during the initial loading (Chiu et al., 2001, Drew et al., 2004). The most beneficial case for the detection of AF tears, which has not yet been reported, would be if there was no change in T2 of the AF following the loading of a healthy IVD, so any potential relaxation rates change within or near an annular tear could be attributed directly to an injury.

2.6 *Functional AF tear detection:*

The novel MRI techniques presented in the last section may or may not have the potential to address conventional MRI's deficiencies in visualizing high collagen content tissues show promise. However, in terms of improved visualization of the AF, investigating a MRI technique that is easier to implement in a clinical setting may yield more relevant annular tear information. Because of the paired mechanical and hydrostatic systems of the IVD, structural damage to the AF may sufficiently disturb the normal hydrostatic system, such that changes in diffusion characteristics are visible using clinically available diffusion MRI sequences.

As described in the Chapter 1, diffusion MRI may provide an excellent opportunity for improving the current state of annular tear detection (Haughton, 2004). Its clinical use for spinal scans will meet considerable challenges due to the susceptibility and short transverse relaxation difficulties in imaging this anatomical region (Holder, 2000). Yet despite any difficulties, compared to the potential strategies discussed in the last section, diffusion MRI has considerable potential in the detection of AF tears, especially if fluid movement is induced concurrently through dynamic compression.

Diffusion MRI basics

The microscopic movement of fluid within tissues is a function of either isotropic or anisotropic diffusion (Tofts, 2003). In this context, isotropic diffusion refers to the random movement of fluid within a tissue when there is very little directional impedance due to biological barriers. Anisotropic diffusion refers to situations where biological barriers considerably influence the direction of fluid movement within a tissue. To summarize the basic difference between conventional and diffusion MRI, conventional MRI techniques visualize tissues based on the amount of water molecules in a given tissue and/or their relaxation properties, while diffusion MRI adds to this by introducing signal attenuation based on the amount of water movement in random versus restricted directions (Tofts, 2003).

The basic form of a diffusion MRI sequence is a standard T2W spin echo sequence with the application of a pulsed field gradient (PFG); specifically, firing two gradient pulses of a specific strength for a fixed time, on either sides of a 180°, refocusing pulse (Stejskal and Tanner, 1965) (Figure 19).

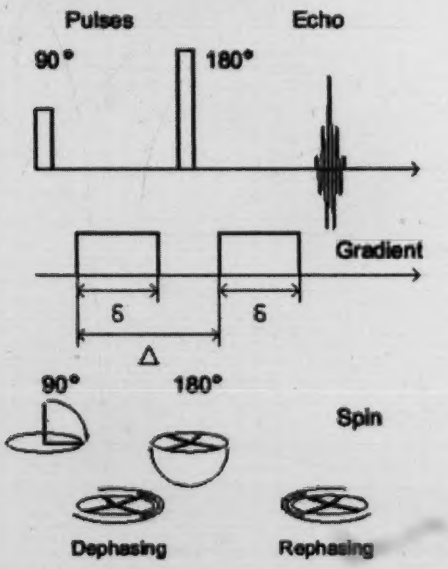

Figure 19. Diffusion gradients and phase accumulation of moving protons (image from http://www.rsierra.com/DA/).

Magnetic spins of stationary molecules will not incur a net phase; however, protons that have moved will experience a net attenuation of transverse magnetization due to phase accumulation. Diffusion weighted images (DWIs) have darker areas corresponding to high water diffusion (Figure 20). The amount of signal following diffusion attenuation is given by the following expressions (Stejskal and Tanner, 1965).

$$A = A_0 e^{-D\gamma^2 G^2 \delta^2 (\Delta - \delta/3)} \quad (1)$$

$$A = A_0 e^{-bD} \quad (2)$$

Where D is the diffusion coefficient, γ is the proton gyromagnetic ratio, G is the gradient strength, δ is the duration of encoding gradient, and $\Delta - \delta/3$ is the diffusion time. As can be seen in Eq. (2), the specifics related to the PFG from Eq. (1) is described using b (s/mm^2), $b = \gamma^2 G^2 \delta^2 (\Delta - \delta/3)$, which is used to describe the strength and duration of the diffusion sequence (Tofts, 2003). To determine the coefficient of diffusion, D (mm^2/s), of a region of interest, the natural log of the ratio between two signals, one acquired with a PFG ($b \neq 0$) and one without ($b = 0$), is taken (Eq.3) (Tofts, 2003).

$$\ln \frac{S(TE,b)}{S(TE,0)} = -bD \quad (3)$$

The b values are used to compare diffusion images, with larger b values resulting in increased diffusion weighting. To achieve reasonable diffusion attenuation, long diffusion times are usually required, which is an issue for scanning the AF as there is very little signal available to attenuate due to diffusion sequence's long TEs of 80-100msec.

Apparent Diffusion Coefficient maps

Because biological barriers can influence the magnitude of water diffusion in any one direction, D is highly dependent on the orientation of the diffusion gradients. To acknowledge the variability of water diffusion given different diffusion gradient

directions, D is referred to as the Apparent Diffusion Coefficient (ADC). The practical application of the ADC parameter is the generation of quantitative maps that quantify the average isotropic diffusion in tissues (Dong et al., 2004, Trudeau, Dixon, & Hawkins, 1995). To reduce the directional dependence, an average ADC is typically calculated using ADCs generated in three orthogonal directions. The average ADC values are then mapped to each voxel where MRI visualization intensity corresponds to the inverse of the ADC magnitude (Figure 20).

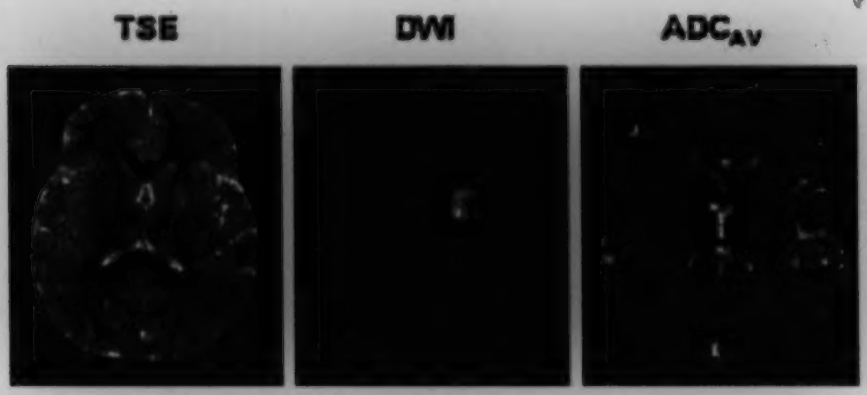

Figure 20. Comparison of a proton density with diffusion weighted MRI and ADC visualization of ischemic stroke (Thomas et al., 2000).

The Diffusion Tensor

To best understand the diffusion properties within a tissue structure, the diffusion tensor (DT) is used. This diffusion MRI sequence reflects the complete directional properties of diffusion within a voxel. In order to calculate the DT, six DWI acquisitions must be performed, in addition to one nonDWI (b=0) (Tofts, 2003). A matrix reflecting each of the diffusion gradient directions with the six corresponding diffusion coefficients derived from Eq.3, is then reduced to its diagonals resulting in the eigenvectors of the DT and their scalar eigenvalues. The mean of each voxel's direction dependent diffusion characteristics can be expressed as the TraceADC (mm^2/s) DT measure. This quantitative DT measure characterizes the isotropic diffusion properties of a voxel. Similarly, the Fractional Anisotropy (FA) (ratio: 0 to 1) measure, also calculated from the

DT, characterizes the anisotropic properties of diffusion within a voxel by giving an estimate of what portion (fraction) of diffusion is anisotropic. Like ADC, the DT measures can be mapped to voxels for visual assessment using DT imaging (DTI) (Tofts, 2003).

2.7 *Diffusion MRI of the IVD:*

Diffusion MRI has recently made substantial clinical contributions as a new strategy for visualizing morphology, pathology, and physiology of a range of tissues (Rowley, Grant, & Roberts, 1999). Taking advantage of the biological barriers in tissues, MRI can use fluid undergoing isotropic and anisotropic diffusion to generate contrast (Newitt and Majumdar, 2005). One of the most successful applications of diffusion imaging has been in stroke detection (Warach, Dashe, & Edelman, 1996). In terms of diffusion MRI applications within the IVD, a considerable amount of mobile fluid is in both the NP and AF, and some diffusion MRI studies have already been conducted to characterize the diurnal fluid levels of healthy and degenerated IVDs (Antoniou et al., 2004, Drew et al., 2004, Kraemer, Kolditz, & Gowin, 1985).

An eloquent study conducted by Kerttulla *et al.* illustrated diffusion MRI's ability to detect changes in IVD morphology that T2W conventional MRI indicated was normal. Youth treated for vertebral compression fractures at least one year previous, were found to have significantly lower ADC in the NP and inner AF then when initially treated (Kerttula et al., 2001). Despite the normal T2W appearance, ADC measurements seemed to be sensitive to changes in IVD tissue. Trauma to the NP and inner AF generally result in the dehydration and thickening of the proteoglycan matrixes, thus a loss of water content and isotropic diffusion (Gu et al., 1999). This study showed that structural changes in the IVD inconspicuous to conventional MRI sequences *can* be detected using diffusion MRI, and that annular tear detection may be within the realm of possibility using diffusion MRI. Changes to biological boundaries has also been shown to affect ADC levels (Tofts, 2003), yet to our knowledge, there has been no attempt to *detect* AF tears using ADCs.

While Kertulla *et al.* used ADC to evaluate the health of IVD, Hsu *et al.* used a DTI sequence to fully characterize the magnitude and directional information of the anisotropic diffusion properties of a healthy section of porcine AF (Hsu and Setton, 1999). Though the magnet strength (7 Tesla (T)) used in this study was much larger than anything currently clinically available (1.5, 3T), the information collected by the DTI sequence allowed the visualization, *in situ*, of the space between healthy lamellae of an IVD (Hsu and Setton, 1999) (Figure 21).

Figure 21. *In situ* sample of AF imaged using DWI at 7.1T magnet. Able to generate DTI set for diffusion direction information (Hsu and Setton, 1999).

To our knowledge, there has been no attempt to detect AF tears using diffusion MRI at clinical magnet strengths (1.5T). For cases where fluid diffusion could be anisotropic, such as the space within an annular tear, the DTI sequence may be able to reflect an injury's diffusion properties. Out of the DT, five rotationally invariant measures can be extracted; TraceADC, three eigenvalues that represent the ADCs in three orthogonal directions oriented along the tissue axis, and Fractional Anisotropy. One of these DT measures may provide an excellent opportunity for improving the current state of annular tear detection (Haughton, 2004).

Challenges regarding the use of Diffusion MRI

Generating diffusion images requires an increase in TE since additional gradient pulses need to be accommodated (Le Bihan et al., 2006). Recalling that the AF is poorly visualized because of its short T2 components, any addition in TE will result in a reduction of SNR from the entire AF, in addition to any losses induced by the diffusion gradients (Le Bihan et al., 2006). The NP is well visualized with T2W based sequences, so there is no significant impact on the signal available from that region of the IVD. Depending on the strength and profiles of these diffusion gradients, the rapid switching on and off of these gradients can also induce eddy currents, which can artificially scale up or down the actual gradients experienced by the voxels resulting in inaccurate DT calculations (Le Bihan et al., 2006). These factors can also lead to contracted or dilated, shifted and sheared geometric distortions in the diffusion images (Le Bihan et al., 2006).

To accomplish DTI there is an increase in the total amount of images acquired during a basic diffusion sequence. Diffusion images have to be generated using a number of gradient directions, and this dramatically slows down the imaging process (Hashemi, Ray H., M.D., Bradley, & Lisanti, Christopher J., M.D., 2003). Any movement in the tissue aside from anisotropic or isotropic fluid diffusion will then have increased opportunities to cause motion artifacts within the images (Le Bihan et al., 2006).

As noted, the presence of many tissue types within the field of view (FOV) of a lumbar IVD scans introduces unique challenges to generating anatomically accurate images. The visualization of a slice of tissue using MRI is dependent on achieving a linearly varying magnetic field along the FOV for the purposes of spatially encoding voxels. Tissues exhibit different magnetization properties cause local disruptions in the linearly varying field to evolve, such that the MRI images have voxels that are shifted into other position (Hashemi, Ray H., M.D., Bradley, & Lisanti, Christopher J., M.D., 2003). This shifting of the image is an artifact that increases with not only the dramatic changes in signal availability (i.e. NP and AF), but also with the introduction of diffusion gradient magnetization profiles, which further disturb the linearly varying magnetic field (Le Bihan et al., 2006, Trudeau, Dixon, & Hawkins, 1995).

Because diffusion MRI generates contrast by introducing signal attenuation in voxels undergoing isotropic or anisotropic diffusion, tissues with limited signal availability are not well imaged using diffusion protocols. Achieving meaningful results from diffusion MRI sequences is not necessarily dependent on generating excellent anatomical images, and for this reason, lower resolution parameters are often preferred for diffusion MRI sequences in order to increase the SNR for tissues of interest (Le Bihan et al., 2006). It must also be noted that the use of lower resolution parameters, increases the risk of artificially amplifying signal availability through partial volume effects (Le Bihan et al., 2006). Also, regarding the quantitative diffusion MRI sequences (ADC, DTI), inclusion of information outside of the tissue of interest can lead to inaccurate results (Le Bihan et al., 2006, Trudeau, Dixon, & Hawkins, 1995).

SNR, artifacts, resolution and partial volume effects are all challenges that must be addressed when using diffusion MRI, but in the case of the AF, these factors limit its application. Preliminary work by the author has described that reducing the impact of one of these factors invariable increases the impact of another. The challenge has now become minimizing the negative effects as much as possible, while ultimately achieving a result that can contribute to answering some of the outstanding questions regarding AF tears and LBP.

Echo Planar Imaging

Given the unique challenges that diffusion MRI faces, various techniques have been explored to ameliorate some of these existing issues. One such technique is EPI. EPI is an extremely fast signal acquisition scheme that can significantly reduce acquisition time by acquiring all the phase information from a slice in one acquisition (Hashemi, Ray H., M.D., Bradley, & Lisanti, Christopher J., M.D., 2003) (Figures 22). In comparison, conventional MRI has a single acquisition for each phase encode until k-space is filled. With the clinical implementation of EPI, dramatic reductions in acquisition times have been achieved. These reductions have significantly reduced the opportunity for artifact causing movement in the body to be captured by MRI. The fast acquisition time also means that the multiple images required for DTI, can be acquired in an acceptable imaging time.

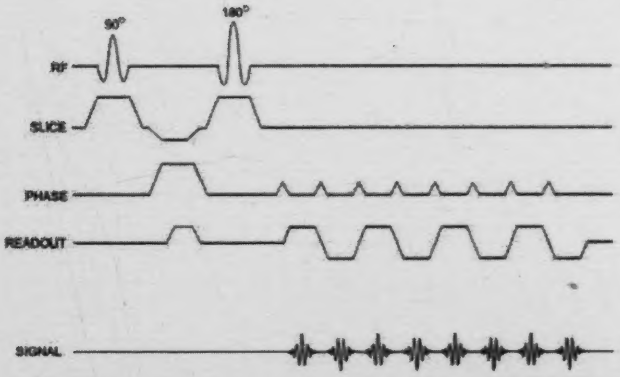

Figure 22. EPI gradient scheme. Between multiple readouts phase encodes allow signal to be stepped through k-space (image from http://bitc.bme.emory.edu/images/epi_pt_1.jpg).

Unfortunately, despite the contribution in reducing acquisition times, thereby reducing motion artifacts, cycling through numerous phase encoding gradients further contributes to geometric distortions through evolving eddy currents, and the accumulation of phase between adjacent voxels (Le Bihan et al., 2006). The increased amount of gradient activity during EPI based sequences must also be of concern given that the body absorbs a portion of the energy from MRI RF pulses (Shellock, 2000). Finally, due to hardware limitations and adjustments for SNR reductions, EPI spatial resolution is typically less than conventional sequences (Le Bihan et al., 2006).

Parallel Imaging (SENSE)

Parallel imaging is an extremely versatile MRI application that reduces the number of phase encode steps required to generate a complete image, and it can be coupled with most conventional MRI techniques, including EPI (Bammer et al., 2002). Though there are some SNR implications with its implementation, parallel imaging has been shown to have the capability of reducing the negative effects in images from EPI sequences (Bammer et al., 2002).

The ongoing clinical utility of MRI requires constant innovation for new ways of generating contrast between tissues while clearly visualizing anatomy. Yet, this has to be

accomplished in a timely fashion. Parallel imaging reduces both image artifacts and the TE in MRI sequences (Larkman and Nunes, 2007). Because the process of phase encoding is what is time consuming regarding conventional visualization, parallel imaging works by acquiring less phase encoding information and then using post-processing to produce complete images (Larkman and Nunes, 2007).

Sensitivity encoding or SENSE, one parallel imaging techniques, acquires a reduced set of phase encodes, creating an incomplete data set and thus an aliased image (Larkman and Nunes, 2007). The use of multiple receiver coils, with different spatial sensitivities profiles within a multi-element RF coil or array (Figure 36), allows for the unwrapping of the aliased component from the image at any location (Hashemi, Ray H., M.D., Bradley, & Lisanti, Christopher J., M.D., 2003). Each coil will acquire a certain amount of signal for each position along a reduced FOV (Hashemi, Ray H., M.D., Bradley, & Lisanti, Christopher J., M.D., 2003). An algorithm derived from the coil sensitivity profiles, separates the aliased image and rebuilds a complete image (Lupo et al., 2006) (Figure 23). SENSE can reduce TEs (Jaermann et al., 2006) and artifacts (Le Bihan et al., 2006, Lupo et al., 2006), but it also comes at the expense of SNR (Lupo et al., 2006, Ruel et al., 2004). In fact, SNR will decrease at approximately the square root of the factor of reduced phase encode lines (Lupo et al., 2006). Considering that SENSE is a technique that can reduce TEs, this may boost the baseline signal levels acquired from the AF.

Figure 23. An example of a 4 channel spinal array where each coil acquired a partial data set which was used to construct the final image on a pixel by pixel basis (Larkman and Nunes, 2007).

The combination of SENSE and EPI has allowed for the best characteristics of both techniques to be applied in the improvement of clinical diffusion MRI. The first study to evaluate DTI using single-shot SENSE-EPI demonstrated excellent results with both the imaging of the brain, and the quantitative data generated for the brain (Bammer et al., 2002) (Figure 24). As mentioned, no studies to date have looked at investigating tears in the AF using DTI at clinical magnet strengths (1.5T). Given the unique challenges with visualizing the AF and tears within the annulus using conventional MRI, EPI and SENSE may provide the keys elements that will improve image quality of IVD DTI, aiding in the early detection of AF tears either through direct visualization or through analyzing the diffusion characteristics quantified by the DTI.

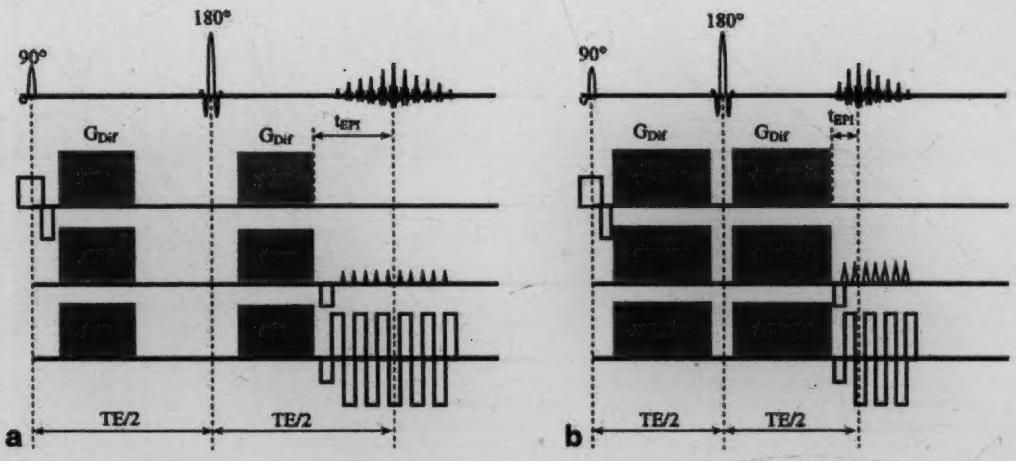

Figure 24. The use of SENSE encoding further improved on the unique advantages of applying EPI to Diffusion-weighted sequence. a) Conventional EPI Diffusion pulse sequence. b) Altered sequence for SENSE application. The EPI echo train is further reduced with SENSE and a much shorter TE for a given diffusion attenuation is possible. (Bammer et al., 2002).

2.8 *Dynamic MRI:*

Compressive loading during conventional MRI scans of the IVD has been extensively used *in vitro* to investigate the diurnal cycle of the IVD (Adams, Dolan, & Hutton, 1987, Botsford, Esses, & Ogilvie-Harris, 1994, Malko, Hutton, & Fajman, 1999), infer the diffusion pathways within the IVD during fluid exudation and uptake (Ferguson, Ito, & Nolte, 2004), describe structural changes under load (Karakida et al., 2003, Malko, Hutton, & Fajman, 1999), and measure IVD hydration under load (Lee et al., 2005). As dynamic loading pertains to this study, tears in the AF may become more conspicuous, providing a better opportunity for visualization and better signal for DTI calculations. The presence of tears in the AF may also alter normal water diffusion characteristics within the AF during compression of the IVD (Chiu et al., 2001, Drew et al., 2004).

The use of quantitative MRI (T1 and T2 relaxation times) has already augmented the qualitative description of fluid content in the IVD under various compressive circumstances (Boos et al., 1993, Roberts, 2002), but quantitative descriptions of how

fluid content reaches these reported levels remains poorly understood. One of the first studies to not only report overall changes in relaxation parameters (relaxation times), implemented a diffusion - dynamic MRI experimental protocol. Chiu *et al.* preloaded human lumbar spine segments stripped of all paravertebral tissue in isotonic saline. Positioning the spine segments head first into the MRI bore, step loading at 700N/20cm^2 during conventional and diffusion MRI scanning at 1.5T was conducted (Chiu et al., 2001). The results showed that there was a significant increase in T1 relaxation time in the NP and AF under load, and a non-significant increase was observed in the T2 relaxation time of the NP and AF (Chiu et al., 2001). Increases in T1 and T2 can be related to changes in water content, and under load the proteoglycan matrixes release bound water. The diffusion MRI results provided a more complete description of the changes in diffusion related to loading, as there was not only a significant increase in diffusion, but the proportion of diffusion occurring in different directions changed as well. Specifically, diffusion in the z direction was highest under both loading conditions, but under a load, the increase in observed diffusion was largest in the x and y directions (Chiu et al., 2001). One potential interpretation of these results is that the IVD's response to load increases diffusion towards the AF. Acknowledging that loading protocols, sample preparation, and an assortment of other factors can have significant impacts on diffusion within the IVD, this study just highlights the strengths of quantitative diffusion MRI in describing fluid diffusion, and how by comparing diffusion under different loading environment the function of the IVD can be better understood.

2.9 *Literature review summary:*

In addition to the direct detection of tears in the AF, their existence in the AF may prove to alter the diffusion pathways in the IVD sufficiently, such that their detection is possible using diffusion MRI sequences. Though diffusion MRI of the NP has been explored, and conventional MRI can infer degenerative changes through visualization of the NP, the role of AF injuries on the "function" of the IVD has not realized many successes with medical imaging.

Despite ongoing advancements in conventional MRI detection of IVD injuries, the difficulties associated with adequate visualization of the AF begs for an alternative to traditional clinical MRI sequences. The well-defined biological barriers present in the AF, and the complex fluid exchange processes of the IVD make diffusion MRI an attractive MRI contrast-generating scheme. The addition of techniques such as EPI and SENSE as well as functional movement (dynamic loading) may boost the effectiveness of this exciting functional imaging scheme.

Diffusion MRI, but more specifically DTI has already made significant impacts on the study of a number of diseases. There a is real opportunity to generate breakthroughs with the use of DTI toward increasing the understanding of the function of the IVD, and how it is impacted by injuries to the AF. The study of LBP, and the impacts of AF injuries are in need of additional tools, and the combination of dynamic MRI and DTI may provide that opportunity.

Chapter 2 references

Adams, M.A., 2004. Biomechanics of back pain. Acupunct. Med. 224, 178-188.

Adams, M.A., Dolan, P., 2005. Spine biomechanics. J. Biomech. 3810, 1972-1983.

Adams, M.A., Dolan, P., Hutton, W.C., 1987. Diurnal variations in the stresses on the lumbar spine. Spine. 122, 130-137.

Adams, M.A., McNally, D.S., Dolan, P., 1996. 'Stress' distributions inside intervertebral discs. The effects of age and degeneration. J. Bone Joint Surg. Br. 786, 965-972.

Adams, M.A., Roughley, P.J., 2006. What is intervertebral disc degeneration, and what causes it? Spine. 3118, 2151-2161.

An, H.S., Anderson, P.A., Haughton, V.M., Iatridis, J.C., Kang, J.D., Lotz, J.C., Natarajan, R.N., Oegema, T.R.,Jr, Roughley, P., Setton, L.A., Urban, J.P., Videman, T., Andersson, G.B., Weinstein, J.N., 2004. Introduction: disc degeneration: summary. Spine. 2923, 2677-2678.

Antoniou, J., Demers, C.N., Beaudoin, G., Goswami, T., Mwale, F., Aebi, M., Alini, M., 2004. Apparent diffusion coefficient of intervertebral discs related to matrix composition and integrity. Magn. Reson. Imaging. 227, 963-972.

Aprill, C., Bogduk, N., 1992. High-intensity zone: a diagnostic sign of painful lumbar disc on magnetic resonance imaging. Br. J. Radiol. 65773, 361-369.

Ayotte, D.C., Ito, K., Tepic, S., 2001. Direction-dependent resistance to flow in the endplate of the intervertebral disc: an ex vivo study. J. Orthop. Res. 196, 1073-1077.

Baer, A.E., Laursen, T.A., Guilak, F., Setton, L.A., 2003. The micromechanical environment of intervertebral disc cells determined by a finite deformation, anisotropic, and biphasic finite element model. J. Biomech. Eng. 1251, 1-11.

Bammer, R., Auer, M., Keeling, S.L., Augustin, M., Stables, L.A., Prokesch, R.W., Stollberger, R., Moseley, M.E., Fazekas, F., 2002. Diffusion tensor imaging using single-shot SENSE-EPI. Magn. Reson. Med. 481, 128-136.

Bass, E.C., Duncan, N.A., Hariharan, J.S., Dusick, J., Bueff, H.U., Lotz, J.C., 1997. Frozen storage affects the compressive creep behavior of the porcine intervertebral disc. Spine. 2224, 2867-2876.

Berendsen, H.J.C., 1962. Nuclear Magnetic Resonance Study of Collagen Hydration. J. Chem. Phys. 3612, 3297-&.

Boden, S.D., Davis, D.O., Dina, T.S., Patronas, N.J., Wiesel, S.W., 1990. Abnormal magnetic-resonance scans of the lumbar spine in asymptomatic subjects. A prospective investigation. J. Bone Joint Surg. Am. 723, 403-408.

Boos, N., Wallin, A., Gbedegbegnon, T., Aebi, M., Boesch, C., 1993. Quantitative MR imaging of lumbar intervertebral disks and vertebral bodies: influence of diurnal water content variations. Radiology. 1882, 351-354.

Botsford, D.J., Esses, S.I., Ogilvie-Harris, D.J., 1994. In vivo diurnal variation in intervertebral disc volume and morphology. Spine. 198, 935-940.

Brinckmann, P., Frobin, W., Hierholzer, E., Horst, M., 1983. Deformation of the vertebral end-plate under axial loading of the spine. Spine. 88, 851-856.

Brinckmann, P., Horst, M., 1985. The influence of vertebral body fracture, intradiscal injection, and partial discectomy on the radial bulge and height of human lumbar discs. Spine. 102, 138-145.

Brinkmann, P., Frobin, W., Leivseth, G., 2002. Mechanical Aspects of the Lumbar Spine in: Bergman, C., Griesbach, S., (Eds),Musculoskeletal Biomechanics, one ed. Thieme, Stuttgart;New York, pp. 105-128.

Broberg, K.B., 1993. Slow deformation of intervertebral discs. J. Biomech. 264-5, 501-512.

Buirski, G., Silberstein, M., 1993. The symptomatic lumbar disc in patients with low-back pain. Magnetic resonance imaging appearances in both a symptomatic and control population. Spine. 1813, 1808-1811.

Bydder, G.M., 2002. New approaches to magnetic resonance imaging of intervertebral discs, tendons, ligaments, and menisci. Spine. 2712, 1264-1268.

Cassidy, J.J., Hiltner, A., Baer, E., 1989. Hierarchical structure of the intervertebral disc. Connect. Tissue Res. 231, 75-88.

Chiu, E.J., Newitt, D.C., Segal, M.R., Hu, S.S., Lotz, J.C., Majumdar, S., 2001. Magnetic resonance imaging measurement of relaxation and water diffusion in the human lumbar intervertebral disc under compression in vitro. Spine. 2619, E437-44.

Coventry, M.B., Ghormley, R.K., Kernohan, J.W., 1945. THE INTERVERTEBRAL DISC: ITS MICROSCOPIC ANATOMY AND PATHOLOGY: Part I. Anatomy, Development, and Physiology. J Bone Joint Surg Am. 271, 105-112.

Crock, H.V., 1986. Internal disc disruption. A challenge to disc prolapse fifty years on. Spine. 116, 650-653.

Dong, Q., Welsh, R.C., Chenevert, T.L., Carlos, R.C., Maly-Sundgren, P., Gomez-Hassan, D.M., Mukherji, S.K., 2004. Clinical applications of diffusion tensor imaging. J. Magn. Reson. Imaging. 191, 6-18.

Drew, S.C., Silva, P., Crozier, S., Pearcy, M.J., 2004. A diffusion and T2 relaxation MRI study of the ovine lumbar intervertebral disc under compression in vitro. Phys. Med. Biol. 4916, 3585-3592.

Ebara, S., Iatridis, J.C., Setton, L.A., Foster, R.J., Mow, V.C., Weidenbaum, M., 1996. Tensile properties of nondegenerate human lumbar anulus fibrosus. Spine. 214, 452-461.

Fardon DF, Millette PC (Chairpersons), 2001. Nomenclature and Classificationof Lumbar Disc Pathology: Recommendations of the CombinedTask Forces of the North American Spine Society, American Society ofSpine Radiology, and American Society of Neuroradiology.. AJNR. 1.

Fazey, P.J., Song, S., Monsas, S., Johansson, L., Haukalid, T., Price, R.I., Singer, K.P., 2006. An MRI investigation of intervertebral disc deformation in response to torsion. Clin. Biomech. (Bristol, Avon). 215, 538-542.

Ferguson, S.J., Ito, K., Nolte, L.P., 2004. Fluid flow and convective transport of solutes within the intervertebral disc. J. Biomech. 372, 213-221.

Fujita, Y., Duncan, N.A., Lotz, J.C., 1997. Radial tensile properties of the lumbar annulus fibrosus are site and degeneration dependent. J. Orthop. Res. 156, 814-819.

Fullerton, G.D., Cameron, I.L., Ord, V.A., 1985. Orientation of tendons in the magnetic field and its effect on T2 relaxation times. Radiology. 1552, 433-435.

Gatehouse, P.D., Bydder, G.M., 2003. Magnetic resonance imaging of short T2 components in tissue. Clin. Radiol. 581, 1-19.

Goel, V.K., Monroe, B.T., Gilbertson, L.G., Brinckmann, P., 1995. Interlaminar shear stresses and laminae separation in a disc. Finite element analysis of the L3-L4 motion segment subjected to axial compressive loads. Spine. 206, 689-698.

Gu, W.Y., Mao, X.G., Foster, R.J., Weidenbaum, M., Mow, V.C., Rawlins, B.A., 1999. The anisotropic hydraulic permeability of human lumbar anulus fibrosus. Influence of age, degeneration, direction, and water content. Spine. 2423, 2449-2455.

Hashemi, Ray H., M.D., Bradley, W.G.J., Lisanti, Christopher J., M.D., 2003. MRI the basics, second ed. , Lippincott Williams & Wilkins, Philaderlphia USA.

Haughton, V., 2004. Medical imaging of intervertebral disc degeneration: current status of imaging. Spine. 2923, 2751-2756.

Henkelman, R.M., Stanisz, G.J., Graham, S.J., 2001. Magnetization transfer in MRI: a review. NMR Biomed. 142, 57-64.

Hiwatashi, A., Danielson, B., Moritani, T., Bakos, R.S., Rodenhause, T.G., Pilcher, W.H., Westesson, P.L., 2004. Axial loading during MR imaging can influence treatment decision for symptomatic spinal stenosis. AJNR Am. J. Neuroradiol. 252, 170-174.

Holder, C.A., 2000. MR diffusion imaging of the cervical spine. Magn. Reson. Imaging Clin. N. Am. 83, 675-686.

Hsu, E.W., Setton, L.A., 1999. Diffusion tensor microscopy of the intervertebral disc anulus fibrosus. Magn. Reson. Med. 415, 992-999.

Hukins, D.W., 1992. A simple model for the function of proteoglycans and collagen in the response to compression of the intervertebral disc. Proc. Biol. Sci. 2491326, 281-285.

Iatridis, J.C., ap Gwynn, I., 2004. Mechanisms for mechanical damage in the intervertebral disc annulus fibrosus. J. Biomech. 378, 1165-1175.

Iatridis, J.C., Setton, L.A., Weidenbaum, M., Mow, V.C., 1997. The viscoelastic behavior of the non-degenerate human lumbar nucleus pulposus in shear. J. Biomech. 3010, 1005-1013.

Jaermann, T., Pruessmann, K.P., Valavanis, A., Kollias, S., Boesiger, P., 2006. Influence of SENSE on image properties in high-resolution single-shot echo-planar DTI. Magn. Reson. Med. 552, 335-342.

Johannessen, W., Vresilovic, E.J., Wright, A.C., Elliott, D.M., 2004. Intervertebral disc mechanics are restored following cyclic loading and unloaded recovery. Ann. Biomed. Eng. 321, 70-76.

Kakitsubata, Y., Theodorou, D.J., Theodorou, S.J., Trudell, D., Clopton, P.L., Donich, A.S., Lektrakul, N., Resnick, D., 2003. Magnetic resonance discography in cadavers: tears of the annulus fibrosus. Clin. Orthop. Relat. Res. (407)407, 228-240.

Karakida, O., Ueda, H., Ueda, M., Miyasaka, T., 2003. Diurnal T2 value changes in the lumbar intervertebral discs. Clin. Radiol. 585, 389-392.

Kerttula, L., Kurunlahti, M., Jauhiainen, J., Koivula, A., Oikarinen, J., Tervonen, O., 2001. Apparent diffusion coefficients and T2 relaxation time measurements to evaluate disc degeneration. A quantitative MR study of young patients with previous vertebral fracture. Acta Radiol. 426, 585-591.

Kingma, I., van Dieen, J.H., Nicolay, K., Maat, J.J., Weinans, H., 2000. Monitoring water content in deforming intervertebral disc tissue by finite element analysis of MRI data. Magn. Reson. Med. 444, 650-654.

Kraemer, J., Kolditz, D., Gowin, R., 1985. Water and electrolyte content of human intervertebral discs under variable load. Spine. 101, 69-71.

Kusaka, Y., Nakajima, S., Uemura, O., Aoshiba, H., Seo, Y., Hirasawa, Y., 2001. Intradiscal solid phase displacement as a determinant of the centripetal fluid shift in the loaded intervertebral disc. Spine. 269, E174-81.

Larkman, D.J., Nunes, R.G., 2007. Parallel magnetic resonance imaging. Phys. Med. Biol. 527, R15-55.

Le Bihan, D., Poupon, C., Amadon, A., Lethimonnier, F., 2006. Artifacts and pitfalls in diffusion MRI. J. Magn. Reson. Imaging. 243, 478-488.

Lee, K.K., Teo, E.C., 2004. Poroelastic analysis of lumbar spinal stability in combined compression and anterior shear. J. Spinal. Disord. Tech. 175, 429-438.

Lee, S.U., Fredericson, M., Butts, K., Lang, P., 2005. The effect of axial loading and spine position on intervertebral disc hydration: An in vivo pilot study. Journal of Back and Musculoskeletal Rehabilitation. 181-2, 15-20.

Lupo, J.M., Lee, M.C., Han, E.T., Cha, S., Chang, S.M., Berger, M.S., Nelson, S.J., 2006. Feasibility of dynamic susceptibility contrast perfusion MR imaging at 3T using a standard quadrature head coil and eight-channel phased-array coil with and without SENSE reconstruction. J. Magn. Reson. Imaging. 243, 520-529.

Malko, J.A., Hutton, W.C., Fajman, W.A., 1999. An in vivo magnetic resonance imaging study of changes in the volume (and fluid content) of the lumbar intervertebral discs during a simulated diurnal load cycle. Spine. 2410, 1015-1022.

Marchand, F., Ahmed, A.M., 1990. Investigation of the laminate structure of lumbar disc anulus fibrosus. Spine. 155, 402-410.

Markolf, K.L., Morris, J.M., 1974. The structural components of the intervertebral disc. A study of their contributions to the ability of the disc to withstand compressive forces. J. Bone Joint Surg. Am. 564, 675-687.

Martinez, J.B., Oloyede, V.O., Broom, N.D., 1997. Biomechanics of load-bearing of the intervertebral disc: an experimental and finite element model. Med. Eng. Phys. 192, 145-156.

Masuda, K., Aota, Y., Muehleman, C., Imai, Y., Okuma, M., Thonar, E.J., Andersson, G.B., An, H.S., 2005. A novel rabbit model of mild, reproducible disc degeneration by an anulus needle puncture: Correlation between the degree of disc injury and radiological and histological appearances of disc degeneration. Spine. 301, 5-14.

Modic, M.T., Ross, J.S., 1991. Magnetic resonance imaging in the evaluation of low back pain. Orthop. Clin. North Am. 222, 283-301.

Morgan, S., Saifuddin, A., 1999. MRI of the lumbar intervertebral disc. Clin. Radiol. 5411, 703-723.

Munter, F.M., Wasserman, B.A., Wu, H.M., Yousem, D.M., 2002. Serial MR Imaging of Annular Tears in Lumbar Intervertebral Disks. AJNR Am. J. Neuroradiol. 237, 1105-1109.

Natarajan, R.N., Williams, J.R., Andersson, G.B.J., 2003/5. Finite element model of a lumbar spinal motion segment to predict circadian variation in stature. Computers & Structures. 818-11, 835-842.

Newitt, D.C., Majumdar, S., 2005. Reproducibility and dependence on diffusion weighting of line scan diffusion in the lumbar intervertebral discs. J. Magn. Reson. Imaging. 214, 482-488.

Nguyen-minh, C., Riley, L.,3rd, Ho, K.C., Xu, R., An, H., Haughton, V.M., 1997. Effect of degeneration of the intervertebral disk on the process of diffusion. AJNR Am. J. Neuroradiol. 183, 435-442.

Ohshima, H., Tsuji, H., Hirano, N., Ishihara, H., Katoh, Y., Yamada, H., 1989. Water diffusion pathway, swelling pressure, and biomechanical properties of the intervertebral disc during compression load. Spine. 1411, 1234-1244.

Oliphant, D., Frayne, R., Kawchuk, G., 2005. A new method of creating intervertebral disc disruption of various grades. Clin. Biomech. (Bristol, Avon).

Osti, O.L., Fraser, R.D., 1992. MRI and discography of annular tears and intervertebral disc degeneration. A prospective clinical comparison. J. Bone Joint Surg. Br. 743, 431-435.

Pollintine, P., Dolan, P., Tobias, J.H., Adams, M.A., 2004. Intervertebral disc degeneration can lead to "stress-shielding" of the anterior vertebral body: a cause of osteoporotic vertebral fracture? Spine. 297, 774-782.

Rajasekaran, S., Babu, J.N., Arun, R., Armstrong, B.R., Shetty, A.P., Murugan, S., 2004. ISSLS prize winner: A study of diffusion in human lumbar discs: a serial magnetic resonance imaging study documenting the influence of the endplate on diffusion in normal and degenerate discs. Spine. 2923, 2654-2667.

Roberts, N., Hogg, D., Whitehouse, G.H., Dangerfield, P., 1998. Quantitative analysis of diurnal variation in volume and water content of lumbar intervertebral discs. Clin. Anat. 111, 1-8.

Roberts, S., 2002. Disc morphology in health and disease. Biochem. Soc. Trans. 30Pt 6, 864-869.

Roberts, S., Menage, J., Eisenstein, S.M., 1993. The cartilage end-plate and intervertebral disc in scoliosis: calcification and other sequelae. J. Orthop. Res. 115, 747-757.

Roughley, P.J., 2004. Biology of intervertebral disc aging and degeneration: involvement of the extracellular matrix. Spine. 2923, 2691-2699.

Roughley, P.J., Alini, M., Antoniou, J., 2002. The role of proteoglycans in aging, degeneration and repair of the intervertebral disc. Biochem. Soc. Trans. 30Pt 6, 869-874.

Rowley, H.A., Grant, P.E., Roberts, T.P., 1999. Diffusion MR imaging. Theory and applications. Neuroimaging Clin. N. Am. 92, 343-361.

Ruel, L., Brugieres, P., Luciani, A., Breil, S., Mathieu, D., Rahmouni, A., 2004. Comparison of in vitro and in vivo MRI of the spine using parallel imaging. AJR Am. J. Roentgenol. 1823, 749-755.

Saifuddin, A., McSweeney, E., Lehovsky, J., 2003. Development of lumbar high intensity zone on axial loaded magnetic resonance imaging. Spine. 2821, E449-51; discussion E451-2.

Saifuddin, A., Mitchell, R., Taylor, B.A., 1999. Extradural inflammation associated with annular tears: demonstration with gadolinium-enhanced lumbar spine MRI. Eur. Spine J. 81, 34-39.

Setton, L.A., Chen, J., 2006. Mechanobiology of the intervertebral disc and relevance to disc degeneration. J. Bone Joint Surg. Am. 88 Suppl 252-57.

Shellock, F.G., 2000. Radiofrequency energy-induced heating during MR procedures: a review. J. Magn. Reson. Imaging. 121, 30-36.

Skaggs, D.L., Weidenbaum, M., Iatridis, J.C., Ratcliffe, A., Mow, V.C., 1994. Regional variation in tensile properties and biochemical composition of the human lumbar anulus fibrosus. Spine. 1912, 1310-1319.

STEJSKAL, E.O., TANNER, J.E., 1965. Spin Diffusion Measurements - Spin Echoes in Presence of a Time-Dependent Field Gradient. J. Chem. Phys. 421, 288-&.

Thomas, D.L., Lythgoe, M.F., Pell, G.S., Calamante, F., Ordidge, R.J., 2000. The measurement of diffusion and perfusion in biological systems using magnetic resonance imaging. Phys. Med. Biol. 458, R97-138.

Tofts, P.S., 2003. The Diffusion of Water in: Wheeler-Kingshott, C.A.M., Barker, G.J., Steens, S.C.A., van Buchem, Mark A., (Eds),Quantitative MRI of the BrainJohn Wiley and Sons, Chichester, pp. 203-0.

Trudeau, J.D., Dixon, W.T., Hawkins, J., 1995. The effect of inhomogeneous sample susceptibility on measured diffusion anisotropy using NMR imaging. J. Magn. Reson. B. 1081, 22-30.

van der Veen, A.J., Mullender, M., Smit, T.H., Kingma, I., van Dieen, J.H., 2005. Flow-related mechanics of the intervertebral disc: the validity of an in vitro model. Spine. 3018, E534-9.

Van Goethem, J.W., Maes, M., Ozsarlak, O., van den Hauwe, L., Parizel, P.M., 2005. Imaging in spinal trauma. Eur. Radiol. 153, 582-590.

Warach, S., Dashe, J.F., Edelman, R.R., 1996. Clinical outcome in ischemic stroke predicted by early diffusion-weighted and perfusion magnetic resonance imaging: a preliminary analysis. J. Cereb. Blood Flow Metab. 161, 53-59.

Wilke, H.J., Neef, P., Caimi, M., Hoogland, T., Claes, L.E., 1999. New in vivo measurements of pressures in the intervertebral disc in daily life. Spine. 248, 755-762.

Williams, J.R., Natarajan, R.N., Andersson, G.B., 2006. Inclusion of regional poroelastic material properties better predicts biomechanical behavior of lumbar discs subjected to dynamic loading. J. Biomech.

Yu, C.Y., Tsai, K.H., Hu, W.P., Lin, R.M., Song, H.W., Chang, G.L., 2003. Geometric and morphological changes of the intervertebral disc under fatigue testing. Clin. Biomech. (Bristol, Avon). 186, S3-9.

Yu, S.W., Haughton, V.M., Sether, L.A., Wagner, M., 1989. Comparison of MR and diskography in detecting radial tears of the anulus: a postmortem study. AJNR Am. J. Neuroradiol. 105, 1077-1081.

Chapter 3: Research Methods

Overview

This chapter is comprised of three sections. The first section will describe general methods (e.g. specimen procurement) common to almost all experiments in this project. The second section of the chapter will describe early experiments that were conducted in order to develop the final protocol of this thesis research. These early efforts include:

- injury generation techniques (pneumatic, stab and radial cores)
- selection and refinement of imaging sequences
- geometric synchronization of axial MRI sequences
- inclusion of loading protocols within the MRI magnet

The last section of this chapter describes the methods used in the final experiment of this thesis. This concluding experiment compared conventional MRI and DTI images with respect to their ability to detect AF tears during no load and load conditions.

3.1 *General methods:*

Specimen retrieval

Cadaveric sows were obtained from another independent study performed at the Swine Research and Technology Centre, University of Alberta. Spines and peripheral spinal tissues were harvested from these sacrificed sows (n = 21, ~15 months of age, ~200kg) using a reciprocating saw (Sawzall, Milwaukee Tool Ltd., Brookfield WI, USA). Approval for removal of these tissues was provided by the Faculty of Animal Welfare and Policy Committee, protocol number 2005-40B. Following the conclusion of protocol 2005-40, continued access to cadaveric tissue was granted by the Faculty of Animal Welfare and Policy Committee (letter dated 20th June 2006, signed by Doug Korver).

Sample preparation

Some spines, depending on the experiment, were used immediately as freshly harvested tissue. Other spines, depending on the experiment, were frozen at approximately -20 C and thawed for 24hrs prior to use.

Immediately after harvest or following thawing, spine segments were cut down to experimental dimensions with an industrial meat band saw (Torrey Inc, USA). The transverse and spinous processes were removed followed by all surface tissue on the anterior and antero-lateral aspect of the IVDs and vertebrae (Figure 25). The specimens were then wrapped in Saran Wrap (SC Johnson, Racine, Wisconsin, USA) and parafilm (Pechiney Plastic Packaging, Chicago IL, USA) until the time of injury generation. All sample preparation activities were conducted in the Common Spinal Disorders (CSD) Centre.

Figure 25. Lumbar spine segments harvested *en block* from 200kg sow (left), and segment following specimen preparation prior to specimen mounting (right).

Specimen mounting for MRI

In preliminary experiments (section 3.2), prepared specimens were placed supine into various containers and then prior to imaging, immersed in ultrasound contrast gel (USG) (Lithoclear, Sonotech Inc., Bellingham WA, USA). All containers were able to fit within the MRI head coil used in this study. The specimens were always oriented so that the head-end of the spine was oriented towards the far end of the magnet. Later, in the final stages of this project, prepared samples were potted in fixtures for placement in a specially designed loading rig (Figure 26) using dental cement (Labstone, Heraeus Kulzer Inc., Armonk NY, USA). Complete details regarding the loading rig can be found in section *3.2*.

Figure 26. Pots (arrows) fixed to spine segment in loading rig fixtures. Image is from final experiment.

Imaging hardware

Imaging of the prepared specimens occurred at the *In Vivo* Nuclear Magnetic Resonance (NMR) Centre. All experiments were conducted using an 8-channel head coil in the Magnetom Sonata 1.5T MRI unit (Siemens, Erlangen, Germany). Imaging of the freshly harvested tissue would commence approximately 4 hours following euthanasia. An MRI technician assisted during the imaging phase of the preliminary experiments.

Tissue storage

Once the MRI protocol had been completed, specimens were removed from the magnet, and returned to the CSD centre. A syringe and needle were then used to inject aqueous Toluene Blue dye into the injury before re-freezing. Refreezing occurred at approximately -20°C.

Anatomical sections for dye enhanced visualization

To confirm MRI observation of injury, the post-experiment frozen IVDs were transected. For photography of these transections, the specimen identification and IVD level were displayed prominently beside the tissue sample and the macroscopic mode of a digital camera (Nikon CP L3, 5.1mpixels, Nikon Corp., Japan) used (Figure 27). The IVDs were sectioned from the inferior to superior endplates (~1cm at outer AF) until the injury, assumed to be the dye-enhanced region, was reached. Because the tissue would warm over time, specimens were returned to the freezer often to maintain rigidity during sectioning.

Figure 27. Anatomical section showing injuries from final experiment.

Tissue disposal

At each preparation step, the approved procedure for disposal of waste (garbage bags, USG, and biological material) was followed.

3.2 *Preliminary Experimentation:*

This section will describe early experiments that were conducted in order to optimize the methods used in the final experiment of this project. As noted in the chapter overview, these early experiments investigated:

- injury generation techniques (pneumatic, stab and radial cores)
- selection and refinement of imaging sequences
- geometric synchronization of axial MRI sequences
- inclusion of loading protocols within the MRI magnet

3.2.1 Pneumatic injury and preliminary selection of imaging sequences:

The goal of this experiment was to determine if injuries of a predictable size could be generated inside of the AF, and then visualized with DTI. The hypothesis of this work was that the resulting tears in the AF, which did not contain any nuclear material, would be visible to DTI maps while invisible to conventional MRI techniques.

Injury generation and imaging protocol

To establish injury in the AF, the method outlined by Oliphant *et al.* was implemented (Oliphant, Frayne, & Kawchuk, 2005). Specifically, a 20GA 1.16IN BD Insyte-W (Becton Dickson, Oakville, ON, Canada) catheter was inserted through the anterior IVD tissue, with the needlepoint coming to rest in the antero-lateral aspect of the AF for each of a specimen's IVDs. Once in position, the needle was removed leaving the catheter in place. The catheter was then connected to the pressure regulator of a compressed nitrogen gas tank (Praxair Inc., Danbury CT, USA) via polyethylene tubing (Cook Canada, Stouffville, ON, Canada) and leur locks. Using the pressure regulator, the compressed gas was ramped to a final pressure of 1000kPa for a duration of 1-minute period. This pressure was maintained for an additional minute and then the catheter was disengaged from the compressed gas tank and removed from the IVD. Once the presumed injury was created in this manner, the specimen was placed into a container with USG as described in section 3.1 and then placed inside the 1.5T MRI unit.

Localizer scans (T1W) were then obtained for slice selection and FOV placement, followed by the imaging protocol outlined in Table 2. To reduce the attenuation of signal from the AF and AF injuries during the DTI sequence (Kealey et al., 2005) a b value of 400 s/mm^2 was utilized.

	Imaging sequences						
Imaging details	HiRes AxT2	AxT1	SagT1	CorT1	AxT2 Measure	SagT2	DTI-mSense IPat (R = 2) b = 400 s/mm^2
TR (msec)	97	46	16	16	1863	109	3
FOV (mm)	180x180	185x185	200x200	180x180	180x185	256x256	128x256
Slice (#)	20	20	15	15	15	15	20
Acquired matrix	512x512	256x256	256x256	256x256	192x192	256x256	96x128

Table 2. Experiment 1 imaging protocol.

Visualization of MRI images

Following imaging, all data were transferred from the MRI unit's workstation to a workstation in the CSD centre. MRVision (MRVision Co, USA) was then used to visualize both the conventional and DTI MRI images.

Slices generated by the conventional MRI sequences could be viewed without any post-processing, but the DTI maps had to be generated using MRVision to process the data captured in the DTI sequence. The raw b0 and 6 diffusion-weighted images (DWI) acquired for one slice in a DTI sequence can be seen in Appendix D. A custom script, tensor6drns.m (created by Yusuf Bhagat), was used to generate preliminary sets of DTI slices. From these initial DTI images, slices that showed promising injury visualization were noted, and the raw DWIs corresponding to these slices were then used to generate DTI maps optimized for injury visualization by the procedure described in the following paragraphs.

Optimization of DTI maps

A signal intensity (SI) profile was plotted across the axial body of the IVD in the b0 scan (no diffusion weighting) (Figure 28) using the '*line mode*' region of interest (ROI) option in the MRVision ROI-Measurements tool. The general SI in the injury location (position 'C', Figure 28) was identified and then a slightly lower number (position 'B', Figure 28) was selected as the SI threshold level. This threshold level was then put in the 'Noise threshold' field of the '*ADC Apparent Diffusion Coefficient Mapping*' function in the MRVision Image Fitting tool. Executing this function then produced 6 threshold ADC maps from the raw DWI images (Figure 29). Each ADC map represented diffusion weighting in a different gradient direction. The '*Diffusion Tensor Mapping*' function was then used to produce the final threshold DTI maps from these 6 threshold ADC maps. Depending on the visual results of the threshold DTI maps, a higher or lower SI threshold value was selected, and the process was repeated until the DTI maps were optimized for injury visualization.

Figure 28. Screen shot of the injured IVD slice (b0) and MRVision's ROI measurement tool generating an SI profile from placement of the 'line ROI' across the anterior AF. Positions A, B, C reflect USG, AF, and AF injury SI along the line ROI. Image is from final experiment.

Figure 29. Screen shot of b0 and 6 DWIs from the same slice prior to being fitted to threshold ADC maps using MRVision's Image fitting tool. Image is from final experiment.

Following DTI map optimization, data from anatomical sections were required to corroborate positive MRI injury visualization. This ensured that MRI observations could be supported by visual evidence. The methodology used to generate anatomical observations is described in section 3.1.

Results

In this experiment, anatomical sections confirmed 2 successful pneumatic injury generations out of 6 attempts, and neither of these injuries was visualized by any of the MRI sequences. Therefore the hypothesis that small injuries lacking nuclear material would be visible to DTI maps while invisible to conventional MRI sequences could not be supported.

Of the four unsuccessful injuries, two were visualized by both DTI and conventional MRI. This was due to these injuries being concentrated in the NP (Figure 28). Of the remaining two injury attempts only catheter tracks toward the intended injury sites were visible on the anatomical sections. These AF regions could have been stronger than the usual injury sites resulting in no injury being formed. The dye for anatomical visualization could have also not been injected at a sufficient pressure so that the injury boundaries were demarcated for visual observation.

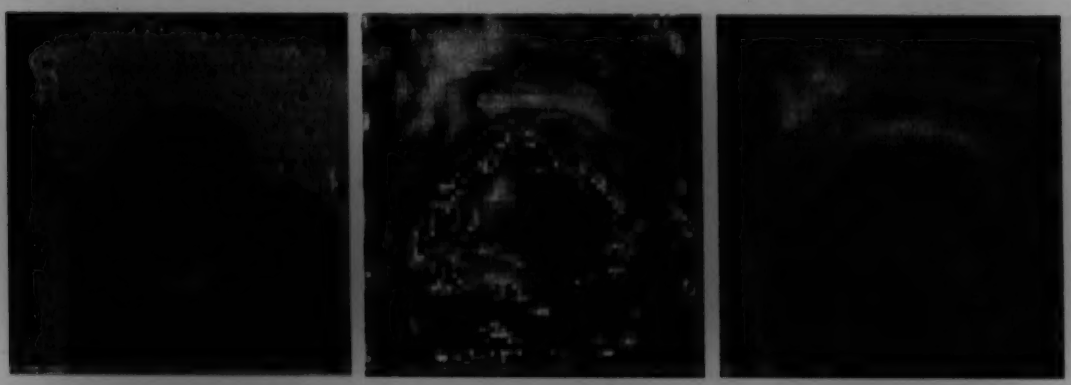

Figure 30. Axial HiResAxT2, and DTI (FA and TraceADC) maps of pneumatic injury where catheter tip came to rest in NP versus the AF.

Discussion

Of the injuries that were successfully generated, the lack of DTI visualization was most likely due to these injuries not immediately filling with inter-cellular fluid. If fluid did manage to migrate into the injury boundaries, the levels may have been below the minimum requirements for DTI visualization. In addition, it was realized that the direct comparison of MRI sequences for injury detection was also problematic as few of the axial sequences had slices at the same physical location.

In summary, the pneumatic injury protocol used in this experiment was not appropriate for further use in this project, and more detailed MRI slice parameters were required. As a result, a different method of injury generation and improvements in injury visualization were sought.

3.2.2 Stab injury, continued selection and refinement of imaging protocol:

The results from the previous experiment indicated that the pneumatic injury, though well characterized by the author in an earlier study, was too small and variable to act as a consistent standard injury for conventional MRI and DTI sequence comparisons. Also, it was discovered that there was a need to synchronize injury slices in order to accurately compare conventional MRI and DTI injury visualization.

Given the above, the first goal of this experiment was to generate a simple injury that would communicate with the NP, in order to best encourage MRI visualization. To accomplish this, a puncture needle was used to induce radial tears in the AF. The second goal of this experiment was to synchronize the axial MRI sequences. To achieve this, sequences were adjusted so that the geometric parameters were closer to that of the DTI sequence. Sequence parameters were also adjusted to improve IVD visualization.

Injury generation and imaging protocol

A 12GA 65mm Puncture Needle (MRI Devices Daum GmBH, Waukesha, WI, USA) was inserted through the anterior-lateral IVD tissue, with the needlepoint exiting through the posterior-lateral aspect on the opposite side of the IVD. Once in position, the needle was removed slowly. The specimen was placed into a container with USG as described in section 3,1 and then placed inside the 1.5T MRI unit. Localizer scans (T1W) were used for slice selection and FOV placement followed by the imaging protocol outlined in Table 3. Independent slice groups were used for each IVD versus the serial slice scanning done in the previous experiment.

	Imaging sequences						
Imaging details	HiRes AxT2	AxT1	SagT1	CorT1	AxT2 Measure	SagT2	DTI-mSense IPat (R = 2) b = 400 s/mm^2

Table 3. Experiment 2 imaging protocol.

MRI injury visualization

The method of injury visualization was identical to the procedure used in the previous experiment.

Results

The injury protocol in this experiment was successfully implemented in all 4 of the specimen IVDs. DTI sequence visualization of the AF injury reached 75%, whereas conventional MRI imaging was unable to visualize the injury (Figure 31). Both imaging techniques were able to visualize the injury in the NP (DTI detection was 75% and conventional MRI detection was 50%) (Figure 31). The low TE intervals of the AxT2Measure sequence also managed to reach 75% AF injury visualization. Also, unlike the previous experiment, each sequence generated slices at the same position, and these slices provided full coverage of the specimen IVDs.

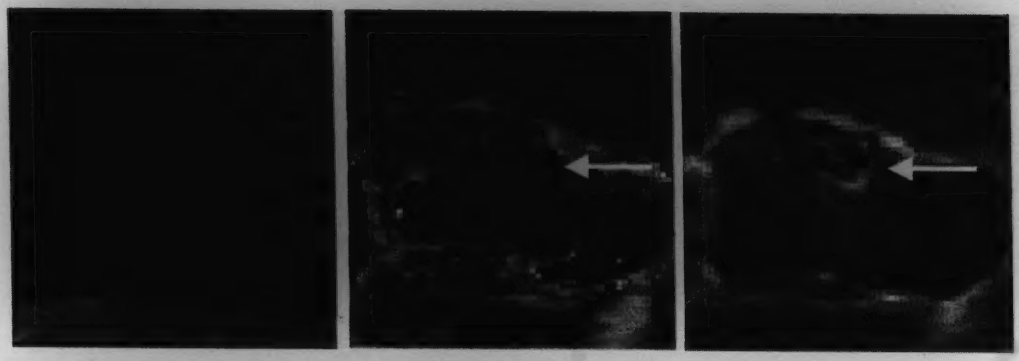

Figure 31. Axial HiResAxT2, and optimized (Threshold at 52SI) DTI (FA and TraceADC) maps of stab injury (white arrow) where injury propagates diagonally through AF and NP.

Discussion

A simple puncture needle stab created an injury that propagated through the AF and into the NP. This allowed for nuclear material to migrate into the injury space, providing a strong signal source for MRI visualization. While the imaging parameters for each sequence were improved regarding slice position, synchronization of slice plane and FOV was still not achieved.

3.2.3 Radial cores with MRI sequence refinement, synchronization, and inclusion of loading protocol

The results from the previous experiment indicated that the 12GA stab wound generated a consistent and reproducible injury, however, the exact boundaries and location of the injury were unknown once the needle was removed. The presence of only one injury also made it difficult to comment on the threshold of injury visualization for DTI maps since only 1 size of injury was generated. The imaging protocol that was used also had many sequences that were not extensively utilized which unnecessarily increased the overall imaging time. It was also shown that the geometric parameters for some sequences could not be adapted to others due to sequence limitations. This resulted in FOV varying between some sequences.

Given the above, the primary goal of this experiment was to establish an injury protocol that would allow for a threshold of injury visualization to be determined for both conventional MRI and DTI. This was to be accomplished by using known diameter drill bits to generate radial cores in the AF. The secondary goal of this experiment was to select a reduced set of MRI sequences, to efficiently use imaging time and to achieve geometric synchronization between all the axial MRI sequences. To ensure that the synchronized slice planes fell over the injury, spectroscopy glass plugs filled with saline were used as internal markers. Finally, dynamic loading was incorporated into this experiment as the experimental methodology was approaching its final form.

Modification of existing loading rig

In order to create dynamic loading of the IVD in the MRI unit, modification of an existing MRI-compatible compression rig had to first be completed. The original rig (Figure 32) was designed to provide compressive loads in a MRI body coil, therefore, specific modifications had to be made so that the compression rig would fit within the 8-channel head coil used in this study (Figure 32).

Figure 32. MRI safe rig used by Oliphant et al. (Oliphant, Frayne, & Kawchuk, 2005) (left), and 8-channel head coil (right).

The original rig used a pneumatic cylinder driven by compressed air to advance the back piece, or ram, of the two-piece rig along two lengths of wood dowel. The top piece of the compression rig was connected to a fine adjustment platform that adjusted the top piece's location along the dowel runners. The dowel runners were anchored to the adjustment platform and the pneumatic cylinder. A load cell (SSM-AJ-500, Interface Inc., Scottsdale Arizona, USA) arranged in series with the pneumatic cylinder and ram, was used to calibrate the compressed gas pressure used to drive the rig to the desired compressive load.

The primary difference between the body and head coil was the length of the imaging volume. To place as much of the specimen into the coil as possible, all unnecessary length was removed from the loading rig. The dowel was anchored to the top piece of the loading rig, and the fine adjustment platform was removed in addition to anything extending behind the top piece of the rig. A portion of the top piece of the rig was also removed, leaving only enough thickness to withstand loads of approximately 2000N. With all the length adjustments, approximately 12cm of specimen could fit into the head coil's imaging volume. This effectively translated into 3 IVDs.

Originally the loading rig sat on 4 adjustable pylons to best position the sample in the body coil. Unlike the body coil, the head coil was closed at the top, and had a contoured base that acted as a basin for a patient's head. Because the top two pylons were attached to the fine adjustment platform, they had already been removed. An alternate means of supporting the top half of the rig was achieved by removing material just below the dowel runners,. This created a lip that allowed the top half of the loading rig to rest on the coil's head basin (Figure 33). The ram remained outside of the coil, and the back height adjustment pylons were positioned so that the loading rig sat level in the head coil. These modifications positioned the sample in the middle of the head coil's imaging volume.

Figure 33. The modified loading rig.

Compression rig calibration

Due to the imaging artifacts generated when using the load cell in the MRI environment, it could not be directly incorporated into the dynamic MRI load measurements. Therefore, a digital pressure sensor (Festo Inc., Mississauga ON, Canada) connected to the compressed gas source was calibrated to the load cell prior to imaging.

To calibrate the digital pressure sensor, a length (approximately 25cm) of polyvinyl chloride tubing was placed into the compression rig. The rig was then driven at a series of pressures at regular intervals. A LabView (National Instruments Corp., Austin TX, USA) data acquisition program (developed by Greg N. Kawchuk) was used to capture the corresponding voltage readings from the load cell on a laptop. The calibration curve was generated (Figure 34), and the voltage to load relationship (2222N / 10V) was then used to determine the required step pressure from the compressed gas tank. With the modified compression rig and a calibrated pressure sensor, a variation to the loading protocol outlined by Chiu *et al.* (Chiu et al., 2001) was used to generate step loads of 830N during MRI.

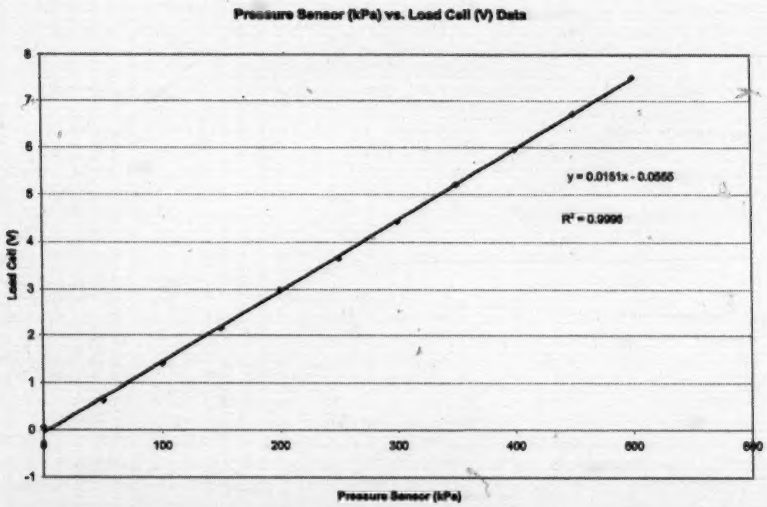

Figure 34. Pressure sensor and load cell calibration curve from final experiment, with curve equation (y) and coefficient of determination (R^2).

Injury generation and imaging protocol

The specimens in this experiment were prepared immediately following tissue harvest, and were potted in fixtures for placement in the modified loading rig as outlined in section 3.1. A wooden spine was affixed to the anterior portion of the specimen by screws in the top and bottom vertebral bodies (Figure 35). On this wooden spine, lines were drawn with a pencil corresponding to the axial plane of each IVD. Then the entire wooden spine was removed from the specimen. A drill press (Delta International Machinery Inc., Guelph ON, Canada) drilled holes of 5mm (or 4mm), and 2mm diameters into the wooden spine along the traced axial planes, with the largest holes positioned at the centre of each plane. The wooden spine was reattached to the specimen. Then the drill press was used to take 5mm (or 4mm), and 2mm diameter cores from the anterior AF using the holes that were drilled earlier into the wooden spine as guides. The 5mm (or 4mm) core was the first injury, followed by the 2mm cores. Each specific core injury was made at each IVD level before the next core size was drilled. The drill was limited to a core depth of approximately 1cm. Each core was at least 5mm from the adjacent core.

Once a tissue core was taken, saline filled spectroscopy glass (5, 4, and 2mm O.D. NMR tubes, Chemglass, Vineland USA) plugs of corresponding outer diameters were inserted through the guides of the wooden spine into the AF injury (Figure 35). The plugs were made by cutting the spectroscopy glass to ~4mm lengths. Using an oxygen torch, one end of each tube was sealed. Once cooled, the sealed end was sanded down to a conical shape, and a small gauge needle and syringe was used to fill the glass body with saline and displace any air bubbles. Once filled with saline, epoxy was used to seal the open end of the plugs. Complete sets of plugs were made prior to the experiment. Following insertion of the glass plugs into the appropriate injuries, the wooden spine was removed.

Figure 35. Wooden spine attached to specimen, with glass plugs in guides. The three different plug sizes are displayed on top of wooden spine.

MRI Protocol: No Load

Following injury, the specimen was placed into the loading rig and covered with USG, and then placed inside the 1.5T MRI unit. Localizer scans (T1W) were used for slice selection and FOV placement was based on visualization of the saline plugs. Immediately following localizers, an Axial T1W scan was used to confirm axial slice

position over the glass plugs. If successful, the MRI bed was partially brought out of the MRI bore, and the glass plugs were manually removed from the specimen. If not successful, new sets of localizers were taken to determine slice placement. When a successful slice plane was achieved, the imaging protocol was conducted as shown in Table 4. Like the previous experiment, independent slice groups were used for each IVD.

Imaging details	Imaging sequences			
	HiRes AxT2	AxT1	SagT2	DTI-mSense IPat (R = 2) b = 400 s/mm^2
[redacted]				

Table 4. Experiment 3 imaging protocol.

MRI Protocol: Load

Prior to initiating the compressive load, the glass plugs were reintroduced into the IVD core injuries. Then using the regulator on the compressed gas tank, the pressure driving the compression rig was ramped up to the final calibrated level required to reach 830N. This was done over a 1-minute period. To ensure a step load, the compressed gas pressure was constantly monitored. Any pressure fluctuations generally stabilized after approximately 3 minutes. After 3 minutes, T1W localization and axial T1W confirmation of slice position was repeated until the injury plane was visualized. The patient bed was then partially backed out of the MRI bore, and the glass plugs were removed. The imaging protocol from Table 4 was then repeated.

MRI injury visualization

Please consult the first preliminary experiment.

Results

Of the 6 IVD injured in this experiment, the larger 5mm (or 4mm) core injuries were consistently visualized by conventional MRI (100%) and DTI (100%), but for the 2mm injury conventional MRI visualization (50%) was less than the DTI visualization (67%) (Figure 36). Each sequence in the imaging protocol had the same injury slice plane as well as the same FOV. Finally, dynamic loading was successfully introduced into the experiment although a number of the glass plugs cracked during the loading protocol.

Figure 36. Axial HiResAxT2, and optimized (Threshold at 80SI) DTI (FA and TraceADC) maps of 5mm (centre left) and 2mm (centre right) core injuries. Injury propagates anterior-posterior through AF and NP. Drill press drilled further than called for in experimental protocol for 5mm core injury.

Discussion

A range of injury visualization was achieved for both conventional MRI and DTI sequences. The core injury, like the stab, enabled nuclear material to migrate into the injury space, providing a strong signal source for MRI visualization. The imaging parameters for each sequence were synchronized in terms of slice plane and FOV, however, the size of the FOV made it difficult to visualize anatomical features on all of the sequences. Finally, dynamic loading was incorporated into the experimental protocol, though using rigid internal markers created difficulties when time for their removal under load conditions. Also, on the occasion that the markers would break, glass could be left inside the injury boundaries, affecting MRI injury visualization.

3.3 *Final thesis study: conventional MRI versus DTI injury visualization of 2mm core and 12GA stab injuries, without and with dynamic loading*

The final experiment in this study was designed to use a known diameter drill bit to generate cores in the AF in addition to radial tears induced by a puncture needle. These injuries where then imaged by conventional MRI and DTI sequences. This approach resulted in a range of injuries for potential visualization without the injuries obscuring each other. Conventional MRI sequences were geometrically synchronized to that of the DTI sequence - all axial slices shared a common slice plane. The specimens were also imaged under no load and load conditions. To ensure that the same slice planes were imaged under both load conditions, wooden beads served as external markers at each injury location to avoid difficulties in removing internal markers.

Injury generation and imaging protocol

The specimens in this experiment were prepared immediately following tissue harvest and were potted in fixtures for placement in the modified loading rig as outlined in section 3.1. Following spinal mounting, the specimens underwent injury generation, which can be seen in Figure 37.

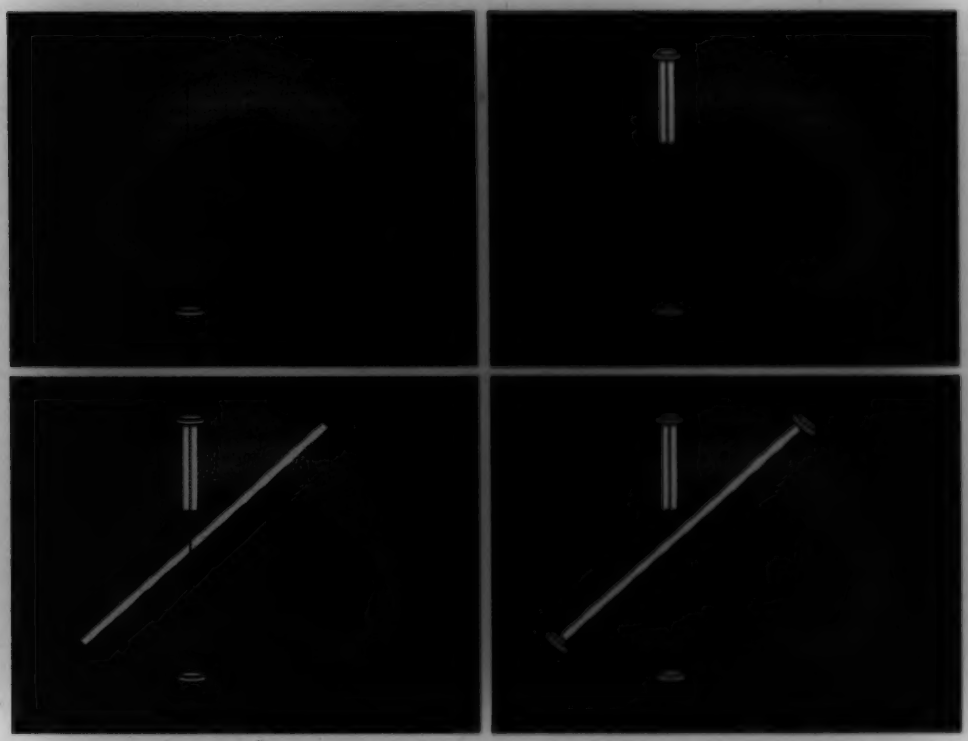

Figure 37. Cross-section of IVD showing progressive schematic of injury protocol. The top two panels describe 2mm core injury generation, and the bottom two panels relate to the 12GA stab injury protocol. The position of the two injuries alternated between adjacent IVDs. A) Small gauge needle advances through the IVD. B) Bead is advanced over the protruding needle and glued to the posterior IVD tissue. C) 2mm core from the AF is taken. D) Second bead is glued above injury site. E) 12GA puncture needle is inserted diagonally through the IVD. F) Beads are glued to the entrance and exit wounds of the stab injury. Background IVD image from Adams *et al.* (2005) (Adams and Dolan, 2005).

A small gauge needle was advanced through the IVD tissue using the drill press, prior to the generation of the core injury. Once protruding through the posterior IVD, a felt marker painted the exit and entrance wounds of the IVD. A small cylindrical bead (varying I.D./O.D., wood or plastic) was then advanced over the protruding needle and glued to the posterior IVD tissue. When the bead was firmly affixed to the IVD tissue, the needle was slowly retracted. Without moving the sample, the 2mm drill bit replaced the needle, and then a 2mm core injury was made in the anterior AF. The pointed end of

a skewer was then placed into the 2mm core injury to guide a pre-glued bead to the injury entrance. The 2mm core injuries were generated slightly lateral to the anterior peak of the IVD. This procedure was conducted on the two middle IVDs of a specimen. The 2mm core of the lower IVD was positioned right of centre, and the 2mm core of the superior IVD was taken left of centre. A 5mm core was then taken from the most caudal IVD for temperature measurements.

Upon completion of the core injuries, the 12GA stab injury protocol from the second preliminary experiment was used. The stab injuries were generated on the anterior-lateral side opposite to the location of the core injury, but within the same injury plane (Figure 37). Then like the core injury, beads were glued to the entrance and exit wounds of the stab injury with a skewer. Following generation of this injury, the two middle IVDs for each specimen had both a 2mm core and 12GA stab injury (Figure 37). With the completion of the injury protocol, the open portion of the anterior beads was covered with parafilm to ensure that USG did not enter the injury space.

MRI Protocol: No Load

Following injury, the specimen was placed into the loading rig, covered with USG, and then placed inside the 1.5T MRI unit. Localizing (T1W) sequences were performed followed by a High Resolution coronal T2W scan to identify bead locations via signal voids surrounding high intensity centre of beads. Axial localizers (T1W) for injury slice selection were then run to place the imaging slices on the anterior and posterior bead identified from coronal scans. Axial visualization of beads confirmed injury plane visualization, and if not successful, new sets of axial localizers were taken until the injury plane was visualized. Following successful injury plane visualization, the imaging protocol was conducted on the 1.5T MRI unit as shown in Table 5. Independent slice groups were used for each IVD.

Imaging details	Imaging sequences: DTI-mSense IPat (R = 2)_ b = 400 s/mm^2	AxT2 Measure	HiRes AxT2	Clinical AxT2_ Turbo SE	Clinical SagT2_ Turbo SE
[redacted]					

Table 5. Final experiment imaging protocol, beginning with DTI-mSense IPat sequence.

MRI Protocol: Load

Following imaging in the no load condition, the MRI bed was brought out of the magnet for access to the specimen and loading rig. Temperature measurements were taken and the position of the back piece of the loading rig was marked on the dowel runner with a pencil. The MRI bed was retracted back into the MRI bore and the dynamic loading protocol from the previous experiment was run. The imaging protocol from Table 5 was then repeated. Following the MRI protocol under load, the specimen temperature was taken and the position of the back piece of the loading rig was marked on the dowel with a pencil.

Qualitative injury visualization analysis

Please consult the first preliminary experiment dealing with pneumatic injury generation and initial imaging protocol. The same injury visualization procedure described there is repeated in this final experiment for both the 2mm core and 12GA stab injuries.

As MRI injury visualization was not always limited to one slice per IVD, two MRI slices were often noted as capable of injury visualization. Although the injury could be visualized by 2 slices, only one slice was aligned to the injury plane as described in the methods. The second, non-aligned slice, came either immediately before or immediately after the aligned slice in the set of serial slices. To differentiate between the two, the slice that covered the actual injury plane is referred to as the "on" slice and the slice adjacent to the injury plane is referred to as the "off" slice. Because there are two slices where injury visualization can occur per IVD, the DTI injury visualization procedure was repeated for the 2mm core and 12GA stab injuries on both the "on" and "off" slices (Appendix D).

Injury detection was determined by the author and a radiologist. A basic tally system was used to score axial injury visualization for each set of sequences categorized as Clinical (clinical ax_T2_tse and hiresT2), Proton Density (AxT2Measure) and DTI (TraceADC, eigenvalue maps 1 – 3, FA) sequences. If injury visualization was achieved, a score of '1' was given. Alternatively, failure to achieve injury visualization resulted in a score of '0'. If consensus was not reached, agreement between the two raters was to occur through discussion.

Using the statistical software package, statistiXL (statistiXL, Broadway-Nedlands, AU) a Wilcoxon Paired-Sample test was used to determine if there was significant difference between the number of DTI injury visualizations, and the number of injury visualizations from the other axial sequences ($\alpha = 0.05$). This analysis was conducted separately as well as combined for the 'on' and 'off' slice planes, in the no load and load data sets of both the 2mm core and 12 GA stab injuries. The Wilcoxon non-parametric test is used to assess the probability of observation from one population exceeding the observations from a second population (statistiXL, non-Parametric tests). Preliminary tests indicated that DTI had higher injury detection rates, so this test was set as a single-tail probability.

Quantitative injury visualization analysis

Boundaries were traced around the 2mm core and 12GA stab injury sites of the SI thresholded DTI maps (Figure 38), as well as the NP, using the '*polygon mode*' in the MRVision ROI-Measurements toolbox. With these ROIs, the DTI (TraceADC, mean diffusivity along principal eigenvalue directions, Fractional Anisotropy) and DWI (SI) values for the injuries and NP were collected for each injured IVD. To calculate CNR between the injuries and NP, additional ROIs were generated for the area outside of the specimen volume, but not in the phase encode direction. From these ROIs standard deviation of the noise SI components in each scan were collected. The CNRs were then calculated by subtracting the SI of the NP from the SI of the injury, and then dividing the result by the noise standard deviation values.

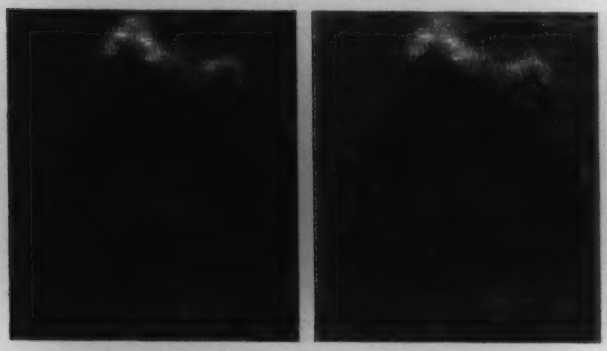

Figure 38. Thesholded (64 SI) TraceADC map (left), with 2mm core injury ROI boundary (right).

Descriptive statistics (mean, standard deviation) were constructed for all DTI data (2mm core, 12GA stab, NP, CNR) in both unloaded, and loaded compressive states. Finally, a 2 x 5 (Injury Slice Plane by ROI) fixed effects multivariate analysis of variance (MANOVA) was used (statistiXL) to determine if any of the average DTI data (TraceADC, eigenvalues 1-3, Fractional Anisotropy) from the 2mm core or 12GA stab injury ROIs were significantly different than the corresponding DTI measure from the NP ($\alpha = 0.05$). A MANOVA is employed when multiple dependent variables exist that cannot be combined, but are potentially affected by changes in an independent variable(s) (statistiXL, General linear model). This analysis was done under both no load, and load conditions.

Chapter 3 references

Adams, M.A., Dolan, P., 2005. Spine biomechanics. J. Biomech. 3810, 1972-1983.

Chiu, E.J., Newitt, D.C., Segal, M.R., Hu, S.S., Lotz, J.C., Majumdar, S., 2001. Magnetic resonance imaging measurement of relaxation and water diffusion in the human lumbar intervertebral disc under compression in vitro. Spine. 2619, E437-44.

Kealey, S.M., Aho, T., Delong, D., Barboriak, D.P., Provenzale, J.M., Eastwood, J.D., 2005. Assessment of apparent diffusion coefficient in normal and degenerated intervertebral lumbar disks: initial experience. Radiology. 2352, 569-574.

Oliphant, D., Frayne, R., Kawchuk, G., 2005. A new method of creating intervertebral disc disruption of various grades. Clin. Biomech. (Bristol, Avon).

Chapter 4: Results

Overview

In Chapter 3, the results of several *early* experiments were presented as these investigations were used to construct the methodology of the final experiment. It is for this reason that only the results from the final experiment will be presented in this chapter. These results will be separated into three sections.

The first section will describe the specimens used in the study.

The second section will report qualitative injury results. In brief, these results demonstrated that injuries were visualized significantly more often in DTI scans than in clinical scans for both the 2mm core and 12GA stab injuries. The qualitative data also showed that dynamic loading of the specimen improved detection of the 2mm core injury in both DTI and clinical sequences.

In the third section of this chapter, the quantitative results will be reported. These results indicate that DTI measures of both injuries were found to be significantly different from those associated with the NP, but not from each other. Dynamic loading did not change this, as DTI measures from the injuries continued to be significantly different from the NP DTI data.

4.1 Study specimens:

A total of 6 lumbar spines were utilized in the final experiment. From these 6 spines, injuries were generated in 14 IVDs then imaged. The use of convenience sampling limited the retrieval of fresh IVDs to this final number. As a result, it was felt that 14 IVDs would provide an adequate opportunity for trends in the data to be observed. Of the 14 IVDs scanned, 3 had to be excluded from the study because of inadequate visualization, which was defined as images having high noise content that resulted in poor contrast between AF, NP and USG, and/or artifacts that obscured visualization of general anatomy. The 3 excluded IVDs were positioned either at the top or bottom of the loading rig. Given this proximity to the rig's terminal ends, as well as being positioned on the periphery of the imaging volume, susceptibility effects and reduced coil sensitivity about these IVDs were most likely the cause of the inadequate visualization.

A total of 22 image slices per load condition were collected. For each IVD, a pair of images was available for injury visualization (Appendix D). One image of the pair was considered to be optimally aligned to the induced injury (the "on" slice) while a second slice fell adjacent to the injury slice plane (the "off" slice).

Finally, the temperature measurements of the most caudal IVD indicated an average IVD temperature of approximately 22°C during the imaging protocol. This is an important variable to record as diffusion is temperature dependent.

4.2 Qualitative injury visualization analysis:

The percentage of visualization for the 2mm core injuries was greater for each MRI category than for the 12GA stab injuries (Table 6). The percentage of DTI visualization was significantly greater than the other two sequence categories for both the 2mm core and 12GA stab injuries. In most cases, dynamic loading conditions increased the percentage of detected injuries (Table 6), however, these increases were not always

statistically significant. The complete set of IVD scans for both the 2mm core and 12GA stab ("on" slices) can be viewed in Appendix F.

No Load	Clinical sequences	Proton Density sequence	DTI maps
2mm core injury	9/22 (41%) *	11/22 (50%) *	19/22 (86%)
12GA stab injury	2/22 (9%) *	4/22 (18%) *	16/22 (73%)
Load			
2mm core injury	15/22 (68%) *, **	11/22 (50%) *	21/22 (96%)
12GA stab injury	3/22 (14%) *	4/22 (18%) *	12/22 (55%)

Table 6. Combined "on" and "off" slice injury visualization for each MRI category. A single * denotes injury observation significantly less than DTI sequences for a given injury and load condition. A double ** denotes a significant increase in injury observation with dynamic loading for an individual MRI category. Significance is at the $p < 0.05$ level.

Qualitative results

For visualization of the 2mm core injury using only "on" slices (Figure 39), both the proton density and DTI maps achieved higher injury observation (91%) than the clinical MRI sequences (55%) (Table 7). Interestingly, the large increase in injury visualization using DTI was not found to be statistically greater than either the clinical or proton density sequences ($p = 0.063$ and 1.00 respectively, Wilcoxon Paired-sample test).

For the "off" slices, DTI visualization of the 2mm core (82%) was statistically greater than both clinical (27%) and proton density (9%) sequences ($p = 0.016$ and 0.004 respectively, Wilcoxon Paired-sample test).

Considering the combined "on" and "off" scores, or the use of 2 serial scans for injury observation, DTI observation (86%) was significantly more sensitive to the 2mm core injury than clinical sequences (41%) ($p = 0.001$, Wilcoxon Paired-sample test). Overall, the proton density sequence achieved visualization levels of 50% for 2mm core injuries, which was significantly fewer injury observations than the DTI sequence ($p = 0.01$, Wilcoxon Paired-sample test).

Clin.AxT2 HiResAx T2 Proton Density TraceADC Eigenvalue 1 Eigenvalue 2 Eigenvalue 3 FA

(a) (b) (c)

Figure 39. Final experiment's axial imaging protocol, "on" slice. 2mm core injury left of centre, and 12GA stab right of centre. Clinical (a) and proton density (b) sequences, and DTI maps (c) were scored as having positive 2mm core injury visualization (left arrow). Only DTI maps (c) were scored as having positive 12GA visualization (right arrow).

2mm core injury	# FOEs	Clinical	Proton Density	DTI
on slice	11	6 (55%)	10 (91%)	10 (91%)
off slice	11	3 (27%) *	1 (8%) *	9 (82%)
combined	22	9 (41%) *	11 (50%) *	19 (86%)

Table 7. Visual observation of the 2mm core injury with axial MRI scans (clinical, proton density and DTI). Each row of the table corresponds to a common MRI slice shared by each of the axial MRI sequences. Absolute number and percentage of successful injury observations are reported for each MRI category. A single * denotes injury observation significantly less than DTI sequences for a given slice plane. Significance is at the $p < 0.05$ level.

Similarly, the 12GA stab was preferentially visualized using the "on" slice with DTI maps (73%) compared to the proton density (36%) and clinical sequences (9%) (Table 8). Unlike the 2mm core visualization using the "on" injury plane, DTI visualization of the 12GA stab was significantly higher than the clinical sequences ($p = 0.008$, Wilcoxon Paired-sample test), but it was still not found to be significantly larger than the proton density sequence ($p = 0.109$, Wilcoxon Paired-sample test).

For the "off" slices, both DTI and clinical sequences had the same score as in the "on" slices (73% and 9%), while the proton density sequence (0%) failed to generate any slices adjacent to the injury plane. Therefore, DTI injury visualization remained significantly larger than the clinical sequences ($p = 0.008$, Wilcoxon Paired-sample test), but was also significantly larger than proton density injury visualization for the "off" slices ($p = 0.004$, Wilcoxon Paired-sample test).

Considering the combined "on" and "off" scores, or the use of 2 serial scans for injury observation, DTI map injury observation (73%) was significantly higher than clinical (9%) and proton density (18%) sequences for 12GA stab injury observation ($p = 0.000$ and 0.001 respectively, Wilcoxon Paired-sample test).

12GA stab injury	[illegible]	Clinical	[illegible]	DTI
on slice	11	1 (9%) *	4 (36%)	8 (73%)
off slice	11	1 (9%) *	0 (0%) *	8 (73%)
Combined	22	[illegible] *	4 (18%) *	16 (73%)

Table 8. Visual observation results of 12GA stab injury on axial MRI scans (clinical, proton density and DTI). Each row of the table corresponds to a common MRI slice shared by each of the axial MRI sequences. Absolute number and percentage of successful injury observations are reported for each MRI category. A single * denotes injury observation significantly less than DTI sequences for a given slice plane. Significance is at the $p < 0.05$ level.

Dynamic loading

Overall, the introduction of compressive loading increased the percentage of 2mm core visualization for each sequence (Tables 9). Clinical sequence observation of injury increased significantly from 41% to 68% ($p = 0.035$, Wilcoxon Paired-sample test). Proton Density injury observation remained at 50% visualization, and DTI visualization of 2mm core injury increased from 86% to 96%, both failing to achieve significant increases in injury observation with loading ($p = 0.750$ and 0.250 respectively, Wilcoxon Paired-sample test).

The improvements in 2mm core visualization under dynamic loading were present at both the "on" and "off" slices (Table 9). The clinical sequences reached 82% injury detection for the "on" slices, just behind both the proton density sequence (100%) and DTI maps (100%). Injury visualization with DTI was not found to be significantly higher than either the clinical or proton density sequences ($p = 0.25$ and 1.0 respectively, Wilcoxon Paired-sample test on the injury slice plane). Similar to the unloaded case, the 2mm core was almost equally visualized in the "off" slices with DTI (91%), while the percentage of injury visualization for the clinical sequence increased (55%), and decreased slightly for the proton density sequence (0%). Both remained significantly less able to visualize the 2mm core injury than the DTI sequence on the "off" slices ($p = 0.109$ and 0.001 respectively, Wilcoxon Paired-sample test).

Even with the sharp increase in clinical visualization (41% to 68%), DTI map 2mm core injury visualization (96%) remained significantly larger with dynamic loading ($p = 0.035$, Wilcoxon Paired-sample test) (Table 9). Injury observation under load conditions with DTI also remained significantly higher than proton density injury visualization (50%) ($p = 0.001$, Wilcoxon Paired-sample test).

2mm with load	# IVDs	Clinical	Proton Density	DTI
on slice	11	9 (41%)	11 (100%)	11 (100%)
off slice	11	6 (55%)	0 (0%) *	10 (91%)
combined	22	15 (68%) *	11 (50%) *	21 (95%)

Table 9. Visual observation results of 2mm core injury with compressive load on axial MRI scans (clinical, proton density and DTI). Each row of the table corresponds to a common MRI slice shared by each of the axial MRI sequences. Absolute number and percentage of successful injury observations are reported for each MRI category. A single * denotes injury observation significantly less than DTI sequences for a given slice plane. A double ** denotes significant increase in injury observation with dynamic loading for an individual MRI category. Significance is at the $p < 0.05$ level.

Compressive loading also had an impact on the overall 12GA stab injury visualization. The clinical sequences improved their injury visualization from 9% to 14%, while proton density observation remained the same at 18%, and DTI 12GA stab visualization decreased from 73% to 55% (Table 10). None of these changes in injury visualization resulted in statistical differences between unloaded and loaded visualization ($p = 0.500$, 0.688, and 0.172 respectively, Wilcoxon Paired-sample test).

For the "on" slices, 12GA stab visualization continued to be above 50% for the DTI maps (64%), and proton density injury visualization (36%) was not found to be significantly less ($p = 0.188$, Wilcoxon Paired-sample test) given compressive loading. Clinical sequences on the other hand, were shown to have significantly less percentage of visualization (9%) than DTI ($p = 0.035$, Wilcoxon Paired-sample test). With the "off" slices, DTI had a reduced rate of injury visualization (46%). Clinical injury observation improved (18%), but DTI 12GA injury visualization was still larger, though there was no longer a significant difference detected ($p = 0.188$, Wilcoxon Paired-sample test). Again, the proton density sequence did not generate slices directly adjacent to the injury plane, and thus was significantly less able to visualize the 12GA stab injury than DTI ($p = 0.031$, Wilcoxon Paired-sample test).

Despite a reduction in DTI injury detection under load, there remained a statistical difference between DTI and the clinical and proton density 12GA injury visualization ($p = 0.011$ and 0.011 respectively, Wilcoxon Paired-sample test) (Table 10).

12GA with load	# FVIs	Clinical	Proton Density	DTI
on slice	11	1 (9%) *	4 (36%)	7 (64%)
off slice	11	2 (18%)	0 (0%) *	5 (46%)
Combined	22	3 (14%) *	4 (18%) *	12 (55%)

Table 10. Visual observation results of 12GA stab injury with compressive load on axial MRI scans (clinical, proton density and DTI). Each row of the table corresponds to a common MRI slice shared by each of the axial MRI sequences. Absolute number and percentage of successful injury observations are reported for each MRI category. A single * denotes injury observation significantly less than DTI sequences for a given slice plane. A double ** denotes significant increase in injury observation with dynamic loading for an individual MRI category (no significant difference in detection with loading observed). Significance is at the $p < 0.05$ level.

4.3 Quantitative injury visualization analysis:

A MANOVA was used to conduct a statistical comparison of various DTI measures (TraceADC, eigenvalues 1-3, and Fractional Anisotropy) obtained from the NP and the two generated injuries (2mm core and 12GA). The quantitative injury visualization results showed that DTI measures (TraceADC, eigenvalues 1-3, and fractional anisotropy) were significantly different between the NP and either injury (2mm core or 12GA stab injury). Dynamic loading did not change these results globally, but it did introduce some significant interactions between the ROI and Slice Plane factors. Last, a comparison between the 2mm core and 12GA stab injuries indicated that there was not a significant difference between most of the two injuries' DTI measures, but that under dynamic loading, the Slice Plane variable became a statistically relevant factor for three of the five DTI measure comparisons. The results from the 2x5 MANOVA are summarized in Tables 11 and 12 below. Confirmation of diffusion weighting (SI attenuation through the addition of diffusion gradients) in the DTI scans, as well as an

assessment of the NP as a comparison to the injuries' DTI results through CNR measurements can be seen in Appendix E.

No Load	TraceADC	[illegible]	[illegible]	[illegible]	[illegible]
2mm core - NP	*	***	*	*	*
12GA stab - NP	*		*	*	*
Load					
2mm core - NP	*, ***	*	*	*, ***	*
12GA stab - NP	*, ***		*	*	*

Table 11. Summary of no load and load results from the 2x5 MANOVA of 2mm core – NP, and 12GA stab - NP DTI data. A single * denotes a significant difference between the DTI measures of the injury and NP ROIs, a double ** denotes a significant difference between DTI measures of the "on" and "off" injury Slice Planes (no significant difference between averages with loading observed), and a triple *** is for a significant interaction between the ROI and Slice Plane factors. Significance was considered to be at the $p < 0.05$ levels.

No Load	TraceADC	[illegible]	[illegible]	[illegible]	[illegible]
2mm - 12GA		*			
Load					
2mm - 12GA	**		**	**	

Table 12. Summary of no load and load results from the 2x5 MANOVA of the 2mm core – 12GA stab DTI data. A single * denotes a significant difference between the DTI measures of the injury ROIs, a double ** denotes a significant difference between DTI measures of the "on" and "off" injury Slice Planes, and a triple *** is for a significant interaction between the ROI and Slice Plane factors. Significance was considered to be at the $p < 0.05$ levels.

Descriptive statistics

Below are the descriptive statistics for the 5 DTI measurements (TraceADC, diffusivity along principle eigenvector directions (eigenvalues 1-3), Fractional Anisotropy) that outline the diffusion properties of the 2mm core and 12GA stab injuries, as well as the NP in the unloaded (Table 13) and loaded conditions (Table 14). In general, the DTI measures of the NP are larger in magnitude than both the 2mm core and 12GA stab injuries. Dynamic loading results in both injuries surpassing the NP's eigenvalue 1 value, and there is a general trend for the injuries' TraceADC and eigenvalue DTI measures to increase while the NP's DTI values tend to decrease under loading conditions. Finally, the DTI data from the 12GA stab are larger than the 2mm core injury, but dynamic loading reversed this for each of the DTI measures except for Fractional Anisotropy. Because of the low SNR out of the AF (~ 6), its DTI results have been rejected.

	TraceADC (mm^2 /sec)	Eigenvalue1 (mm^2 /sec)	Eigenvalue2 (mm^2 /sec)	Eigenvalue3 (mm^2 /sec)	Fractional Anisotropy (0 to 1)
[redacted]					
Mean	0.000794	0.001815	0.00080	0.000141	0.74
Std Error	0.000078	0.000088	0.000084	0.000039	0.03
Std Dev.	0.000323	0.000361	0.000345	0.000163	0.11
Minimum	0.000315	0.001322	0.000364	0.000000	0.53
Maximum	0.001405	0.002515	0.001484	0.000525	0.87
N = 17					
[redacted]					
Mean	0.000906	0.002095	0.000898	0.000171	0.74
Std Error	0.000084	0.000088	0.000066	0.000035	0.02
Std Dev.	0.000327	0.000340	0.000255	0.000134	0.08
Minimum	0.000941	0.001523	0.000335	0.000000	0.57
Maximum	0.001305	0.002766	0.001275	0.000382	0.90
N =15					
[redacted]					
Mean	0.001423	0.001919	0.001381	0.000974	0.33
Std Error	0.000018	0.000040	0.000022	0.000033	0.02
Std Dev.	0.000085	0.000186	0.00010	0.000155	0.10
Minimum	0.001223	0.001613	0.001105	0.000438	0.22
Maximum	0.001584	0.002441	0.001582	0.001157	0.62
N = 22					

Table 13. Descriptive statistics for DTI measures from 2mm core, 12GA stab injuries, and NP ROIs.

	TraceADC (mm^2 /sec)	Eigenvalue1 (mm^2 /sec)	Eigenvalue2 (mm^2 /sec)	Eigenvalue3 (mm^2 /sec)	Fractional Anisotropy (0 to 1)
[illegible]					
Mean	0.001042	0.002173	0.000995	0.000245	0.72
Std Error	0.000081	0.000094	0.000078	0.000046	0.02
Std Dev.	0.000378	0.000441	0.000367	0.000215	0.08
Minimum	0.000330	0.001305	0.000363	0.000000	0.52
Maximum	0.001691	0.002864	0.001729	0.000734	0.81
N = 22					
[illegible]					
Mean	0.000957	0.002103	0.000926	0.000174	0.75
Std Error	0.000093	0.000115	0.000089	0.000051	0.02
Std Dev.	0.000385	0.000472	0.000366	0.000209	0.09
Minimum	0.000330	0.001272	0.000286	0.000000	0.50
Maximum	0.001820	0.002926	0.001853	0.000696	0.84
N =17					
[illegible]					
Mean	0.001407	0.001902	0.001373	0.000956	0.33
Std Error	0.000027	0.000035	0.000032	0.000044	0.02
Std Dev.	0.000129	0.000164	0.000150	0.000207	0.11
Minimum	0.001021	0.001587	0.000932	0.000162	0.23
Maximum	0.001621	0.002184	0.001636	0.001154	0.74
N = 22					

Table 14. Descriptive statistics for DTI measures from 2mm core, 12GA stab injuries, and NP ROIs under load conditions.

Statistical analysis considerations:

Before conducting statistical analyses on the quantitative data, some issues require consideration. First, despite the use of SI thresholding for improved injury visualization, each ROI did not present itself equally in terms of clarity of visualization in the DTI images of the specimen population (11 IVDs, or 22 MRI slices). In some cases no injury could be detected. Recall that the MRVision data acquisition boundaries were drawn directly onto the DTI maps. While the NP was always present, the qualitative results show that DTI observation of the injuries was not always possible (the number of visualizations is higher in this analysis as visualization criteria was not as stringent). This inequality of visualizations is reflected by the number of data points (N) reported for each ROI in Tables 13 and 14. Because the statistical tests used in this analysis require equal points between sites of comparison, any removal of data would have reduced the power of the analysis. For this reason, a separate statistical analysis was done for each of the 2mm core versus NP, 12GA stab versus NP, and 2mm core versus 12GA stab comparisons of DTI data. These analyses were then repeated in the loaded case bringing the total number of statistical analyses to six. This approach allowed two ROI groups to be matched per analysis. The results are reported below.

Second, the nature of tissue harvesting made it difficult to remove the same IVD levels (e.g. L1 to L4) during each spine segment extraction. Therefore, the same IVD levels were not imaged between specimens. Because of this circumstance, it was assumed that DTI measures between lumbar IVD levels are equivalent for the three ROIs. A statistical evaluation of this assumption was conducted and is presented in Appendix F.

Finally, from qualitative analysis, it was realized that injury visualization could be broken down into "on" and "off" slices. Therefore, it was assumed that the diffusion properties of "on" and "off" images may differ. As a result, slice plane was included as an additional factor to ROI in the statistical comparison of DTI measures.

Quantitative results

Beginning with the comparison of DTI measures across the 2mm core injury and NP ROIs, the overall test of univariate models from the 2 x 5 (Slice Plane by ROI) fixed effects MANOVA suggested that each of the DTI measures, save eigenvalue 1, had a factor that varied significantly between the 2 ROIs (Table 15). Upon further analysis, it was shown that the eigenvalue 1 dependent variable did not reach significance for the ROI factor ($p = 0.307$, MANOVA), but that there was a significant interaction between the Slice Plane and ROI factors ($p = 0.032$, MANOVA) (Table 16 and Figure 40). The ROI factors reached significance levels for each of the other DTI measures ($p = 0.000$, MANOVA).

DTI Measure	Source	Type III Sum of Squares	Degrees of Freedom	Mean Square	F	Probability value
TraceADC	Model	0.000003	3	0.000001	22.357	0.000*
	Error	[illegible]	[illegible]	[illegible]		
	Total	0.000005	33			
Eigenvalue1	Model	[illegible]	[illegible]	[illegible]	[illegible]	0.082
	Error	0.000002	30	0.000000		
	Total	[illegible]	[illegible]			
Eigenvalue2	Model	0.000003	3	0.000001	15.924	0.000*
	Error	[illegible]	[illegible]	[illegible]		
	Total	0.000005	33			
Eigenvalue3	Model	[illegible]	[illegible]	[illegible]	[illegible]	0.000*
	Error	0.000001	30	0.000000		
	Total	[illegible]	[illegible]			
Fractional Anisotropy	Model	1.482119	3	0.494040	41.881	0.000*
	Error	[illegible]	[illegible]	[illegible]		
	Total	1.836009	33			

Table 15. Overall tests of univariate models for fixed effects MANOVA of DTI values for 2mm core injury and NP ROIs; "on" and "off" slice planes. A single * denotes a significant factor at the $p < 0.05$ level.

DTI Measure	Source	Type III Sum of Squares	Degrees of Freedom	Mean Square	F	Probability-value
TraceADC	on/off	0.000000	1	0.000000	2.235	0.145
	roi	[illegible]	[illegible]	[illegible]	[illegible]	[illegible]
	on/off*roi	0.000000	1	0.000000	2.343	0.136
Eigenvalue1	on/off	[illegible]	[illegible]	[illegible]	[illegible]	[illegible]
	roi	0.000000	1	0.000000	1.079	0.307
	on/off*roi	[illegible]	[illegible]	[illegible]	[illegible]	[illegible]
Eigenvalue2	on/off	0.000000	1	0.000000	1.726	0.199
	roi	[illegible]	[illegible]	[illegible]	[illegible]	[illegible]
	on/off*roi	0.000000	1	0.000000	1.451	0.238
Eigenvalue3	on/off	[illegible]	[illegible]	[illegible]	[illegible]	[illegible]
	roi	0.000006	1	0.000006	206.529	0.000*
	on/off*roi	[illegible]	[illegible]	[illegible]	[illegible]	[illegible]
Fractional Anisotropy	on/off	0.003949	1	0.003949	0.335	0.567
	roi	[illegible]	[illegible]	[illegible]	[illegible]	[illegible]
	on/off*roi	0.001844	1	0.001844	0.156	0.695

Table 16. Tests of univariate effects for fixed effects MANOVA of DTI values for 2mm core injury and NP ROIs; "on" and "off" slice planes. A single * denotes significance at the $p < 0.05$ level.

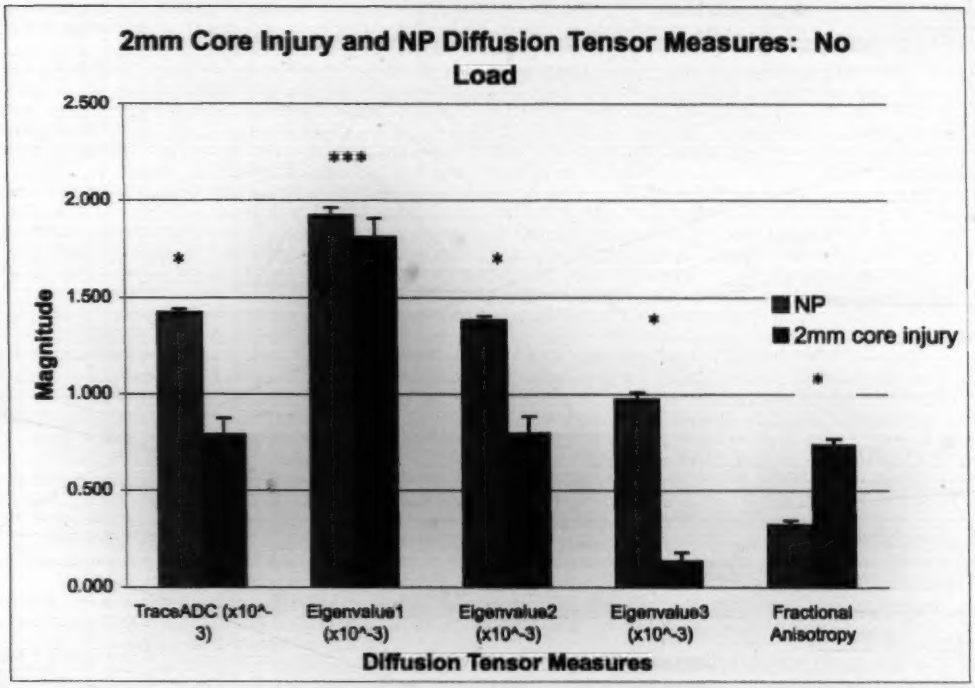

Figure 40. Diffusion tensor results for 2mm core injury and NP with standard error bars. TraceADC and eigenvalues 1, 2 and 3 are in units of mm^2 /sec, and Fractional Anisotropy is a ratio between 1 and 0. A single * denotes a significant difference between the DTI measures of the injury and NP ROIs, a double ** denotes a significant difference between the Slice Planes of each individual ROI, and a triple *** denotes a significant interaction between the ROI and Slice Plane factors. Significance was considered to be at the $p < 0.05$ level.

Moving from the larger to the smaller annular injury, many of the statistical descriptions for the 12GA stab injury are similar to that of the 2mm core injury. The overall univariate models continue to suggest that there are statistically significant differences within the DTI measures, aside from eigenvalue 1 (Table 17). Following the univariate effects test, there is no significant interaction for eigenvalue 1 in this case ($p = 0.477$, MANOVA), and the ROI factors continue to reach significance levels for each of the other DTI measures ($p = 0.000$, MANOVA) (see Table 18 and Figure 41).

DTI Measure	Source	Type III Sum of Squares	Degrees of Freedom	Mean Square	F	Probability Value
TraceADC	Model	0.000	3	0.000	11.227	0.000*
	Error	0.000	26	0.000		
	Total	0.000	29			
Eigenvalue1	Model	0.000	3	0.000	1.132	0.354
	Error	0.000	26	0.000		
	Total	0.000	29			
Eigenvalue2	Model	0.000	3	0.000	15.214	0.000*
	Error	0.000	26	0.000		
	Total	0.000	29			
Eigenvalue3	Model	0.000	3	0.000	15.041	0.000*
	Error	0.000	26	0.000		
	Total	0.000	29			
Fractional Anisotropy	Model	1.307	3	0.436	46.529	0.000*
	Error	0.243	26	0.009		
	Total	1.550	29			

Table 17. Overall tests of univariate models for fixed effects MANOVA of DTI values for 12GA stab injury and NP ROIs; "on" and "off" slice planes. A single * denotes a significant factor at the $p < 0.05$ level.

DTI Measure	Source	Type III Sum of Squares	[illegible]	Mean Square	F	Probability-value
TraceADC	on/off	0.000	1	0.000	0.063	0.803
	Roi	0.000	1	0.000	33.647	0.000*
	on/off*roi	0.000	1	0.000	0.241	0.628
Eigenvalue1	on/off	0.000	1	0.000	0.312	0.58
	Roi	0.000	1	0.000	2.718	0.111
	on/off*roi	0.000	1	0.000	0.116	0.477
Eigenvalue2	on/off	0.000	1	0.000	0.012	0.912
	Roi	0.000	1	0.000	45.797	0.000*
	on/off*roi	0.000	1	0.000	0.468	0.500
Eigenvalue3	on/off	0.000	1	0.000	0.000	0.99
	Roi	0.000	1	0.000	183.886	0.000*
	on/off*roi	0.000	1	0.000	0.021	0.885
Fractional Anisotropy	on/off	0.001	1	0.001	0.096	0.760
	Roi	1.208	1	1.208	119.283	0.000*
	on/off*roi	0.001	1	0.001	0.099	0.755

Table 18. Tests of univariate effects for fixed effects MANOVA of DTI values for 12GA stab injury and NP ROIs; "on" and "off" slice planes. A single * denotes significance at the $p < 0.05$ level.

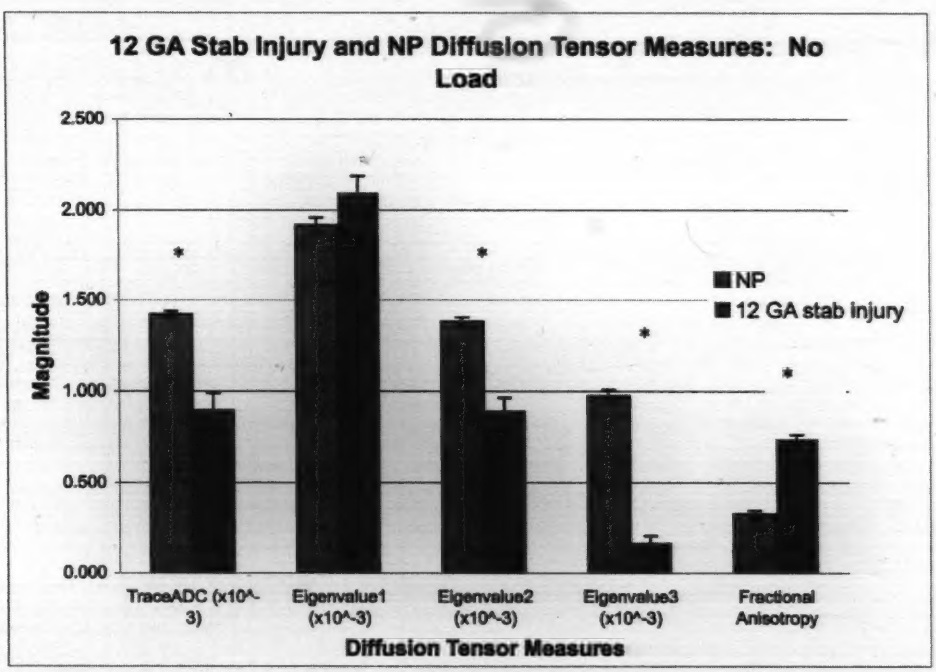

Figure 41. Diffusion tensor results for 12GA stab injury and NP with standard error bars. TraceADC and eigenvalues 1, 2 and 3 are in units of mm^2 /sec, and Fractional Anisotropy is a ratio between 1 and 0. A single * denotes a significant difference between the DTI measures of the injury and NP ROIs, a double ** is significant difference between the Slice Planes of each individual ROI, and a triple *** is for a significant interaction between the ROI and Slice Plane factors. Significance was considered to be at the $p < 0.05$ level.

Dynamic loading

Under dynamic loading, overall tests of the univariate models indicated that there was a significant difference between the 2mm core injury and NP ROIs for each of the DTI measures, including the eigenvalue 1 (Table 19). Following the univariate effects tests, both TraceADC and eigenvalue 3 were indicated as having significant interactions between the slice planes and ROIs ($p = 0.027$ and 0.040 respectively, MANOVA), while at the same time having reached significance for the ROI factor ($p = 0.000$ and 0.000 respectively, MANOVA). The remaining three DTI measures, eigenvalues 1, eigenvalue 2, and Fractional Anisotropy also reached significance for the ROI factor ($p = 0.009$, 0.000 and 0.000 respectively, MANOVA), without any significant interaction terms (Table 20 and Figure 42).

DTI Parameter	Source	Type III Sum of Squares	Degrees of Freedom	Mean Square	F	Probability value
TraceADC	Model	0.000	3	0.000	9.689	0.000*
	Error	0.000	40	0.000		
	Total	0.000	43			
Eigenvalue1	Model	0.000	3	0.000	5.641	0.021*
	Error	0.000	40	0.000		
	Total	0.000	43			
Eigenvalue2	Model	0.000	3	0.000	8.607	0.000*
	Error	0.000	40	0.000		
	Total	0.000	43			
Eigenvalue3	Model	0.000	3	0.000	10.525	0.000*
	Error	0.000	40	0.000		
	Total	0.000	43			
Fractional Anisotropy	Model	1.651	3	0.550	56.746	0.000*
	Error	0.388	40	0.010		
	Total	2.039	43			

Table 19. Overall tests of univariate models for fixed effects MANOVA of DTI values for 2mm core injury and NP ROIs; "on" and "off" slice planes under physiological loading conditions. A single * denotes a significant factor at the $p < 0.05$ level.

DTI Measure	Source	Type III Sum of Squares	Degrees of Freedom	Mean Square	F	Probability value
TraceADC	on/off	0.000	1	0.000	2.785	0.103
	roi	0.000	1	0.000	21.031	0.000*
	on/off*roi	0.000	1	0.000	5.280	0.027*
Eigenvalue1	on/off	0.000	1	0.000	0.012	0.913
	roi	0.000	1	0.000	7.559	0.009*
	on/off*roi	0.000	1	0.000	2.441	0.126
Eigenvalue2	on/off	0.000	1	0.000	1.509	0.226
	roi	0.000	1	0.000	21.866	0.000*
	on/off*roi	0.000	1	0.000	3.005	0.091
Eigenvalue3	on/off	0.000	1	0.000	2.410	0.131
	roi	0.000	1	0.000	139.513	0.000*
	on/off*roi	0.000	1	0.000	4.384	0.043*
Fractional Anisotropy	on/off	0.011	1	0.011	1.159	0.288
	roi	1.623	1	1.623	167.849	0.000*
	on/off*roi	0.012	1	0.012	1.272	0.266

Table 20. Tests of univariate effects for fixed effects MANOVA of DTI values for 2mm core injury and NP ROIs; "on" and "off" slice planes under physiological loading. A single * denotes significance at the $p < 0.05$ level.

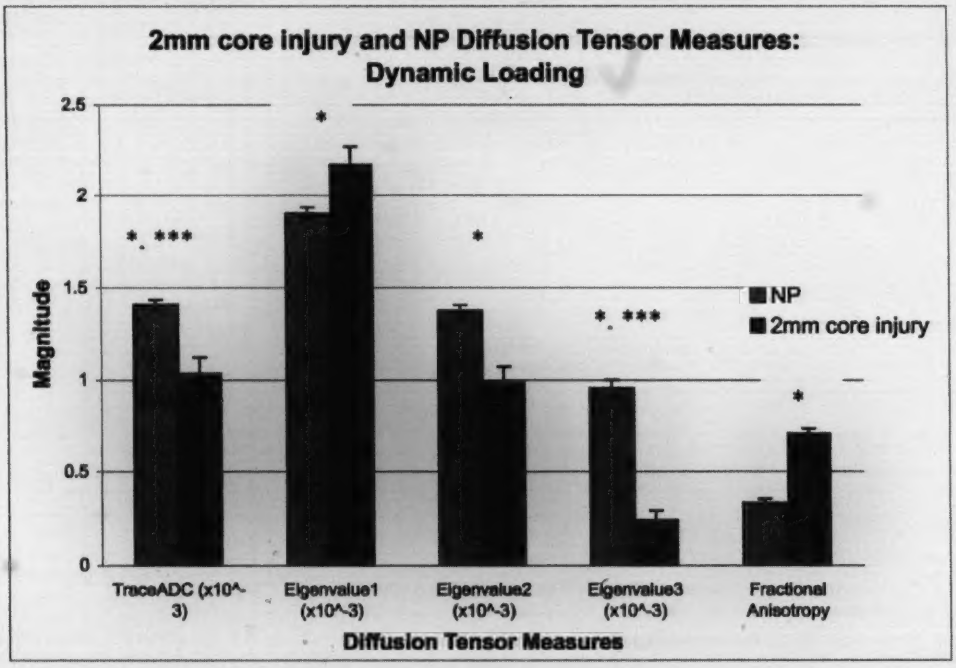

Figure 42. Diffusion tensor results for 2mm core injury and NP under loading conditions, with standard error bars. TraceADC and eigenvalues 1, 2 and 3 are in units of mm^2 /sec, and Fractional Anisotropy is a ratio between 1 and 0. A single * denotes a significant difference between the DTI measures of the injury and NP ROIs, a double ** is significant difference between the Slice Planes of each individual ROI, and a triple *** is for a significant interaction between the ROI and Slice Plane factors. Significance was considered to be at the $p < 0.05$ level.

Again the results with the 12GA stab under load are very similar to the 2mm core injury load data. Eigenvalue 1 is the only dependent variable to not reveal a significant factor in the overall test statistics (Table 21). In the univariate effects tests, a significant interaction between slice plane and ROI is shy of reaching significance levels for eigenvalue 1 ($p = 0.071$, MANOVA), and there continues to be no significant difference detected for the ROI factor ($p = 0.142$, MANOVA). The TraceADC DTI measure does present a significant interaction between the ROI and Slice Plane factors ($p = 0.037$, MANOVA), as well as a significant difference on the ROI factor ($p = 0.000$, MANOVA). The remainder of the DTI maps, continue to have the ROI factor indicated as showing a significant difference between the injury and NP ($p = 0.000$, MANOVA) (Table 22, Figure 43).

DTI Measure	Source	Type III Sum of Squares	[illegible]	[illegible]	[illegible]	[illegible]
TraceADC	Model	0.000002	3	0.000001	9.550	0.000*
	[illegible]	[illegible]	[illegible]	[illegible]	[illegible]	[illegible]
	Total	0.000004	33			
[illegible]	[illegible]	[illegible]	[illegible]	[illegible]	[illegible]	[illegible]
	Error	0.000003	30	0.000000		
	[illegible]	[illegible]	[illegible]	[illegible]	[illegible]	[illegible]
Eigenvalue2	Model	0.000002	3	0.000001	8.868	0.000*
	[illegible]	[illegible]	[illegible]	[illegible]	[illegible]	[illegible]
	Total	0.000004	33			
[illegible]	[illegible]	[illegible]	[illegible]	[illegible]	[illegible]	[illegible]
	Error	0.000001	30	0.000000		
	[illegible]	[illegible]	[illegible]	[illegible]	[illegible]	[illegible]
Fractional Anisotropy	Model	1.439665	3	0.479888	38.572	0.000*
	[illegible]	[illegible]	[illegible]	[illegible]	[illegible]	[illegible]
	Total	1.812904	33			

Table 21. Overall tests of univariate models for fixed effects MANOVA of DTI values for 12GA stab injury and NP ROIs; "on" and "off" slice planes under physiological loading conditions. A single * denotes a significant factor at the $p < 0.05$ level.

TraceADC	on/off	0.000000	1	0.000000	2.211	0.147
	roi					
	on/off*roi	0.000000	1	0.000000	4.761	0.037*
	roi	0.000000	1	0.000000	2.273	0.142
Eigenvalue2	on/off	0.000000	1	0.000000	1.587	0.218
	on/off*roi	0.000000	1	0.000000	3.721	0.063
	roi	0.000005	1	0.000005	98.728	0.000*
Fractional Anisotropy	on/off	0.015085	1	0.015085	1.212	0.280
	on/off*roi	0.004880	1	0.004880	0.392	0.536

Table 22. Tests of univariate effects for fixed effects MANOVA of DTI values for 12GA stab injury and NP ROIs; "on" and "off" slice planes under physiological loading. A single * denotes significance at the $p < 0.05$ level.

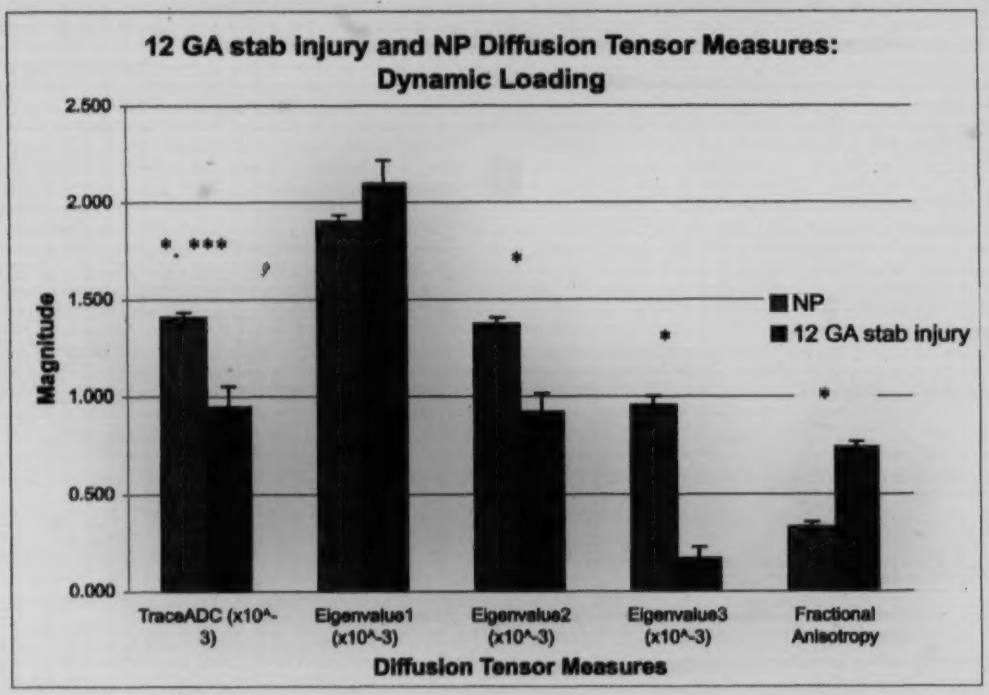

Figure 43. Diffusion tensor results for 12GA stab injury and NP under loading conditions, with standard error bars. TraceADC and eigenvalues 1, 2 and 3 are in units of mm^2 /sec, and Fractional Anisotropy is a ratio between 1 and 0. A single * denotes a significant difference between the DTI measures of the injury and NP ROIs, a double ** is significant difference between the Slice Planes of each individual ROI, and a triple *** is for a significant interaction between the ROI and Slice Plane factors. Significance was considered to be at the $p < 0.05$ level.

2mm core versus 12GA stab injury

With the comparison of diffusion properties from two kinds of annular injuries to the NP completed, the direct comparison between the 2mm core and 12GA stab injuries was conducted. In general, the graphical comparison of the DTI means in Figure 42 does not indicate that there are any substantial differences between the two injuries. The overall test statistics also did not indicate significant differences for any of the DTI measures (Table 23), however the univariate effects tests did identify ROI as being a significant factor for eigenvalue 1 ($p = 0.045$, MANOVA) (Table 24, Figure 44).

DTI Measure	Source	Type III Sum of Squares	Degrees of Freedom	Mean Square	F	Probability Value
TraceADC	Model	0.00000	3	0.00000	0.394	0.759
	Error	0.00000	18	0.00000		
	Total	0.00000	21			
Eigenvalue1	Model	0.00000	3	0.00000	1.435	0.267
	Error	0.00000	18	0.00000		
	Total	0.00000	21			
Eigenvalue2	Model	0.00000	3	0.00000	0.573	0.64
	Error	0.00000	18	0.00000		
	Total	0.00000	21			
Eigenvalue3	Model	0.00000	3	0.00000	0.41	0.747
	Error	0.00000	18	0.00000		
	Total	0.00000	21			
Fractional Anisotropy	Model	0.00798	3	0.00266	0.267	0.848
	Error	0.17949	18	0.00997		
	Total	0.18747	21			

Table 23. Overall tests of univariate models for fixed effects MANOVA of DTI values for 2mm core and 12GA stab injury ROIs; "on" and "off" slice planes. A single * denotes a significant factor at the $p < 0.05$ level.

DTI Measure	Source	Type III Sum of Squares	Degrees of freedom	Mean Square	F	Probability value
TraceADC	on/off	0.000000	1	0.000000	0.221	0.644
	roi	[illegible]	[illegible]	[illegible]	[illegible]	[illegible]
	on/off*roi	0.000000	1	0.000000	0.563	0.463
Eigenvalue1	on/off	[illegible]	[illegible]	[illegible]	[illegible]	[illegible]
	roi	0.000001	1	0.000001	4.622	0.045*
	on/off*roi	[illegible]	[illegible]	[illegible]	[illegible]	[illegible]
Eigenvalue2	on/off	0.000000	1	0.000000	0.107	0.747
	roi	[illegible]	[illegible]	[illegible]	[illegible]	[illegible]
	on/off*roi	0.000000	1	0.000000	0.184	0.673
Eigenvalue3	on/off	[illegible]	[illegible]	[illegible]	[illegible]	[illegible]
	roi	0.000000	1	0.000000	0.042	0.840
	on/off*roi	[illegible]	[illegible]	[illegible]	[illegible]	[illegible]
Fractional Anisotropy	on/off	0.002715	1	0.002715	0.272	0.608
	roi	[illegible]	[illegible]	[illegible]	[illegible]	[illegible]
	on/off*roi	0.005245	1	0.005245	0.526	0.478

Table 24. Tests of univariate effects for fixed effects MANOVA of DTI values for 2mm core and 12GA stab injury ROIs; "on" and "off" slice. A single * denotes significance at the $p < 0.05$ level.

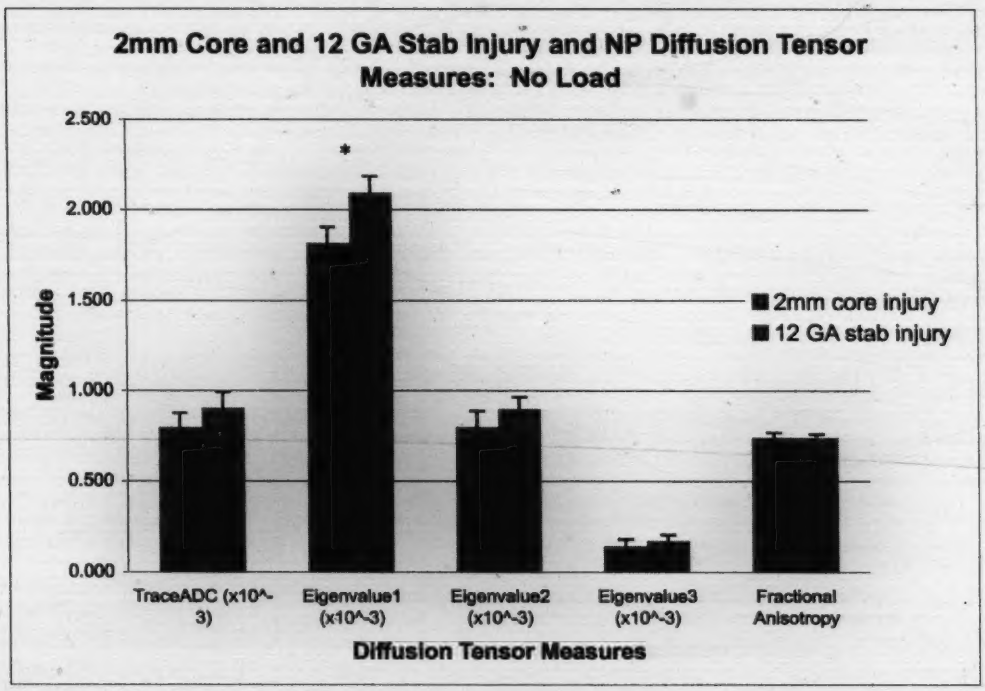

Figure 44. Diffusion tensor results for 2mm core and 12GA stab injuries with standard error bars. TraceADC and eigenvalues 1, 2 and 3 are in units of mm^2 /sec, and Fractional Anisotropy is a ratio between 1 and 0. A single * denotes a significant difference between the DTI measures of the injury and NP ROIs, a double ** is significant difference between the Slice Planes of each individual ROI, and a triple *** is for a significant interaction between the ROI and Slice Plane factors. Significance was considered to be at the $p < 0.05$ level.

Dynamic loading

With dynamic loading the overall test results continued to indicate a lack in significant differences between DTI measures for the 2 injuries (Table 25). However, in the univariate effects tests, slice plane did materialize as a significant factor for TraceADC, eigenvalue 2, and eigenvalue 3 ($p = 0.017$, 0.031, and 0.033, MANOVA). Fractional anisotropy also came close to reaching significance for the Slice Plane factor ($p = 0.055$, MANOVA) (Table 26, Figure 45).

DTI Measure	Source	Type III Sum of Squares	Degrees of Freedom	Mean Square	F	Probability-value
TraceADC	Model	0.000001	3	0.00000	2.463	0.082
	Error					
	Total	0.000005	33			
Eigenvalue1	Model					
	Error	0.000006	30	0.00000		
	Total					
Eigenvalue2	Model	0.000001	3	0.00000	1.932	0.146
	Error					
	Total	0.000004	33			
Eigenvalue3	Model					
	Error	0.000001	30	0.00000		
	Total					
Fractional Anisotropy	Model	0.049727	3	0.01658	2.169	0.112
	Error					
	Total	0.27894	33			

Table 25. Overall tests of univariate models for fixed effects MANOVA of DTI values for 2mm core and 12GA stab injury ROIs; "on" and "off" slice planes under physiological loading conditions. A single * denotes a significant factor at the $p < 0.05$ level.

DTI Measure	Source	Type III Sum of Squares	Degrees of Freedom	Mean Square	F	Probability-value
TraceADC	On/off	0.000001	1	0.000001	6.399	0.017*
	roi	[illegible]	1	[illegible]	[illegible]	[illegible]
	on/off*roi	0.000000	1	0.000000	0.034	0.856
[illegible]	[illegible]	[illegible]	[illegible]	[illegible]	[illegible]	[illegible]
	roi	0.000000	1	0.000000	0.528	0.473
	[illegible]	[illegible]	[illegible]	[illegible]	[illegible]	[illegible]
Eigenvalue2	on/off	0.000001	1	0.000001	5.164	0.031*
	roi	[illegible]	[illegible]	[illegible]	[illegible]	[illegible]
	on/off*roi	0.000000	1	0.000000	0.029	0.866
[illegible]	[illegible]	[illegible]	[illegible]	[illegible]	[illegible]	[illegible]
	roi	0.000000	1	0.000000	2.021	0.166
	[illegible]	[illegible]	[illegible]	[illegible]	[illegible]	[illegible]
Fractional Anisotropy	on/off	0.030533	1	0.030533	3.996	0.055
	roi	[illegible]	[illegible]	[illegible]	[illegible]	[illegible]
	on/off*roi	0.000322	1	0.000322	0.042	0.839

Table 26. Tests of univariate effects for fixed effects MANOVA of DTI values for 2mm core and 12GA stab injury ROIs; "on" and "off" slice planes under physiological loading. A single * denotes significance at the $p < 0.05$ level.

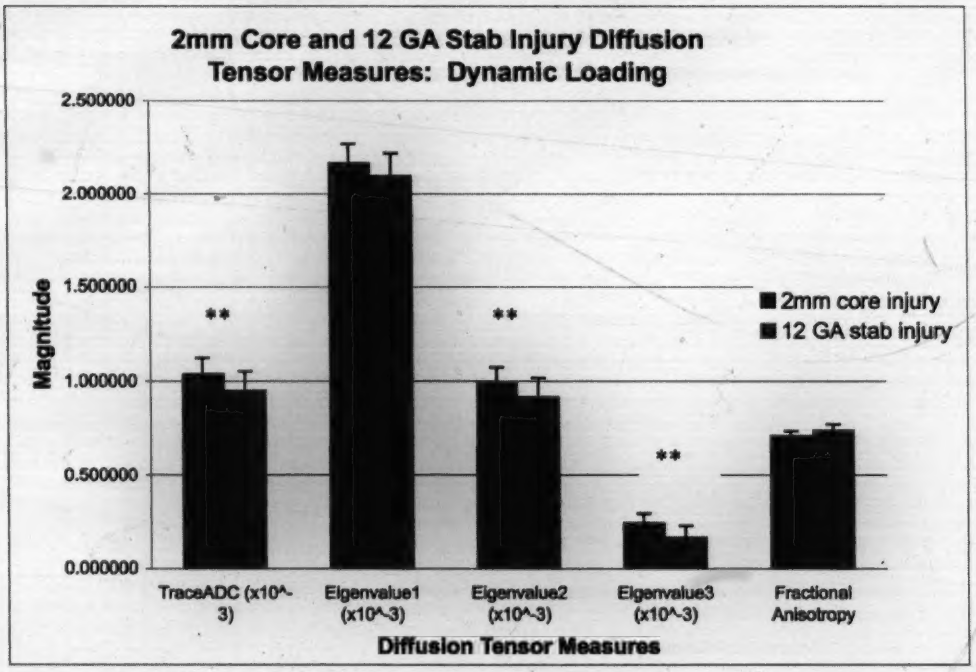

Figure 45. Diffusion tensor results for 2mm core and 12GA stab injuries under load conditions, with standard error bars. TraceADC and eigenvalues 1, 2 and 3 are in units of mm^2 /sec, and Fractional Anisotropy is a ratio between 1 and 0. A single * denotes a significant difference between the DTI measures of the injury and NP ROIs, a double ** is significant difference between the Slice Planes of each individual ROI, and a triple *** is for a significant interaction between the ROI and Slice Plane factors. Significance was considered to be at the $p < 0.05$ level.

Chapter 4 references

There are no references for this chapter.

Chapter 5: Discussion

Overview

In Chapter 4, the qualitative and quantitative results of this master's research were reported. To discuss the meaning and relevance of these results, this chapter is separated into five sections.

The first three sections will assess how the results of this work support, or do not support, the three hypotheses outlined in Chapter 1. The first hypothesis suggested that the ability of qualitative DTI maps to detect artificially generated AF tears would surpass that of clinical MRI. The results from the qualitative analysis support this hypothesis. The second hypothesis suggested that the quantitative DTI measurements of the IVD would enable the differentiation between the NP and artificial injuries within the AF. This hypothesis was partially supported by quantitative data. The third hypothesis suggested that dynamic compression would improve DTI's visual and quantitative sensitivities to artificially generated AF tears. This hypothesis was supported in part by the qualitative and quantitative data.

The last two sections of this chapter will discuss the strengths, weaknesses and the clinical significance of the project's results.

5.1 Hypothesis 1:

The first hypothesis of this thesis predicted that qualitative DTI maps would have a greater ability to detect artificially generated AF injuries when compared to conventional MRI sequences. Given the voxel resolution of the sequences in this study, the results from the qualitative analysis supported this hypothesis as DTI visualization of the 2mm core and 12GA injuries were significantly higher than conventional or "clinical" sequences ($p = 0.001$ and 0.000 respectively, Wilcoxon Paired-sample test). Injury visualization using qualitative DTI maps reached 86% for the larger 2mm core injury and 73% for the smaller 12GA stab injury.

Comparison to other literature

The qualitative results that support Hypothesis 1 are in agreement with *in vivo* MRI tear detection rates reported previously in studies by Aprill and Bogduk, and Schelhas *et al.* In these studies, radial tear detection by clinical MRI was rated as high as 86% (Aprill and Bogduk, 1992, Schellhas et al., 1996). These radial tear detection rates were determined by comparing the number of conventional MRI detections to that of a gold standard. The gold standard used in these studies was x-ray discography and/or pain provocation through the injection of discography contrast dye into the IVD.

Instead of being significantly larger, the DTI tear visualization results from this study are similar to the conventional MRI detection rates reported in Aprill and Bogduk, and Schelhas *et al.* One possible explanation for this result is that discographic detection, as a gold standard, is not 100% accurate – an assumption inferred by the authors of studies using this technique. Given this assumption, conventional MRI AF tear detection rates published by Aprill and Bogduk, and Schelhas *et al.* could have been inflated as additional AF tears could have been present, but not detected by the gold standard. If this were the case, the MRI detection rates from Aprill and Bogduk, and Schelhas *et al.* could actually have been closer to the conventional MRI detection rates observed in this study. Results from earlier cadaveric investigations support this argument where conventional MRI tear detection rates of 67% were observed (Kakitsubata et al., 2003). While this is still a higher conventional MRI detection rate than what was found in this study, it is not as large a difference as the comparison with the discographic-based conventional MRI detection rates (Table 27).

Study (MRI method)	Percentage of radial tear detection
Aprill and Bogduk (conventional)	86%
Schelhas (conventional)	82%
Kakistubata (conventional)	67%
final experiment (DTI)	86% (2mm), 73% (12GA)
final experiment (conventional)	41% (2mm), 9% (12GA)

Table 27. Percentage of radial tear detection. Conventional MRI radial tear detection reported from a number of studies compared to the DTI and conventional MRI detection rates from this study.

In comparison to x-ray discography, or the gold standard used by Aprill and Bogduk, and Schelhas *et al.*, DTI is obviously less sensitive to tears in the AF. One explanation for the insensitivity of DTI to radial tears compared to discography is that for the DTI procedure, there is no use of contrast material or pain generation assisting the detection of AF tears. While these techniques are helpful in the identification of tears, there is concern related to the invasiveness of these techniques as they may exacerbate injury in IVD due to infection, or create morphological changes due to mis-positioned contrast dye injection (Guyer, Ohnmeiss, & NASS, 2003, Lander, 2005). Realistically, any debate about the efficacy of DTI maps in the detection of IVD injury compared to discography is premature in that the DTI data from this thesis were not collected from symptomatic humans in a clinical setting, however, the detection rate achieved in this study suggest that DTI visualization of AF tears holds promise, especially since it is not associated with invasive procedures such as contrast injection.

In general, improvements in DTI map tear visualization could be realized with the use of a SENSE-EPI coil that was designed specifically to optimize signal reception from the spine. In this study, the coil that was used was not optimal as it was a head coil designed to provide MRI visualization for a much larger volume/object. Furthermore, the DTI sequence used in this study was adapted so that it could be compared to other standard MRI sequences. This meant that parameters such as FOV and slice thickness had to be matched with the other sequences in the imaging protocol to promote a fair comparison

of visualizations. As parameters such as these can be adjusted to improve image quality, the DTI sequence lacked specifically optimized parameters for IVD visualization. The clinical MRI sequences used in Aprill and Bogduk, and Schelhas *et al.'s* studies were most likely specialized specifically for spinal imaging, as they did not require the same geometric parameters as the discographic scans. Other parameters of the DTI sequence such as bandwidth (can reduce TE for better reception of signal from the AF) and diffusion gradient directions (can improve diffusion weighting given injury geometry) could also have been optimized, but further gains in visualization was not deemed necessary given the exploratory nature of this study.

Many of these same coil and sequence related DTI limitations were also applicable to the conventional MRI sequences used in this study. These factors may have contributed to the observation that conventional radial AF tear detection rates from this study were less than what was reported for the conventional MRI sequences in the discography studies.

Discussion

Support of Hypothesis 1 by the results of this study was expected for three reasons. First, conventional MRI sequences have a low sensitivity to AF tears due to many factors including the size of AF tears, the resolution of the detection system, the magnetic relaxation properties of the AF, and the avascular nature of the IVD. In contrast to conventional MRI, diffusion MRI generates additional contrast by sensitizing visualization to diffusion patterns within tissues. Diffusion MRI is also less dependent on high-resolution visualization of structures to identify pathology. Given theses properties, it was expected and shown that DTI maps would be able to achieve a higher rate of AF tear visualization than conventional MRI sequences.

Second, the AF is a structure with high water content and varying degrees of water diffusion. For this reason, a tear in the AF could have the potential to disrupt the AF's hydrostatic system beyond injury boundaries, improving the chances of injury visualization with DTI.

The third reason why DTI visualization of IVD injury was expected to be greater than conventional MRI, is that this technique produces five different diffusion maps (TraceADC, eigenvalues 1 – 3, Fractional Anisotropy) compared to the single image produced by conventional MRI. By using 5 different DTI maps for injury visualization, the probability that abnormal patterns in the AF could be identified would be increased assuming that more than one of these imaging sequences was advantageous for AF tear imaging. With respect to these 5 DTI maps, the three eigenvalue maps were particularly helpful in corroborating injury observation by the TraceADC and Fractional Anisotropy maps. The voxels of these three DTI maps reflect ADC magnitudes in three orthogonal directions. The eigenvalue 1 map represents the vector with the largest ADC values, followed by eigenvalue maps 2 and 3. When visualizing tissue structures that encourage anisotropic diffusion, the eigenvalue 1 maps are bright as diffusion is high, however, because diffusion is happening in primarily one direction, eigenvalue maps 2 and 3 tend to be increasingly darker over the same voxel. In this case, this effect maintained only the visualization of the central portion of the artificial injuries, bringing the injuries into focus when each eigenvalue map was observed. This facilitated injury detection.

As expected, tear detection was best with image slices aligned to the injury itself ("on" slices). Being aligned with the injury provided the best opportunity for imaging because this slice provided the most direct visualization of the nuclear material and/or inter-cellular fluid in the injury. This presence of a strong signal source is what probably caused no significant differences in injury visualization to be detected between DTI and the other sequences for the 2mm core injury. Interestingly, DTI tear detection was also possible from "off" slices. That diffusion abnormalities related to tearing extend beyond the physical boundaries of the injury itself is likely the reason for this observation. This phenomenon may be explained due to increased fluid diffusion towards an injury site because AF tissues exhibit varying degrees of water permeability (Gu et al., 1999) and IVD mechanical systems are so closely associated with fluid movement within the IVD. In addition, isotropic diffusion between lamellae may be blocked due to injury causing fluid to pool just outside the immediate injury site. The process of generating an injury could have also caused lower level damage in tissue surrounding the injury site. The

ability of DTI to "see" an injury beyond its physical borders makes it a much more powerful tool in the detection of AF tears, given that the area of potential detection is larger than conventional MRI assuming that slices thicknesses are equal.

While the results related to Hypothesis 1 are encouraging, a potential confounder is the presence of imaging artifacts that can be mistaken for injuries. These artifacts are thought to be caused by the presence of air bubbles in the USG trapped against the paravertebral tissue; and the attachment of beads to the IVD. While optimization of DTI injury visualization through SI thresholding did reduce the presence of the artifacts related to the USG and slice plane demarcation beads, this potential confounder was not eliminated. In a clinical environment, an imaging medium such as USG would no longer be required and therefore, its absence may eliminate artifacts related to air bubbles along the IVD tissue. Likewise, the inability to employ demarcation beads for injury slice plane selection would eliminate any artifacts that were a result of their presence on the IVD. In this case, any improvement due to loss of artifacts may be offset due to loss of specific injury slice plane information. With that being said, the ability of DTI to visualize injury "off" of aligned slice planes may compensate for the loss of injury slice plane information. Though the loss of artifacts related to USG and demarcation beads can be assumed, another major issue for future consideration would be artifacts caused by magnetic field inhomogenieties due to boney articulations of the spine and CSF. Because these structures were removed from the spine segments used in this study, these factors may introduce new challenges to the use of DTI in the detection of AF tears.

It should be noted that although the conventional MRI detection rates were significantly lower than detection by DTI maps in this study, a variation of conventional MRI imaging demonstrated promising results. In this project, a proton density sequence was added because of initial observations in the early experimentation phase of this research. These observations indicated that similar to DTI, a proton density sequence could achieve axial visualization of a stab injury in the AF that was not detectable using conventional MRI. The addition of a proton density sequence was also thought to be advantageous because one of the major issues associated with IVD imaging is the short relaxation time of the

AF, and the proton density sequence is characterized by a short TE and a long TR. Unfortunately, the sequences available on the clinical magnet used in this study would not allow the appropriate TE parameter (30 – 40msec for AF) to be set below a certain level (+60msec) for most of the sequences in the imaging protocol. To reduce the TE past these cut-off points, an MRI sequence (AxT2Measure) that generates a series of images at discrete TE increments was able to produce a low TE or "proton density" image. The results from this sequence, using the "on" injury slice plane, were better than the clinical sequences, and they were also found to be as good as the DTI sequences in a number of injury observations. Compared to DTI, the quality of visualization of the proton density sequence was much clearer, though there was some blurring as well as some streaking in the images due to the air bubbles and beads on the IVD surface. Ultimately, the AxT2Measure sequence providing the proton density images was only able to generate an image on every other slice due to a default 100% distance factor between slices. This limitation caused the proton density sequence to be significantly less sensitive to both artificial injuries compared to DTI injury visualization – this technique still must be aligned to the injury itself. As will be discussed in the last two sections of this chapter, although the DTI sequence used in this study is clinically available, limitations must be overcome before it is ready for clinical implementation in AF tear detection. On the other hand, a proton density sequence, could be adapted for implementation in clinical assessments of AF tears.

5.2 Hypothesis 2:

The second hypothesis of this study was that quantitative DTI AF tear measurements (TraceADC, eigenvalues 1 - 3, Fractional Anisotropy) would be significantly different from the same measures obtained from the NP. The NP was selected as a standard for quantitative AF tear assessment due to DTI's reliance on good SNR, and the AF's chronic lack of signal in T2W sequences. Overall, the results from the final experiment support this hypothesis as both the 2mm core and 12GA stab injuries had significantly different DTI values than the NP for all five of the DTI measures except for eigenvalue 1. Specifically, the eigenvalue 1 results demonstrated a significant interaction between the ROI and Slice Plane factors between the 2mm core and NP DTI data (Figure 46).

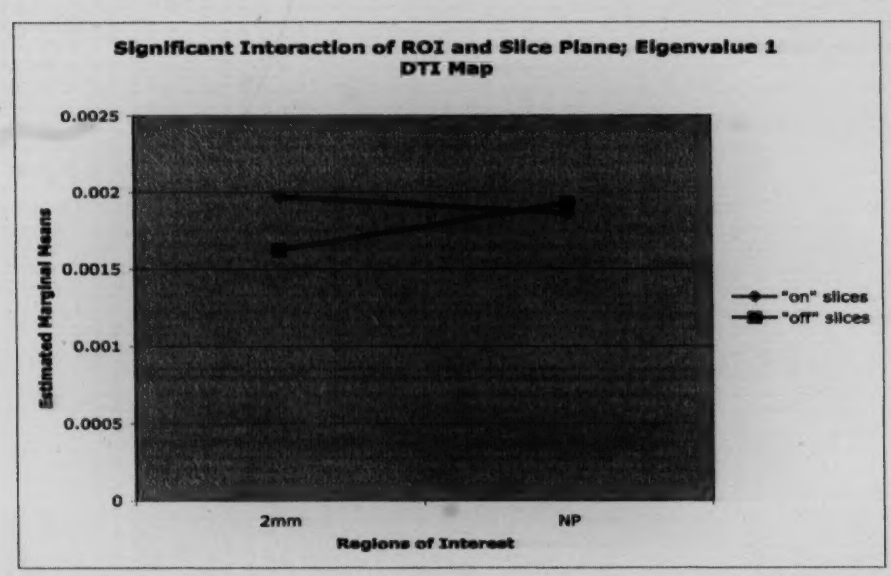

Figure 46. Significant interaction between ROI and Slice Plane for the eigenvalue 1 data of the 2mm core and NP ROIs.

Comparison to other literature

The author is aware of no prior study that has compared DTI data of injuries in the AF to other regions in the IVD. In general, prior studies have investigated changes in diffusion data between loading periods (Chiu et al., 2001, Drew et al., 2004), and/or the effect of degenerative change on diffusion data from the NP (Kealey et al., 2005, Kerttula et al., 2001, Niinimaki et al., 2007).

Of the studies that are most applicable for the comparison to the DTI results described in this thesis, Kealey *et al.* reported mean or TraceADC values for healthy NPs of 0.002208 mm^2/s (free water at room temperature, ~0.0025 mm^2/s) and values of 0.002094 mm^2/s in abnormal NPs (as indicated by conventional MRI degenerative findings) (Kealey et al., 2005). The TraceADC values from the abnormal NPs in Kealey *et al.*'s study were closest to the experimental result from this research of 0.001423 mm^2/s. One main difference between the two studies that may explain the differences between TraceADC

results is the temperature of the IVD during imaging. As Kealey *et al.*'s experiment was done *in vivo*, diffusion within the NP would have occurred at a higher temperature (body temperature ~37°C) than our average imaging temperature of 22°C thereby acting to increase diffusion rates. This phenomenon would explain the higher TraceADC results. In support of this speculation, eigenvalue 1 values from two other studies were less than the results for this study (Table 28), which may also be attributed to diffusivity's dependence on temperature (~ 1.5% per 1°C) (Basser, 1995). While Drew did not report the temperature of the specimens during imaging (Drew et al., 2004), Chiu reported that the temperature of the specimens used in the study could be as high as 16°C at the end of the imaging protocol (Chiu et al., 2001).

Nucleus Pulposus			
	Eigenvalue 1	Eigenvalue 2	Eigenvalue 3
Drew	0.0015	0.00150	0.00150
Chiu	0.00116	0.00111	0.00116
Final Experiment	0.00197	0.00138	0.00097

Table 28. Eigenvalues (mm^2/s) for the NP from Drew *et al.* (Drew et al., 2004), Chiu *et al.* (Chiu et al., 2001), and this study.

The other two eigenvalues reported by Drew *et al.* and Chiu *et al.* did not follow the same trend, as they were larger in some cases than the values from this study. This variation could be attributed to the fact that these studies used thawed cadaveric IVD specimens. From Table 28 it is apparent that the other 2 studies show quite similar diffusion numbers for all of the NP eigenvalues, where anisotropy (non-uniform eigenvalue magnitudes) was definitely observed in this study. Unfortunately, Kealey *et al.* only reported the mean ADC data so anisotropy could not be confirmed in the *in vivo* environment. It may be that in this study, the actual diffusion characteristics of the IVD were maintained due to the use of fresh specimens and the lack of a freeze-thaw cycle employed by Drew *et al.* and Chiu *et al.*

No diffusion studies were identified in the literature where Fractional Anisotropy results were reported for regions within the IVD. This is a strength of this study as the Fractional Anisotropy DTI measure describe the anisotropic tendencies of diffusion within a structure. This may be a value tool, as it may aid in generating inferences regarding AF tear lengths, widths, and orientations.

Discussion

Observation of the significant interaction between the ROI and Slice Plane factors (Figures 46) indicates that for the 2mm core injury, the "on" slices have larger eigenvalue 1 values than the "off" slices. For the NP, this trend changes: the values of the "off" slices become larger than those of the "on" slices. The reason why this interaction is present involves the arrangements of structures within the IVD. Recall that the IVD body is sandwiched between two endplates (Chapter 2, Figure 2), and that the central plane of the IVD falls between the space where the endplates are closest, near the transition zone of the AF. Both the 2mm core and 12GA stab injuries lie in this central plane where the "on" slice is aligned. The NP occupies the middle of the IVD and its superior and inferior borders extend to the top and bottom of the concave portion of the endplates. So while the "on" slice is the optimal plane for data acquisition of the two injuries, either the "on" or "off" slices are adequate for NP DTI data collection. In the case of eigenvalue 1, the NP data is slightly larger in magnitude for the "off" slice than for the "on" slice, but since there is such a difference between the values acquired from these slices for the 2mm core ROI, a significant interaction was detected.

Regarding the general descriptions of the DTI results, the injury data characteristics were due in large part to the nuclear material that had migrated into the injury spaces. It is for this reason that diffusivity along the primary eigenvector, or eigenvalue 1, is expected to be similar between the NP and the 2 injuries. It is the remainder of the injury eigenvalues that should be expected to be significantly different from the corresponding eigenvalues of the NP, as was the case. This expectation is based on the fact that anisotropic diffusion is related to preferential diffusion directions. The smaller the potential route for diffusion, the smaller the eigenvalue 2 and 3 values are compared to eigenvalue 1. On

the other hand, isotropic diffusion results indicate very few restrictions on fluid mobility, therefore, limited differences between eigenvalue 1, 2, and 3 would exist. The diffusion characteristics of the three ROIs can be viewed on Table 29.

	Trace ADC (mm^2/s)	Eigenvalue 1 (mm^2/s)	Eigenvalue 2 (mm^2/s)	Eigenvalue 3 (mm^2/s)	FA (0 to 1)
2mm core	0.000794	0.001815	0.00080	0.00014	0.74
12GA stab	0.000906	0.002095	0.00090	0.00017	0.74
NP	0.001423	0.001919	0.00138	0.00097	0.33

Table 29. DTI means from Experiment 4, for the 2mm core, 12GA stab, and NP. No load.

The close agreement between the eigenvalue 1 values of all three ROIs, also increases the confidence of the injury DTI data. The AF generally exhibits such poor signal that very few studies focus on this region. If the AF region is a focus, such as in this case, there is often inadequate SNR to report results confidently (Drew et al., 2004). While the SNR derived from normal AF data was deemed to be too low for it to be accurate, both the 2mm core and 12GA stab injuries almost doubled the AF in SNR (SNR 13 and 14, respectively).

One unexpected result from the DTI data is the larger diffusion values of the 12GA stab than the 2mm core. Since the 12GA stab injury is a cleft between AF tissues compared to an absence of tissue in the case of the 2mm core injury, it is possible for there to be higher diffusion levels in the more dramatic injury. Likewise, with the puncture, a higher Fractional Anisotropy value would be expected, and this was also not the case. These observations are most likely the result of errors in generating the DTI values due to the presence of air within some of the 2mm core injuries. Because of the size of the 2mm core injury, NP material was not observed to migrate into the entire core injury space immediately following drilling. As parafilm was placed above the anterior beads to ensure that there was no USG infiltrating the injury and influencing the DTI results, an air space could have corrupted the data from the material that did make its way into the

injury. The presence of air, or very low SNR in the injury probably also affected the 12GA stab data, as eigenvalue 1 is larger than that of the NP, which was not expected. A number of methods were explored to introduce donor nuclear material into these injuries, however, the most effective strategy was to wait for nuclear migration into the tear. Loading the IVDs also increased the amount of nuclear material within the injury boundaries.

As is always the case with DTI, a number of confounders can be identified that may have influenced the final data sets for the 2mm core and 12GA stab injuries. The first factor was SNR. Low SNR generates over-estimates of the largest eigenvaluevalue, and under estimates of the smallest. This leads to an over estimate of Fractional Anisotropy (Basser and Pajevic, 2000). The low SNR of the AF also facilitated the development of artifacts - another potential confounder. Finally, distortions introduced by the strong diffusion and EPI gradients were another potential confounder. The geometric distortions introduced at injury locations as well as the NP made it difficult to draw an ROI around the exact feature in the IVD. This most likely introduced some level of partial volume effects that would corrupt the DTI data from the ROI.

In the clinical setting, tears in the AF will most likely not be of the same magnitude as the 2mm core injury generated in this study. Yet, if tears were present, they would be filled with nuclear or extracellular fluid and it would be unlikely for air spaces to be present. Furthermore, if visible to conventional MRI, these tears may have content within the injury borders that will provide good signal sources and thus higher SNR than what was observed in this study. As this particular application of DTI is not focused on the visual recognition of tears, DTI characterization of tears visible to conventional MRI sequences may provide adequate SNR so that data acquired could be used as predictive measures of tear behaviour or other pathological outcomes of the IVD. In addition to concerns regarding SNR impact on DTI data accuracy, image distortions, and thus ROI placement for DTI data acquisition, will likely be a concern in any clinical applications of this technology. Like the combination of SENSE-EPI has reduced the artifacts and distortions related to DTI visualization of tissue, there may be additional technical

advances that reduce this limitation of DTI investigations, thus improving ROI placement for DTI data acquisition.

Until clinical DTI of the IVD is actually piloted, the extent of challenges regarding SNR and distortions related to DTI data acquisition of the IVD will not be known. If these issues prove to be insurmountable in the immediate future, the use of a standard to advance relative diffusion profiles of regions within the IVD, as was done in this study, could provide important clinical knowledge regarding the diffusion characteristics of injuries and other regions in the IVD while not developing firm quantitative descriptions.

5.3 Hypothesis 3

The third and last hypothesis of this study stated that dynamic compression would improve DTI's sensitivity to artificially generated AF tears. Because this study involved qualitative and quantitative components, the results of dynamic loading will be discussed in terms of these two data sets beginning with the Qualitative results.

Qualitative Results:

Though there is a trend that indicates loading improves detection of the 2mm core injury, the results only partially support this hypothesis as the increase in DTI injury visualization (11%) did not reach significance ($p = 0.250$, Wilcoxon Paired-sample test). In the case of the 12GA stab injury, there was a non-significant reduction in DTI injury detection (25%) with compressive loading ($p = 0.172$, Wilcoxon Paired-sample test). On the other hand, clinical MRI visualization of the 2mm core injury increased (67%) significantly ($p = 0.035$, Wilcoxon Paired-sample test), but improvements in 12GA stab visualization (50%) failed to reach significance ($p = 0.500$, Wilcoxon Paired-sample test). There was no change in proton density injury detection with loading for either the 2mm core or the 12GA stab.

Comparison to other literature

Though dynamic loading has been introduced into spinal imaging previously, there are few examples of when compression has been into the actual MRI environment toward improving tear detection. One such study, performed by Saifuddin *et al.,* demonstrated increased sensitivity to HIZ (indicative of radial tears) on axial slices of a conventional MRI protocol (Saifuddin, McSweeney, & Lehovsky, 2003). As in this study, which demonstrated increases in 2mm core detection for DTI, and 2mm core and 12GA stab detection for clinical sequences, the increase in tear sensitivity reported by Saifuddin *et al.* was most likely attributed to three things. First, loading may create an increase in unbound water. Recall that under increasing pressures, the proteoglycans within the IVD lose their ability to bind with water. The unbound water may move into the injury site therefore increasing the signal availability and/or contrast for both conventional MRI and DTI injury detection. The second reason for the increase in injury sensitivity is related to the first. The general increase in unbound water is also attributed to reported increases in T2 relaxation rates for both the NP and AF (Chiu et al., 2001) under load. This would improve the overall visualization of the AF because it would bring the TE of the AF closer to the TE parameters available in most T2W based MRI sequences. Though increases in unbound water and relaxation rates could have played a role in the increases observed in MRI injury sensitivity, migration of the NP into the injury was probably the major factor that resulted in increased tear detection. As radial tears propagate outwards from the NP, any increase in pressure will most likely see the NP attempt to find some way of relieving the additional pressure, resulting in the migration of nuclear material towards or into an existing tear. Any additional nuclear material in a radial tear would definitely increase MRI sensitivity, by either conventional or DTI sequences.

As described in Chapter 2, the AF structure has evolved to contain the tremendous pressure generated by the NP. Though physiological loading may result in some NP migration into the AF, once additional loads are removed, the tensile force and pressure acting in the AF may force the migrated nuclear material back towards the NP. Of course, this is one issue that must be addressed prior to the clinical implementation of dynamic MRI as the migration of nuclear material out of the NP would destabilize the

mechanical system of the IVD. If the nuclear material failed to return to the NP, dynamic loading related to improved AF tear detection may have more detrimental effects to IVD health than benefits. While the magnitude of loading, given a range within normal daily activities, would not be the primary concern regarding clinical dynamic MRI, the timing and loading scheme (creep, step, etc) could have additive affects to any injury even at low loads (Adams et al., 2000).

Discussion

This hypothesis was initially generated based on the assumption that unloaded DTI visualization of the artificial tears would not be as sensitive as this study indicates. Because of this, it was simply impossible for dynamic loading to initiate any significant improvements to 2mm core visualization as DTI's unloaded detection rates were too high. Yet, improvements in DTI 2mm core injury visualization with loading was most likely due to the additional pressure in the NP causing the migration of nuclear material into the large injury.

Overall, the reduction in DTI 12GA stab injury visualization given dynamic loading was not expected as it was anticipated that nuclear material would migrate into the injury space and provide a strong signal source. A possible explanation for this observation is related to the AF's well known alternating fibre pattern that allows it to self-seal if ever there is a sufficiently large break or tear of the lamellae. This behaviour is analogous to a self-sealing tire that will not lose air pressure if punctured by a nail. Though DTI was able to detect a certain percentage of the stab wounds under no loading conditions, the additional increase in IVD pressure may have caused the AF to seal the injury.

A potential confounder for dynamic loading results was the position of injury plane during imaging. As the DTI sequence preceded the clinical and proton density scans, this confounder pertains more to the visualization of injury on these sequences following DTI. Increases were observed in the detection of both clinical and proton density slices, but the optimal slice planes generated for DTI imaging might have changed position over the entire loading protocol. As the total imaging time was approximately 30 minutes

long, displacement of the IVD tissue during imaging was expected. To combat this situation, the initial loading was taken to a steady state point (following 3 minutes of loading about the set-point) so that any initial displacement would take place prior to the beginning of the imaging protocol. With the initial movement given a chance to dissipate, the imaging protocol was started. Depending on the amount of creep over the 30 minute period, the absolute slice location for each MRI sequence may have varied but examination of the images taken during dynamic imaging show the same portion of demarcation beads, and similar clinical and NP features between each of the 4 axial sequences (Appendix E). For this reason, any residual creep during the loading protocol is of concern, but most likely would not have significantly altered the qualitative results. Measurements of linear displacement were included in the experimental protocol, however, significant bending of the specimens rendered the creep information suspect.

Quantitative Results

Under load conditions, a significant interaction between the ROI and Slice Plane factors was introduced into the TraceADC and eigenvalue 3 DTI measures (Figures 47 and 48). Overall, there continued to be a significant difference between the DTI maps of the two injuries and the NP under load conditions, and eigenvalue 1 was now found to be significantly different between the 2mm core injury and NP. This hypothesis was supported by the results based on the increase of DTI measures that significantly varied between the injuries and the NP. The hypothesis was further supported through the quantitative DTI measure results for each ROI, which described relative diffusion properties that reflected the size and contents of the ROI.

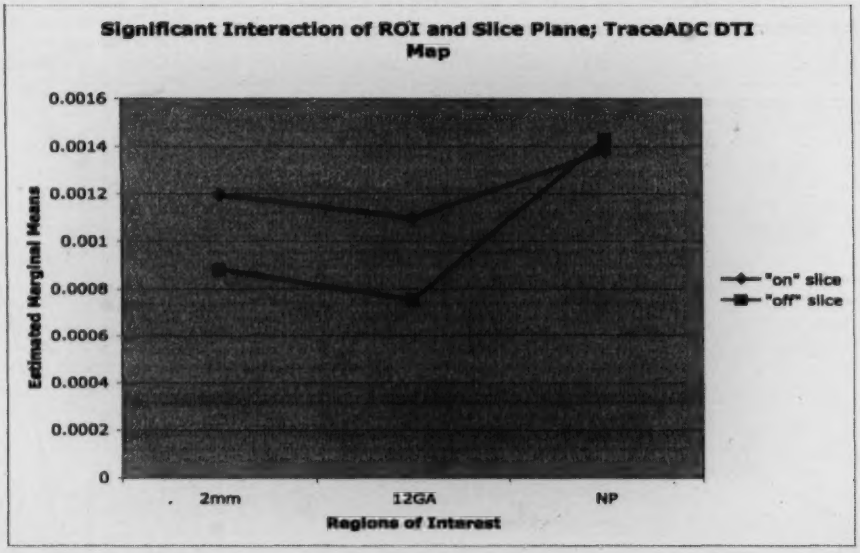

Figure 47. Significant interaction between ROI and Slice Plane for TraceADC data of injuries and NP during compressive loading.

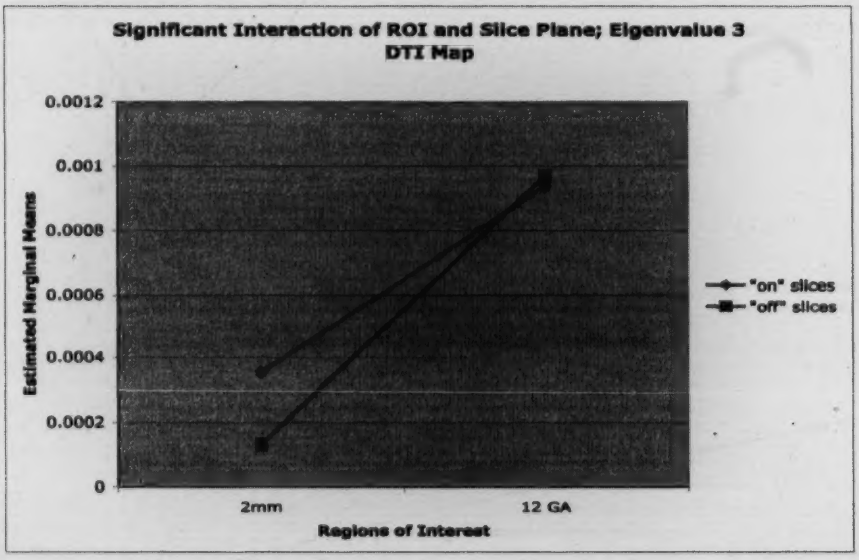

Figure 48. Significant interaction between ROI and Slice Plane for the eigenvalue 3 for 2mm core and NP ROIs during compressive loading.

Comparison to other literature

Once again returning to the quantitative comparison between the results from this study and the results from Chiu *et al.*, the application of loading saw small changes in eigenvaluevalues for this study, while increases in the eigenvaluevalues were reported from Chiu *et al.*'s NP ROIs (Table 30). A large increase in diffusion as a result of loading would seem to be the most intuitive, but this was not the case. There are a few potential reasons for this observation. First, the loading protocols of this study and Chiu *et al.* were different. As in the final experiment of this thesis, Chiu *et al.* used a step load, however, the load magnitude was 350kPa (Chiu et al., 2001) compared to the ~250kPa used in this study. It also took approximately 10 minutes to begin the imaging protocol for this experiment as it was essential that the injury slice position was accurately determined, whereas Chiu *et al.* were able to begin diffusion measurements at least 5 minutes following loading because additional imaging was not required to position the mid-sagittal slice plane used for diffusion MRI. The advantages of acquiring diffusion information early in the loading cycle was well explained by Chiu; diffusion had not yet approached an equilibrium and was therefore more dynamic (Chiu et al., 2001). Given the long loading period prior to diffusion imaging in this study, the relative diffusion equilibrium within the NP could have reestablished itself from any perturbations initially caused by loading. The larger load may have also initiated more diffusion within the NPs of Chiu *et al.*'s specimens, whereas the load in this study may have been insufficient to alter the diffusion equilibrium within the NP. These factors may be the reasons behind the larger changes in Chiu *et al.'s* eigenvaluevalues compared to the minute variations in the changes seen in the eigenvaluevalues from this study.

Nucleus Pulposus	[illegible]	[illegible]	[illegible]
Chiu	0.00116	0.00111	0.00116
Final Experiment	0.00192	0.00138	0.00097
[illegible]			
Chiu	0.00124	0.00126	0.00119
Final Experiment	0.00190	0.00137	0.00096

Table 30. Eigenvalues (mm^2/s) for the NP from Chiu *et al.* (Chiu et al., 2001). Dynamic load conditions.

Different ROI locations may have also contributed to the observed difference in diffusion responses to load. Because of the mid-sagittal slice plane used by Chiu *et al.*, there was a limit to the coverage of the NP that could be achieved with ROIs. Therefore, three small boxes in the central portion of mid-sagittal slices were used to generate the eigenvaluevalues for Chiu *et al.*'s study (Chiu et al., 2001), while the entire axial body of the NP was traced and used as the ROI in this study. Chiu *et al.*'s ROIs covered the central portion of the NP, between the endplates, and this area is most likely to experience increased diffusion with loading, however, it is not known how diffusion changes near the transition layers between the NP and AF, or what happens at the periphery of the NP, so the ROI used in this study was generated to also include these areas. At a latter date, more specific ROIs can be used to generate data from this study, which can then be compared to answer some of these questions.

Finally, though the NP loading results from this experiment are counter intuitive, the use of fresh specimens in this study and thawed specimens by Chiu *et al.*, may provide an explanation. For example, factors related to sample preparation, such as temperature and freeze-thaw cycle, could affect the constitution of the NP matrix or the behaviour of proteogylcan/water binding (Bass et al., 1997).

Discussion

Dynamic loading introduced significant interactions between the ROI and Slice Plane factors for the TraceADC and eigenvalue 3 DTI measures. Similar to the significant interaction indicated in the second hypothesis, observation of the interactions (Figures 45 and 46) indicates that for the injuries, the "on" slices have larger TraceADC and eigenvalue 3 values than the "off" slices. For the NP, this trend changes and the values from the "off" slices become larger than that of the "on" slices. The presence of this interaction involves the arrangements of the injuries and NP within the IVD. Because the "on" slice is usually situated between two endplates in the central part of the IVD (Chapter 2, Figure 2), this is the optimal plane for data acquisition of the two injuries, while either the "on" or "off" slices are adequate for NP DTI data collection. In the case of eigenvalue 1, the NP data are slightly larger on the "off" slice than the "on" slice, but

since there is such a difference between the values acquired from these slices for the two injuries, a significant interaction was detected.

One additional explanation that was not noted when describing the potential origin of the early significant interaction in Hypothesis 2, takes into consideration that the "on" injury slice was not always in the very central zone of the IVD. In some cases the injuries were generated just below or above one of the endplates, which placed the occasional "off" slice in the central zone of the IVD. Because no matter what the actual location of the injuries were, they would be partially filled with nuclear material, so the "on" slices would always exhibit DTI injury data that was larger in magnitude than the "off" slice data. The NP on the other hand, could have been better positioned within the IVD on an "off" slice that placed the ROI directly between the two endplates, resulting in higher TraceADC and eigenvalue 3 values than the "on" slice. The injury plane often not being aligned with the central plane of the IVD could be a reason why the "off" slices from the NP were slightly larger than the "on" slices, resulting in an interaction between Slice Plane and ROI being detected.

Regarding the general trends of the ROIs, the diffusion characteristics of the two injuries in the loaded case were much closer to what would be expected than what was originally characterized in the unloaded case and their DTI characteristics remained statistically different from the NP. This observation supports Hypothesis 3, as dynamic loading seems to have improved the sensitivity of DTI to the actual diffusion characteristics of the two injuries.

Overall, the NP continues to have larger TraceADC, eigenvalue 2 and eigenvalue 3 values, but the injuries dominate the eigenvalue 1 and Fractional Anisotropy measures (Table 31). This is to be expected given that as the pressure within the NP increases due to loading, nuclear material should try to escape to lower pressure zones. The easiest conduits to achieve this would be the 2 injuries. Since the injury, and thus diffusion, is primarily in one direction, the average Fractional Anisotropy values continue to be greater within the injuries than in the NP. The TraceADC, and eigenvaluevalues of the

2mm core data surpasses that of 12GA, as the 2mm core is a larger injury and thus it should have more isotropic diffusion properties. Fractional anisotropy is also larger for the 12GA stab than the 2mm core injury under loading conditions as what would be expected for an injury with smaller boundaries. This improved quantitative DTI data is likely a result of the compressive loading, which most likely filled the injuries with nuclear material, displacing any airspace, and thus providing better estimates for the diffusion characteristics of the injuries.

	Trace ADC (mm^2/s)	Eigenvalue (mm^2/s)	Eigenvalue (mm^2/s)	Eigenvalue (mm^2/s)	Fractional anisotropy (0 to 1)
2mm core with load	0.001042	0.002173	0.000995	0.000245	0.72
12GA stab with load	0.000957	0.002103	0.000926	0.000174	0.75
NP with load	0.001407	0.001902	0.001373	0.000956	0.33

Table 31. DTI means from Experiment 4, for the 2mm core, 12GA stab, and NP. Dynamic loading.

A potential confounder of the quantitative dynamic DTI results involves DTI's data quality given low SNR. Even though the results in the loaded case seemed to be more logical, there was actually an 8% drop in SNR for each of the 2mm core, 12GA stab, and NP ROIs during loading. This observation could be due to a loss in water content because of the longer loading period (Drew et al., 2004). Because in the clinical environment such specific slice plane selection would not be required, a shorter loading protocol could be used if the reduction in SNR is indeed related to a loss of water content within the material occupying the injury boundaries. On the other hand, the presence of bulk water may have actually caused the SNR reductions. Though improved visualization of injury occurred, an overall reduction in magnetization, and thus signal strength could have occurred due to pooling fluid (Hashemi, Ray H., M.D., Bradley, & Lisanti, Christopher J., M.D., 2003). Because the tears in this injury protocol were acute, there could have been higher water content present, whereas the material within a tear that is visible to

clinical MRI may actually be associated with older injuries that do not have as high water contents. This may reduce potential bulk water effects in the clinical acquisition of sufficient SNR for accurate quantitative DTI measurements of AF tears. Whether the loss in SNR was caused by a decrease or increase of water content, hardware and sequence improvements are required before DTI characterization of AF tears reaches a level were results are confidently reported in either experimental or clinical conditions.

5.4 Strengths and weaknesses

Strengths:

This study was the first to evaluate if qualitative observation of AF tears is improved by observation of DTI maps in comparison to injury visualization with conventional MRI sequences using a clinical MRI unit (1.5 T). Additionally, quantitative DTI values were used to characterize the diffusion properties of these injuries compared to those in the NP.

The final experiment of this study was generated to best observe the differences between conventional and dynamic MRI AF tear detection. To accomplish this goal, multiple early experiments were conducted to ensure equivalent imaging circumstances between the two sequences. These circumstances included equivalent geometric parameters and slice location, as well as a range of injuries that were aligned on a single slice plane shared by the two sequences. As a result, any differences or similarities between the results for the DTI and clinical sequences were due almost exclusively to their different abilities to detect artificial radial tears in the AF.

Repeating the imaging protocol under dynamic loading conditions introduced a functional component to the comparison of DTI and conventional MRI sensitivities to artificial tears in the AF. Dynamic MRI has been previously used to improve clinical MRI AF tear detection and to measure changes in diffusion MRI measures of the NP, but this is the first study to specifically investigate the impact of dynamic MRI on both the qualitative visualization and quantitative characterization of AF tears using DTI. Further,

the quantitative DTI data acquired were more representative of what the actual *in vivo* loading environment would be like for an injured IVD, allowing a more confident reporting of the quantitative results.

Finally, many studies use sagittal slice planes for the detection of IVD abnormalities, but this limits the potential for injury boundaries to be identified. The axial slice plane used in this study provided the best opportunity for visualization of the artificial injuries, NP and the general features of the IVD. The axial slice plane also allowed for the exact slice placement on the injury plane, increasing the confidence when qualitatively scoring injury detection. The increased opportunity for injury boundary visualization also allowed for larger ROIs to be made, generating the best possible quantitative approximations of the injuries and NP diffusion characteristics.

Weaknesses:

The main weakness of this study was the low SNR from the AF and AF injuries. It has already been well described how DTI is extremely susceptible to low SNR resulting in distortion, artifacts, and inaccurate DTI values (Basser and Pajevic, 2000, Le Bihan et al., 2006). Though EPI and SENSE were utilized, similar SNR result were found as in previous studies (Drew et al., 2004) leading ultimately to the exclusion of the normal AF DTI data. The DTI data from the injuries did have greater SNR levels, but not at levels as robust as the NP. A number of materials incorporated into the study (USG, beads), further added to the presence of artifacts within the DTI images that may have contributed to errors in the ROI generation, and thus DTI averages.

Despite the optimization of DTI maps for injury visualization, the presence of artifacts near the injury location may have caused inaccurate observations by observers. Also, any potential bias that preferentially increased DTI visualization rates could have reduced the rate of injury visualization for the other sequences. While the influence of artifacts on injury scoring was difficult to control, employing blinding techniques could have reduced any bias introduced into the injury visualization scoring.

The low number of specimens used in this study is also problematic. While DTI detection was consistently greater, a small difference in injury observations could have affected whether there was significant difference detected or not. Because the ability to have a significant trend was dependent on a small number of observation, the lack or detection of a significant difference may not have been due to a true difference in clinical MRI and DTI procedures.

The use of porcine spine segments introduced an obvious weakness into the study. While animal models are extensively used in clinical research of the lumbar spine, the AF diffusion properties of human IVDs are most likely different than those of quadrupeds. The size of injury generated in this study was also most likely larger than what would be expected in *in vivo* cases. Prior knowledge of injury dimensions additionally allowed for the in-plane resolution, slice thickness, and inter-slice gap of the MRI sequences used in this study to be reduced precisely from their clinical levels to best capture the artificial injuries. This level of precision is not realistic in clinical evaluations. Given these factors, the DTI results from this study should not be taken as representative of what could be repeatedly detected in naturally occurring tears in the human AF.

The size of the *in vitro* animal model allowed for the use of a 8-channel head coil. This specific coil is what made the implementation of SENSE-EPI DTI possible in this study. Because the loading rig was designed so that the spine segments could be imaged in this specific head coil, any future human *in vivo* studies must readapt the basic DTI sequences usually used for brain imaging for IVD DTI. This would mean that this entire study would have to be repeated using a spinal array, or body coil with SENSE capabilities.

5.5 Clinical Potential / Research Significance

This study shows that the use of DTI has potential for not only the visualization of tears in the AF, but also that DTI has the ability to characterize the diffusion properties of structures and injuries in the IVD. Visualization of the artificial injuries was achieved at higher rates than clinical MRI while under loading conditions, additional improvements to the quantitative DTI data were seen. It is for the latter reason that DTI may provide a

new tool for LBP research. By providing the characterization of diffusion properties within the IVD, a sense of how diffusion changes between the IVD structures, and how diffusion changes within injuries, can begin to be described. These observations conspire to give potential to DTI as a viable tool in the ongoing clinical and academic study of the IVD.

Despite favorable DTI injury observation results, there are a number of factors that preclude the immediate use of this technique in clinical settings. The presence of artifacts and sporadic signal from the AF is what motivated the optimization of the DTI maps. Without this processing, only the clearest of 2mm core and 12GA stab injuries could be confidently detected. Furthermore, the presence of erroneous signal sources could be misinterpreted as clinical findings. With that being said, the dominance of DTI detection of injury compared to conventional MRI detection, especially from the "off" injury slice plane, suggests that when DTI sequences become more robust to artifacts, clinical implementation of DTI tear detection will follow shortly.

Though the DTI protocol is presently available for clinical use, the MRI unit used in this study lacked the ability to generate optimized DTI maps. For this reason another workstation would have to be used to generate the basic DTI maps. Depending on the quality of visualization, SI thresholding could be initiated for improved DTI injury visualization, though this process was extremely time consuming. A single iteration of the DTI map optimization process could take up to 5 minutes, and several iterations were sometimes required to reach an optimum injury visualization level. In the clinical environment, a certain amount of time is allotted per MRI investigation, and as it stands, the DTI technique described in this thesis is outside of this time window.

A final note regarding the clinical significance of this study; Though conventional MRI was found to not be as sensitive to artificial AF injuries, dynamic loading increased the detection of injuries by a significant amount. This finding must be further studied to confirm that loading does not exacerbate existing injuries before the recommendation for clinical dynamic MRI can be made.

Chapter 5 references

Adams, M.A., Freeman, B.J., Morrison, H.P., Nelson, I.W., Dolan, P., 2000. Mechanical initiation of intervertebral disc degeneration. Spine. 2513, 1625-1636.

Aprill, C., Bogduk, N., 1992. High-intensity zone: a diagnostic sign of painful lumbar disc on magnetic resonance imaging. Br. J. Radiol. 65773, 361-369.

Bass, E.C., Duncan, N.A., Hariharan, J.S., Dusick, J., Bueff, H.U., Lotz, J.C., 1997. Frozen storage affects the compressive creep behavior of the porcine intervertebral disc. Spine. 2224, 2867-2876.

Basser, P.J., 1995. Inferring microstructural features and the physiological state of tissues from diffusion-weighted images. NMR Biomed. 87-8, 333-344.

Basser, P.J., Pajevic, S., 2000. Statistical artifacts in diffusion tensor MRI (DT-MRI) caused by background noise. Magn. Reson. Med. 441, 41-50.

Chiu, E.J., Newitt, D.C., Segal, M.R., Hu, S.S., Lotz, J.C., Majumdar, S., 2001. Magnetic resonance imaging measurement of relaxation and water diffusion in the human lumbar intervertebral disc under compression in vitro. Spine. 2619, E437-44.

Drew, S.C., Silva, P., Crozier, S., Pearcy, M.J., 2004. A diffusion and T2 relaxation MRI study of the ovine lumbar intervertebral disc under compression in vitro. Phys. Med. Biol. 4916, 3585-3592.

Gu, W.Y., Mao, X.G., Foster, R.J., Weidenbaum, M., Mow, V.C., Rawlins, B.A., 1999. The anisotropic hydraulic permeability of human lumbar anulus fibrosus. Influence of age, degeneration, direction, and water content. Spine. 2423, 2449-2455.

Guyer, R.D., Ohnmeiss, D.D., NASS, 2003. Lumbar discography. Spine J. 33 Suppl, 11S-27S.

Hashemi, Ray H., M.D., Bradley, W.G.J., Lisanti, Christopher J., M.D., 2003. MRI the basics, second ed. , Lippincott Williams & Wilkins, Philaderlphia USA.

Kakitsubata, Y., Theodorou, D.J., Theodorou, S.J., Trudell, D., Clopton, P.L., Donich, A.S., Lektrakul, N., Resnick, D., 2003. Magnetic resonance discography in cadavers: tears of the annulus fibrosus. Clin. Orthop. Relat. Res. (407)407, 228-240.

Kealey, S.M., Aho, T., Delong, D., Barboriak, D.P., Provenzale, J.M., Eastwood, J.D., 2005. Assessment of apparent diffusion coefficient in normal and degenerated intervertebral lumbar disks: initial experience. Radiology. 2352, 569-574.

Kerttula, L., Kurunlahti, M., Jauhiainen, J., Koivula, A., Oikarinen, J., Tervonen, O., 2001. Apparent diffusion coefficients and T2 relaxation time measurements to evaluate disc degeneration. A quantitative MR study of young patients with previous vertebral fracture. Acta Radiol. 426, 585-591.

Lander, P.H., 2005. Lumbar discography: current concepts and controversies. Semin. Ultrasound CT MR. 262, 81-88.

Le Bihan, D., Poupon, C., Amadon, A., Lethimonnier, F., 2006. Artifacts and pitfalls in diffusion MRI. J. Magn. Reson. Imaging. 243, 478-488.

Niinimaki, J., Ruohonen, J., Silfverhuth, M., Lappalainen, A., Kaapa, E., Tervonen, O., 2007. Quantitative Magnetic Resonance Imaging of Experimentally Injured Porcine Intervertebral Disc. Acta Radiol. 486, 643-649.

Saifuddin, A., McSweeney, E., Lehovsky, J., 2003. Development of lumbar high intensity zone on axial loaded magnetic resonance imaging. Spine. 2821, E449-51; discussion E451-2.

Schellhas, K.P., Pollei, S.R., Gundry, C.R., Heithoff, K.B., 1996. Lumbar disc high-intensity zone. Correlation of magnetic resonance imaging and discography. Spine. 211, 79-86.

Chapter 6: Conclusion

Overview

To summarize, this thesis has shown that DTI can be used to detect a known IVD injury. The remaining three sections of this chapter prioritize future work, highlight the relevance of this research towards new knowledge regarding LBP, and then finally describe directions for the future of this research.

6.1 Hypothesis One

The first hypothesis of this thesis stated that DTI would enable the visualization of artificially generated AF tears of magnitudes inconspicuous to conventional MRI detection. The results generated in this thesis supported this hypothesis directly; the detection sensitivity of DTI to artificially generated tears in the AF was higher than conventional or "clinical" MRI. Furthermore, DTI's threshold of injury visualization is more than that of conventional sequences. This result is even more significant when both the "on'' and "off" slices were used for visualization.

Despite the support of the first hypothesis, clinical implementation of DTI for use in lumbar spine imaging will require improvements in MRI AF signal acquisition. In addition, further improvements in DTI sequences are required to limit the presence of artifacts that may confound clinical findings. Clinical implementation would also require improvements in DTI image processing so that diagnosis can be generated in a clinically acceptable timeframe.

Though DTI may not yet be suited for the diagnostic detection of AF tears, the strength of injury visualization demonstrated in this research makes a strong case for continued development of this technique in the study of LBP.

6.2 Hypothesis Two

The second hypothesis of this master's research was that DTI AF tear measurements would be significantly different from that of the NP. This was supported as DTI measurements of artificially generated injuries could be statistically differentiated from the NP. Yet more importantly, the comparison of DTI measures described the diffusion characteristics representative of what would be expected given each ROI. This was especially true under loading conditions.

This quantitative application of DTI is better suited for research purposes than clinical applications, but as mentioned previously, improvements in IVD signal acquisition and DTI protocols are still required to increase the confidence in quantitative IVD DTI results. Because accurate DTI results are highly dependent on a minimum SNR, the suggested improvements in DTI imaging of the IVD would provide important improvements in signal magnitude allowing for the development of quantitative diffusion profiles of regions within IVDs. At the moment, quantitative DTI data, save data from the NP, is not useful as a stand-alone technique to identify IVD injury. These DTI results also demonstrate that by using two regions within the IVD, relative diffusion profiles can be generated.

6.3 Hypothesis Three

The third hypothesis of this thesis, namely that dynamic compression would improve DTI's sensitivity to artificial AF tears, was not supported or refuted directly by the data collected. Dynamic MRI improved the ability of conventional and DTI imaging to identify the larger 2mm core injury. With respect to the smaller, 12GA injury, dynamic MRI increased injury identification in conventional MRI but had the opposite effect on DTI imaging. The time at which these sequences were implemented during the loading protocol is believed to have had a possible impact on the effectiveness of dynamic loading in further improving injury detection.

The results of this research support the future clinical implementation of dynamic loading protocols to increase MRI sensitivity to tears in the IVD, however, if dynamic loading is to be introduced clinically, steps must be taken to ensure visualization is being improved and not hindered. These steps would include the evaluation of a variety of loading protocols in order to optimize loading schemes and MRI acquisition timing to best elicit SI increases within AF tears. Further, the evaluation of the affect of dynamic loading on IVD pathology is required.

6.4 Thesis recommendation

This study has shown that DTI's tremendous ability to not only generate contrast between tissues, but to also quantitatively characterize what is being seen can be used to both visualize and describe artificial tears in the AF. Specifically, DTI qualitative detection of AF tears was achieved and found to surpass the capabilities of the conventional MRI sequences used in this study. Further, the application of dynamic loading complimented DTI's ability to characterize diffusion properties of regions within the IVD. Because researchers of LBP have very few techniques that enable the in depth *in vivo* study of the IVD, continued research towards a DTI – Dynamic MRI protocol that can confidently (adequate SNR, few artifacts) be used as a LBP research tool is recommended. Given the results from the proton density sequence, adaptions to further reduce the TE of existing lumbar spine proton density protocols (TE ~ 15msec) to reflect the TE used in this study (TE 9.7msec) is also recommended for clinical AF tear detection.

A reduced focus on further adaptations of existing clinical IVD MRI techniques is also recommended for a number of reasons. First, clinical IVD MRI is used widely and has already experienced IVD specific optimizations, but its inability to consistently visualize AF tears limits its use in the continued study of AF tears' relationship to LBP. Second, though dynamic MRI significantly improved clinical MRI sensitivity to AF tears, the increases in visualization still did not surpass unloaded DTI visualization. Finally, the overall percentage of clinical MRI visualizations of the artificial tears was very similar to rates of proton density injury visualization, despite this sequences inability to generate "off" slices.

Overall, the basic uses of MRI technology are the detection of abnormalities and the generation of knowledge regarding *in vivo* processes in the body. Of the three types of sequences evaluated in this study, only DTI fulfills these requirements for AF tears, and of the remaining MRI sequence types, proton density outperformed conventional MRI.

6.5 Thesis relevance

This work supports the view that DTI sequences have the potential to provide opportunities for identification of annular tears and therefore, provide a potential tool toward understanding the relation between IVD tears and LBP. The quantitative description of AF tears may identify fluid diffusion characteristics that are predictive of increased AF tear migration, degeneration, or even LBP. The presence of tears themselves may not be a significant indicator of LBP, but there may be a link within the diffusion properties of the tear. Whether that link is indicative to acuteness of injury, or just the mechanical properties of the material within the tear, conventional MRI measures such as SI, IVD height, bulge and HIZs are reaching a limit as to what they can tell us about the IVD. This study illustrates the continued potential for MRI to yield new information regarding the IVD and LBP. Greater sensitivity to AF tears, while not yet at the point of clinical implementation, can play a role in monitoring the effects of experimental interventions or the progression of injury in an animal model.

6.6 Directions for the future

Continued research is necessary to reduce the presence of artifacts and distortions within DTI visualization of the AF. This can be accomplished, in part by increasing the SNR of the AF through the specific optimization of DTI parameters for IVD imaging. Many of the factors contributing to the artifacts within the DTI maps were also due to experimental materials. Changes in the experimental materials and/or design (USG, beads, loading rig, animal MRI unit, etc) may improve the quality of both DTI visualization and DTI data. Because these improvements are not imminent, it is important to acknowledge the proton density sequence's ability to visualize both this study's injuries at rates higher than the clinical sequences. Adaptations to existing forms of this sequence should be explored for immediate use in clinical AF tear detection.

Chapter 6 references

There are no references for this chapter.

Appendix A: Ethics Protocols

APPLICATION TO USE ANIMALS FOR RESEARCH OR TEACHING
FACULTY OF AGRICULTURE, FORESTRY AND HOME ECONOMICS

Amendment to Protocol/Annual Renewal/Annual Report
Date: May 24, 2005
Protocol Number: 2005-40B
Investigator Information

	Name	Position	Department	E-mail address	Telephone
Principal Investigator	Greg Kawchuk	Assistant Professor	Physical therapy	greg.kawchuk@ualberta.ca	(780)492-6891
Coinvestigator	George Foxcroft	Professor	AFNS	george.foxcroft@ualberta.ca	(780)492-7661
Coinvestigator	Jennifer Patterson	Research Coordinator	AFNS	Jennifer.patterson@ualberta.ca	(780) 439-4808
Emergency Contact	Jennifer Patterson	Research Coordinator	AFNS	Jennifer.patterson@ualberta.ca	(780) 439-4808
Unit Manager	Jay Willis	Swine Unit Manager	Swine Unit	jay.willis@ualberta.ca	(780) 492-7688

Protocol Information

Project Title (from Section 2 of original protocol)	A comparison of breeding at the first or second post-weaning estrus to determine the effect on ovarian follicular development and associated fertility in first parity sows.
Amendment(s):	(Identify the sections from the original protocol to be amended by section number and title: (e.g. "1. Investigators", "3. Staff", "4. Animals", "7a. Project Description", "7b. Standard Operating Procedures", "9. Samples", "10. Agents", etc.):
	3. STAFF QUALIFICATIONS AND EXPERIENCE WORKING WITH ANIMALS Spines will be removed by either the PI (Greg Kawchuk) or a graduate student trained by the PI. The Pi has removed hundreds of spines between studies at the U of A, U of Calgary and Goteborg University. 7.a) Project Description: D28 Data: In addition to the data collected at d28, after euthanasia, spines will be harvested *en block*. That is, a saw will be used to transect thoracolumbar and lumbosacral regions and the lumbar spine removed as a whole. These spines will then be used for magnetic resonance imaging studies to characterize the diffusion properties of intervertebral discs.
Annual Progress Report (if renewing a protocol)	(Summarize progress to date; identify number of animals used [including the number "used" unintentionally in wildlife field studies]; number of cases of unexpected morbidity/mortality; precautions and recommendations for the future)
	Not applicable

Original Protocol:	Submission Date: April 28, 2005	Commencement Date: May 20, 2005	Conclusion Date: Dec 2005
Prior amendments/renewals:	Date: n/a	Date: n/a	Date: n/a

UNIT MANAGER'S COMMENTS (must be included on all amendments)

I wholeheartedly approve of any opportunity to make more extensive use of animals euthanized for research.
Jay Willis, SRTC Manager

PRINCIPAL INVESTIGATOR'S COMMENTS (must be included on all amendments)

Post-mortem removal of spines in this study further maximizes the use of these animals and may lead to future collaborations between researchers regarding the effect of pregnancy on spinal mechanics.

FAPWC Review: Comments and Conditions

(Response to FAPWC review.)

DECLARATION

In submitting this application, the investigators accept the following declaration:

i. All manipulations having the potential to cause pain and discomfort will, wherever possible, be refined in technique and reduced in numbers, to achieve the desired results with a minimum degree of discomfort to the animal.

ii. All animal manipulations will be carried out by trained and competent personnel, using only approved techniques. I have prepared and/or reviewed this application in its entirety and I accept personal responsibility as Principal Investigator for all animal manipulations involved in the project by myself and staff.

iii. I will ensure that all animals used in this research project will be cared for in accordance with the guidelines of the University Animal Policy and Welfare Committee, UAPWC; Faculty of Agriculture, Forestry and Home Economics, FAPWC; guidelines and policies of the Canadian Council on Animal Care, and requirements of legislation. I accept responsibility for keeping current with this information.

iv. I will continue to seek alternative methods which do not involved the use of living animals or which enable comparable results to be achieved by use of a species that is lower in the phylogenetic order or with a less developed central nervous system.

v. I will notify the FAPWC of any revisions to this protocol.

Faculty of
Agriculture, Forestry
and Home Economics

Faculty Animal Policy and Welfare Committee

20 June 2006

Dr. Greg Kawchuk
Canada Research Chair in Spinal Function
Assistant Professor, Faculty of Rehabilitation Medicine
University of Alberta

RE: Obtaining Animal Tissues

Dr. Kawchuk,

Thank you for your letter requesting cadaveric spines from regularly euthanized swine at the SRTC. As this is a category "A" procedure, you may obtain any amount of tissue as required for your research and FAPWC does not need to record the amount, protocol numbers or investigators that correspond to the tissue harvest. Please follow up with Jay Willis, Unit Manager, SRTC, to confirm what records he might need to keep or report.

Any need to obtain spines that requires that animals be euthanized specifically for this purpose will require a completed and approved animal ethics form submitted to FAPWC with the form available at http://www.fapwc.afhe.ualberta.ca.

The Committee has no concerns regarding this research and there is no expiry to this letter. If you have any questions, please contact me at 492-3990 or via email doug.korver@ualberta.ca if I can be of further assistance.

Sincerely,

Doug Korver

Doug Korver,
Chair, FAPWC

cc: Jay Willis, Unit Manger, SRTC
Loren Kline, Chair, HSAPWC

UNIVERSITY OF ALBERTA IN VIVO NMR CENTRE CONTINUING RESEARCH PROJECT

1. Project Title:
Magnetic resonance imaging study to characterize the diffusion properties of intervertebral discs (IVDs) with an inner annulus injury.

2. Name, Position and Department of Principal Investigator:
Dr. Greg Kawchuk, Assistant Professor Faculty of Rehabilitation Medicine (UofA), Adjunct Biomedical Engineering

3. Names, Positions and Departments of Co-Investigators:
Jason Pearman, Candidate – M.Sc. Biomedical Engineering, Department of Biomedical Engineering

Funding Source:
NSERC

Study Objectives and Protocol Summary:

OBJECTIVE: This project is to quantify the diffusion properties of intervertebral discs (IVD) during simulated weight bearing conditions before and after the initiation of an inner annulus injury.

PROTOCOL SUMMARY:

i) Porcine spines are harvested *en block*, that is, a saw will be used to transect thoracolumbar and lumbosacral regions and the lumbar spine removed as a whole.

ii) Once harvested, spine segments will be stored at Corbett Hall, refrigerated at approximately -20 C until used in study.

iii) Before use, a segment will be thawed for 24hrs, and a plastic catheter inserted into the inner annulus to permit injection of compressed nitrogen gas.

iv) The spine segment will be placed in a garbage bag filled with ultrasound contrast gel, which will then be placed in two additional garbage bags.

v) The triple bagged spine segment immersed in ultrasound gel will then be placed in a specially constructed rig which will allow axial compression of the specimen while it is positioned in the 1.5T Magnet to conduct diffusion MRI studies. This rig has undergone testing and prior use at the Seaman Family MRI facility in Calgary.

vi) The plastic catheter will be connected to plastic tubing which will be run into the MR control room. This will permit injection of compressed air into the sample without disturbing the placement of the specimen.

vii) Using known parameters, the IVD of interest will be imaged in a loaded and unloaded state. The IVD will then be injected with compressed nitrogen to create an annular injury and the IVD re-imaged in the loaded and unloaded state. Once imaging has been completed, the specimen will be sectioned and inspected visually in the NMR Centre's Wet Lab, followed by the appropriate disposal of the garbage bags, ultrasound gel, and biological material.

Type and number of animals:
Cadaveric swine specimens (~20)

Which magnet will be used?
1.5T

Planned Completion Date:
2007

Appendix B: PTHER531 Directed Study Final Report

Characterization of Water Diffusion in Intervertebral Discs; Injury Generation Method

Submitted to: Greg N Kawchuk

Submitted by: Jason A Pearman

November 4, 2006

Characterization of Water Diffusion in Intervertebral Discs; Injury Generation Method

Jason A. Pearman B.Sc. (ENG BIO), Greg N. Kawchuk PhD
Rm. 2-28 Corbett Hall, University of Alberta

Introduction

Intervertebral disc (IVD) injury is considered to be a significant cause of acute and chronic back pain. Current magnetic resonance imaging (MRI) protocols have been unable to consistently visualize sites of IVD injury, and thus, diagnose potential causes of pain. My research will attempt to visualize precursors of injury by identifying alterations in water diffusion patterns within IVDs using MRI.

In order to achieve the end goal of improved IVD injury visualization using MRI, two sub topics required initial investigation: 1. determining a highly user defined injury generation method for animal and cadaver models and 2. exploring physiological loading parameters for dynamic imaging, so that functional changes in the injured IVD can be visualized. The focus of the work presented here is on topic 1.

Attempts to reproduce IVD injuries through various models have met with difficulties in controlling injury magnitude and location, in addition to minimizing damage from external access to injury site. The aim of this study was to validate Oliphant *et al's* injury method as an accurate and user-defined method of generating Inner Disc Disruption (IDD) injuries of various magnitudes.

Methods

IDD injuries were generated in cadaveric porcine IVDs using nitrogen gas introduced into the annulus fibrosus (AF) via 20G and 16 G catheters. Drops of Toluene Blue dye were injected into the catheter tubes, followed by the nitrogen gas at pressures of 172 kPa, 345 kPa, 690 kPa, 1000 kPa, 1400 kPa, 2000 kPa and 2400 kPa. Each injured IVD was then sectioned and visually inspected (Figure1).

Results

Accurate insertion of catheters into the antero-lateral aspect of the discs was achieved, except for two instances where the catheter came to rest in the nucleus pulposus-AF interface. The use of catheters did minimize puncture damage to tissue, however, on occasion at higher pressures, the compressed gas made its way outside of the IVD creating bubbles at the endplates and adjacent tissues.

Onset of injury could be seen at 690 kPa, with the relative size of IDD increasing until reaching a plateau around 1000 kPa, after which, little change in the relative size of injury was observed at increasing pressures. Hyper-intensely dyed areas following gas injection have been assumed to be the boundaries of the induced annular injury.

The catheter gauge had an observable affect on the size of injury generated at a given pressure. At lower pressures the 20G catheter generated larger injuries than the16G, however, after 1400 kPa, the 16G catheter created much larger annular disruptions, the largest being 1.55cm at ~1400 kPa.

Conclusions

As shown by Oliphant *et al*, using catheters to inject compressed air into the AF will induce annular disruptions and minimize injury to the rest of the IVD. μ-CT with contrast dye will also be used in the near future to further characterize the injury generated using this protocol.

References

Oliphant *et al.*, in press

Figure1. Injury at 690 kPa

Introduction:

The objective of this study is the validation of *Oliphant et al*'s injury method of generating highly user-defined intervertebral disc (IVD) injuries of various magnitudes (Oliphant, et al. 2005). Visual and μ-CT inspection will be used to visualize these injuries, which will be generated in porcine IVDs. By characterizing the path and magnitude of the injury created by this new protocol, it is expected that its future utilization will enable the development of new imaging techniques, which will focus on the detection of lower grade IVD injuries.

In humans the IVD acts as a shock absorber between the vertebral units and facilitates movement of the spine. The basic structure of the IVD is that of a high pressured gelatinous core called the nucleus pulposus (NP) contained by radial sheets of fibre (lamellae) of the annulus fibrosus (AF) (Cassidy, et al. 1989 ; Marchand and Ahmed 1990). Injury to the IVD has been identified as a major contributor to the presence of lower back pain (Kakitsubata, et al. 2003 ; Munter, et al. 2002 ; Yu, et al. 2003). These injuries manifest themselves in a variety of ways such as radial, circumferential, and transverse tears of the AF, and the type, size and location of these injuries can have a considerable impact on the presence of pain (Munter, et al. 2002). Currently clinicians are dependent on the visualization of IVD injury to associate the onset of pain with IVD damage. Unfortunately, detection is often dependent on injuries communicating with the NP, or the outside of the IVD. Yet, it has been hypothesized that asymptomatic low grade injuries may develop into these larger detectable symptomatic injuries (Fujita, et al. 1997).

Attempts to reproduce IVD injuries through various models have met with difficulties in controlling injury location and magnitude, as well as minimizing damage from external access to injury site (Oliphant, et al. 2005). *Masuda et al*, were able to generate reproducible IVD degeneration, measured in disc height and magnetic resonance imaging (MRI) grade by using 16GA - 21GA needles to puncture the AF (Masuda, et al. 2005). Degeneration results can not be used to infer acute and asymptomatic disruptions; however, the major success of this study was the limited damage the external initiation of

injury caused in comparison to the classic stab model, which was conducted as a comparison. The injury method investigated in this current study, goes a step further by utilizing compressed gas to generate graded Internal Disc Disruptions once the catheters are in the AF.

Internal Disc Disruption (IDD) has been described as being a disruption of the internal architecture of the disc without a change in the external shape (Crock 1986). Fissures in the inner third of the AF are rarely associated with pain until they propagate to the outer third of the annulus (Aprill and Bogduk 1992). *Oliphant et al* created an injury protocol that generates IDDs using compressed gas introduced into the AF via a 20G catheter. Injury visualization was accomplished using Gadolinium dye in MRI, showing different levels of dye propagation with increasing gas injection pressures (Fig. 1). Visual inspection was also performed using ink. It was acknowledged by this research team that the calculated gas density in the disc could not be equated to an anatomical injury.

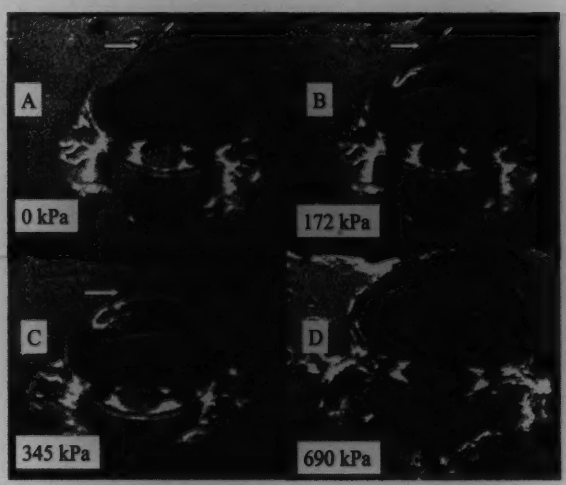

Figure1. MRI inspection results from *Oliphant et al* **(Oliphant, et al. 2005)**

Materials and Method:

Visual Inspection

As prescribed by *Oliphant et al*, porcine lumbar spine segments were harvested and refrigerated at approximately -20° C (Oliphant, et al. 2005). Before use, spine segment were thawed for a minimum of 24hrs, followed by the removal of all surface tissue on the anterior and antero-lateral aspect of the discs. The catheters used to generate the IDD injuries were the 20GA 1.16IN BD Insyte-W (Becton Dickson, Oakville, ON, Canada), and the 16GA 65mm Puncture Needle (MRI Devices Daum GmBH, Waukesha, WI, USA). A catheter was inserted through the anterior IVD tissue, with the needle point coming to rest in the antero-lateral aspect of the disc. Once in position, the needle was removed leaving the catheter in place. Aqueous Toluene Blue dye was then injected into the free end of the catheter tube until the reservoir at the end of the catheter was full or there was no more movement of dye into the catheter. The catheter was then connected to polyethylene tubing (Cook Canada, Stouffville, ON, Canada) via leur locks, which was in tern attached to the pressure regulator of a compressed nitrogen gas tank.

Using the pressure regulator, the compressed nitrogen gas was ramped to a final pressure of 690kPa over a minute, and maintained for an additional minute. Prior to catheter removal, the polyethylene tubing was detached, and more dye was injected into the catheter. The polyethylene tubing was then reattached and the pressure increased to approximately 20kPa, followed by the slow removal of the catheter. The injury generation procedure was repeated at pressures of 1000kPa, 1400kPa, 2000kPa and 2400kPa. The pressure used on each IVD injury was identified by a coloured marker imbedded in tissue adjacent to the disc. Both catheters were used to generate injuries at each pressure, creating 10 injuries in total. Both catheters were reused over the course of a day.

Following injury generation, the lumbar spine segment was refrigerated at approximately -20° C. Once frozen, the discs were sectioned axially through the centre, and then inspected visually. A machinist ruler was used to measure the distance from catheter insertion site to the top and bottom of hyper-intensely dyed region of the AF. The

difference between these two distances was defined as the relative size of injury, and the entire hyper-intensely dyed area was assumed to be the boundaries of the induced annular injury. If the initial sectioning revealed little damage, thinner slices would be taken using a scalpel until better injury visualization was achieved, or until it was obvious no visible injury was present.

μ-CT

In order to meet the sample dimension requirements for the vivaCT 40 (SCANCO MEDICAL, Southeastern, PA, USA) μ-CT unit, the porcine spinal columns had to be reduced to four individual vertebra–disc–vertebra units no larger than 38 mm in diameter. Once stripped of sufficient tissue using a band-saw and scalpel, the above injury protocol was performed. Only the 20GA catheters were used to generate these IDDs, and 300 mgI/mL Omnipaque Iodinated Contrast dye (Amersham Health, Oakville, ON, Canada), the same contrast dye as what is used for human discography, was used to achieve μ-CT injury visualization. Once the nitrogen gas was injected into the disc, the portion of the catheter protruding from the disc was cut off. Additional iodinated contrast dye was then injected into the remaining catheter tubing using a syringe with a 27GA needle. This procedure ensured catheter track visualization. Pressures of 180kPa, 690kPa, 1000kPa, and 2000kPa were used to generate the injuries.

Once the injury was generated and the protruding catheter tubing removed, the disc sample was loaded into the μ-CT sample rig, and then the rig was placed into the vivaCT 40 bore. The injured disc segments were imaged with high resolution scans at 55KeV and 72μA. The vivaCT 40 proprietor and ImageJ software (http://rsb.info.nih.gov/ij/) were used for injury visualization.

Results:

Visual Inspection

Accurate insertion of catheter into the antero-lateral aspect of the IVD was achieved, except for two instances where the catheter came to rest in the NP-AF interface. The use of catheters did minimize puncture damage to tissue, however, on occasion at higher pressures, the compressed gas made its way outside of the IVD creating bubbles at the endplates and adjacent tissues.

Onset of injury could be seen at 690kPa, with the relative size of IDD increasing until reaching a plateau at approximately 1000kPa, after which, little change in the relative size of injury was observed at increasing pressures (Fig. 2). As described, the relative size of injury is defined as the approximate distance between the top and bottom of a hyper-intensely dyed region of the AF.

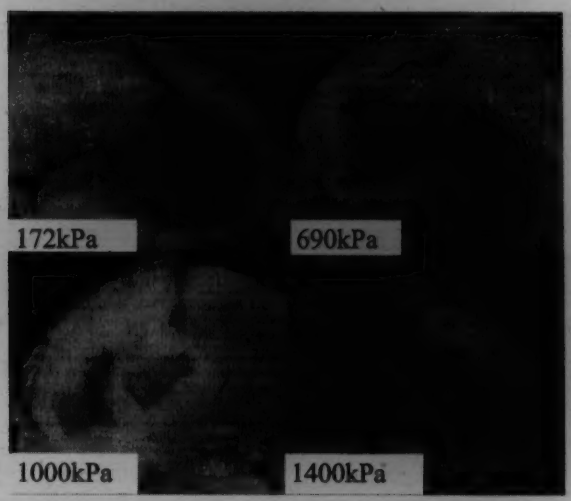

Figure2. Visual inspection results

Table1. Approximate size of injury (cm)					
20GA catheter		16GA catheter		16GA catheter thin sections	
Right Section		Right Section		Right Section	
690kPa	0.1588	690kPa	0.1587	690kPa	--
[redacted]	0.7541	[redacted]	--	[redacted]	--
[redacted]	0.6351	[redacted]	0.4365	[redacted]	1.5478
[redacted]	0.8335	[redacted]	0.0397	[redacted]	--
[redacted]	0.9525	[redacted]	0.6350	[redacted]	1.0319
Left Section		Left Section		Left Section	
690kPa	0.5953	690kPa	0.0794	690kPa	--
[redacted]	0.9922	[redacted]	0.3175	[redacted]	0.1984
[redacted]	1.0716	[redacted]	0.3175	[redacted]	--
[redacted]	0.5953	[redacted]	0.1588	[redacted]	1.0506
[redacted]	--	[redacted]	--	[redacted]	--

Catheter gauge seemed to have had an affect on the size of injury generated at a given pressure. At lower pressures the 20GA catheter generated larger injuries than the16GA, however, after 1400kPa, the 16G catheter created much larger annular disruptions, the largest being 1.55cm at ~14000kPa. Table 1 displays the approximate size of injury in each of the disc sections for each injection pressure, and Figure 3 gives a graphical display of the data. The absence of data indicates that no definable injury was detected or that no additional sectioning was required.

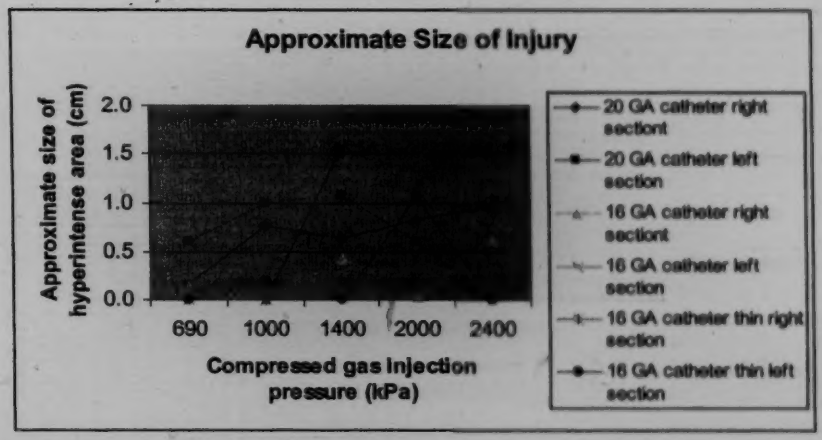

Figure3. Approximate Size of Injury (cm)

μ-CT inspection

Accurate insertion of the catheter into the antero-lateral aspect of the disc was achieved, except for one instance where the catheter was redirected by the endplate into the NP.

No injury was detected, despite catheter visualization, at 180kPa and 690kPa. At 1000kPa a large cylindrical circumferential disruption was visualized (Fig.4), but unfortunately, due to the Field of View (FOV) selection of this particular scan, no catheter track can be seen, and therefore onset of injury. The injury generated at 2000kPa was isolated to the NP, resulting in its partial delineation. Due to threshold and FOV parameters, it is hard to confidently report on the size of injury seen at 1000kPa using μ-CT.

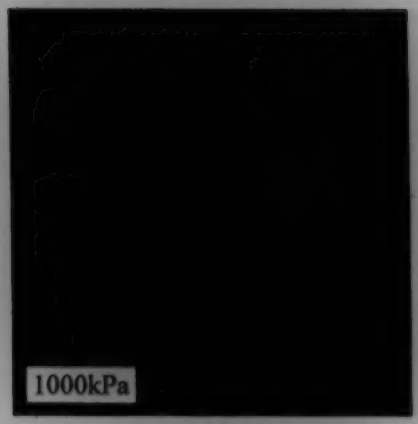

Figure4. μ – CT inspection results

Discussion:

General Comments

The use of non-compressible (liquid dye) and compressible fluids (nitrogen gas) to generate annular injury leaves some questions as to the actual existence of inter-laminar separation. The dye could just be diffusing through the biological material, which is one of the functions of the AF; the size of the hyper-intensely dyed area being a function of anisotropic and isotropic diffusion. However, there is some definite annular separation observed at 690kPa (Fig. 2), and there were also a number of injuries that crossed multiple lamellae, propagating anterior to posterior.

For unknown reasons, initial dye movement from the catheter reservoir would change depending on the type of dye being used. The injection pressure would also affect the initial movement of dye from the reservoir. *Oliphant et al.* saw Gadolinium in the discs at 172kPa with T1-weighted MRI, however, no dye movement was observed until approximately 690kPa for all but one injury using Toluene Blue (Oliphant, et al. 2005). Using Iodinated Contrast dye, movement was seen at 172kPa in one instance, and then 500kPa in another. The viscosity of the dyes may have had an influence on the fluids' ability to cleave the annular layers, or as will be discussed shortly, the morphology of the AF and its viscoelastic response to perturbations in the IVD may explain the varied resistances to flow observed.

Considering the highly pressurized NP contained by the lamellar layers of the AF, the circumferential tendencies of the injuries generated is not surprising. Following the path of least resistance, the gas and dye was most likely guided between the pressure front of the NP and the pressure equalizing layers of the AF. The insertion angle of the catheters may also have had a considerable impact on the general geometry of the injuries. The initial pneumatic force vectors' orientation was closer to parallel with the lamellar fibers than perpendicular, limiting the opportunity for radial failures to occur.

While the injuries generally followed the curvature of the annular layers, further investigation into the micro-structure of the lamellar fibres offers some explanation as to why some injuries propagated anterior-posterior, or a combination of anterior-posterior and circumferential. As reported by *Marchand et al*, lamellar fibres are a combination of oval fibre bundles and a gelatinous ground substance; similar to bricks and mortar (Marchand and Ahmed 1990). These layers are often incomplete, ending abruptly between two adjacent layers, or splitting an existing layer causing it to fork. Also, a given layer may not extend from endplate to endplate. Considering this morphology, there are many potential failure points between annular layers, and within individual lamellae. Reaching the proper fault point may have allowed injuries to propagate across multiple lamellae or branch into adjacent lamellar boundaries.

The catheter gauge, depth of penetration, as well as the injection pressure seemed to have had an affect on the injury observed. The viscoelastic properties of the IVD must enable constant response to pressures that vary throughout the day (Wilke, et al. 1999). In regards to the 16GA catheter, a perturbation to the system, in the form of a larger catheter, may have garnered a stronger pressure equalization response from the AF. As well, the depth of penetration for the 16GA catheters was a few millimeters less than the 20GA, potentially leaving its catheter tip suspended in an increasingly well defined portion of the AF (Fujita, et al. 1997 ; Marchand and Ahmed 1990). The relative size of injury given increasing pressures further supports the possibility of the AF aggressively responding to large perturbations in the IVD. Graded injuries were still observed, but, as

shown by this study, the size of injury has the potential to plateau. Another potential explanation for the injury size plateau is that the injection pressures were increased caudally with the IVDs (Oliphant, et al. 2005).

Visual Inspection

The injuries observed through visual inspection on either side of the axial sections were not always symmetrical, suggesting that the boundaries of the gross injury were not continuous over the entire height of the disc. Catheter tip placement was not always directly in the middle plane of the IVD, and would sometimes tract closer to one endplate. The use of a cryostat would have increased the confidence of the injury dimensions reported; however, for the scope of this study additional scalpel sectioning was performed when deemed necessary.

μ-CT

The inclusion of μ-CT visualization into this study was a late addition. To date, there has been limited time to determine the best imaging parameters for injury visualization, and the images displayed from μ-CT are highly dependent on post-processing. Considering Figure 3, the general length and curvature of the injury is similar to what is observed with visual inspection, however, the radial thickness of the injury is much larger than what has been observed. The current thresh-hold parameters most likely pick up the presence of any iodinated contrast dye at a relative concentration, so it may be hard to separate highly concentrated areas (annular fissure) with lower baseline levels (diffused contrast in the ground substance, or micro-tears through lamellae).

The injury seen in Figure 3 was scanned with a limited FOV due to scan time availability. For future scans, the length of the catheter and entire lateral portion of the disc will be selected, since the image of this injury is clearly truncated.

Conclusion:

In a study by *Kakisubata et al*, randomly acquired IVDs from thoracic and lumbar cadaveric spine segments had circumferential injuries comprising a third of the total numbers of disc failures detected through gross anatomicalal inspection (Kakitsubata, et al. 2003). Out of this group, circumferential injuries were found to have the lowest MR imaging and MR discogram detection percentages (21%). Considering this, *Oliphant et al*'s injury protocol ***does*** produces a clinically relevant injury, which is frequently present in IVDs, yet at this moment, confounds established clinical imaging techniques.

The original MRI results from *Oliphant et al* in addition to the visual inspection and micro-ct results from this study, still haven't fully characterized the injury generated using this protocol. However, this study has shown that indeed a graded injury is possible with minimal damage to other areas of the IVD.

With this injury method, and the new interest concerning the detection of inter-laminar separation and matrix failure between the lamellae, there may be an opportunity to re-open the debate regarding the clinical relevance of IVD injury mechanisms and the causes of lower back pain (Fujita, et al. 1997 ; Videman, et al. 2003 ; Videman and Nurminen 2004).

References:

Aprill C, Bogduk N. 1992. High-intensity zone: a diagnostic sign of painful lumbar disc on magnetic resonance imaging. Br J Radiol 65:361-369.

Cassidy JJ, Hiltner A, Baer E. 1989. Hierarchical structure of the intervertebral disc. Connect Tissue Res 23:75-88.

Crock HV. 1986. Internal disc disruption. A challenge to disc prolapse fifty years on. Spine 11:650-653.

Fujita Y, Duncan NA, Lotz JC. 1997. Radial tensile properties of the lumbar annulus fibrosus are site and degeneration dependent. J Orthop Res 15:814-819.

Kakitsubata Y, Theodorou DJ, Theodorou SJ, Trudell D, Clopton PL, Donich AS, Lektrakul N, Resnick D. 2003. Magnetic resonance discography in cadavers: tears of the annulus fibrosus. Clin Orthop Relat Res (407):228-240.

Marchand F, Ahmed AM. 1990. Investigation of the laminate structure of lumbar disc anulus fibrosus. Spine 15:402-410.

Masuda K, Aota Y, Muehleman C, Imai Y, Okuma M, Thonar EJ, Andersson GB, An HS. 2005. A novel rabbit model of mild, reproducible disc degeneration by an anulus needle puncture: Correlation between the degree of disc injury and radiological and histological appearances of disc degeneration. Spine 30:5-14.

Munter FM, Wasserman BA, Wu HM, Yousem DM. 2002. Serial MR Imaging of Annular Tears in Lumbar Intervertebral Disks. AJNR Am J Neuroradiol 23:1105-1109.

Oliphant D, Frayne R, Kawchuk G. 2005. A new method of creating intervertebral disc disruption of various grades. Clin Biomech (Bristol, Avon)

Videman T, Battie MC, Gibbons LE, Maravilla K, Manninen H, Kaprio J. 2003. Associations between back pain history and lumbar MRI findings. Spine 28:582-588.

Videman T, Nurminen M. 2004. The occurrence of anular tears and their relation to lifetime back pain history: a cadaveric study using barium sulfate discography. Spine 29:2668-2676.

Wilke HJ, Neef P, Caimi M, Hoogland T, Claes LE. 1999. New in vivo measurements of pressures in the intervertebral disc in daily life. Spine 24:755-762.

Yu CY, Tsai KH, Hu WP, Lin RM, Song HW, Chang GL. 2003. Geometric and morphological changes of the intervertebral disc under fatigue testing. Clin Biomech (Bristol, Avon) 18:S3-9.

Appendix C: Experimental and Imaging Protocols

SWINE _ EXPERIMENTAL PROTOCOL

Time

Temperature @ section_____°C

Wrap and Pot spines

Calibrate pressure sensor (830N)_____kPa

Generate injuries (2mm control – left – right, 12GA c – r – l, head to toe)

Drill hole in last disc for thermometer introduction

Temperature @ injury_____°C

Cover 2mm's with surgical tape

Load cell to back pots all the way into rig

Mark distance with pencil

Temperature @ pre-imaging _____°C

Imaging protocol (no load)!!!!!!

Temperature @ pre-load _____°C

Imaging protocol (load)!!!!!!!

Temperature @ post-load_____°C

Mark distance with pencil

Load cell ____V, Pressure sensor _____ kPa

Back-up rig and measure distance _____mm

Recover beads, and inject dye into injuries

SWINE _ IMAGING PROTOCOL

NO LOAD time, kPa

Localizer

Localizer (true loc) ** check localizers for artifacts

HiresAxT2 Coronal

Localizer (axial) ** pop off beads if present

DTI

DTI

AxT2M (increase slice position in phase direction: H...+1mm)

T2_tse_ax

HiResAxT2 TE103

HiResAxT2 TE15

T2_tse_sag (adjust using true loc)

SWINE EXPERIMENT PROTOCOL

LOAD (830N = ... kPa, wait till stabilizes over 3mins, 1min to ramp)

Localizer (true loc)

HiresAxT2 Coronal

Localizer (ax)

DTI

AxT2M (increase slice position in phase direction +1mm)

T2_tse_ax

HiResAxT2 TE103

HiResAxT2 TE15

T2_tse_sag (adjust using true loc)

Appendix D: Example of Results from Imaging Protocol of One IVD

Image catalogue:

1) b0 and 6 DWIs "on" slice (raw data used to generate DTI maps)

2) 2mm core "on" slice, DTI threshold of 60 SI

3) 2mm core "off" slice, DTI threshold of 76 SI

4) 12GA stab "on" slice, DTI threshold of 60 SI

5) 12GA stab "off" slice, DTI threshold of 76 SI

Note:

* SI measurements in image captions refer **ONLY** to top row (no load condition)

b0	DW1	DW2	DW3	DW4	DW5	DW6
(0, 0, 0)	(1, 0, 1)	(-1, 0, 1)	(0, 1, 1)	(0, 1, -1)	(1,1, 0)	(-1, 1, 0)

Figure D1. Unprocessed b0 and 6 DWI "on" slice from DTI sequence, no load (top row) and load (bottom row) conditions.

Figure D2. 2mm core "on" slice, no load (top row) and load (bottom row) conditions. 2mm injury 89 SI, normal AF 55 SI, DTI threshold of 60 SI.

Clin. AxT2 HiResAx T2 TraceADC Eigenvalue 1 Eigenvalue 2 Eigenvalue 3 FA Clin. SagT2

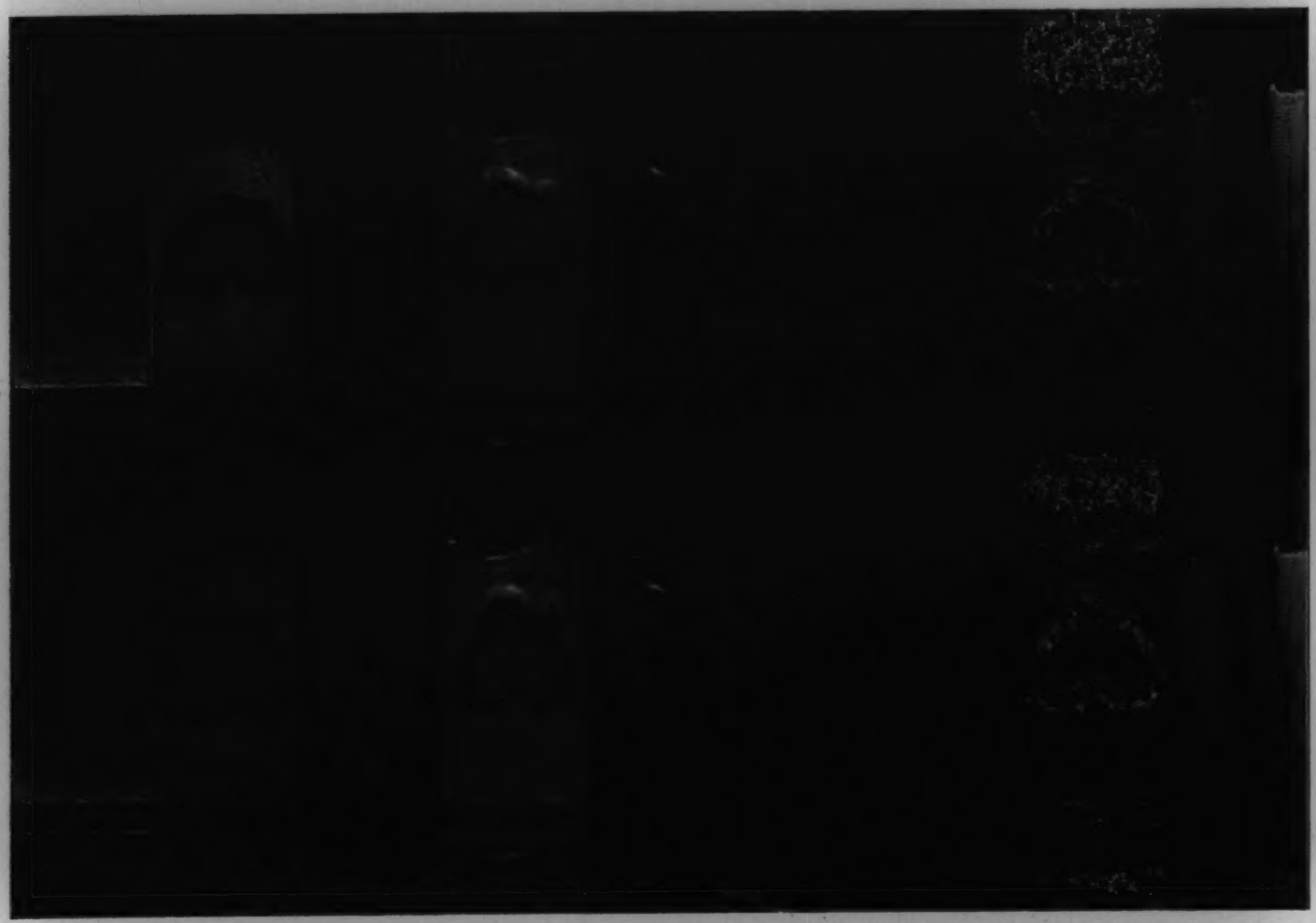

Figure D3. 2mm core "off" slice, no load (top row) and load (bottom row) conditions. 2mm injury 133 SI, normal AF 66 SI, DTI threshold of 76 SI.

Figure D4. 12GA stab "on" slice, no load (top row) and load (bottom row) conditions. 12GA injury 77 SI, normal AF 55 SI, DTI threshold of 60 SI.

Clin. AxT2 HiResAx T2 TraceADC Eigenvalue 1 Eigenvalue 2 Eigenvalue 3 FA Clin. SagT2

Figure D5. 12GA stab "off" slice, no load (top row) and load (bottom row) conditions. 12GA injury 91 SI, normal AF 67 SI, DTI threshold of 76 SI.

Appendix E: Final Results ("on" slices) from Imaging Protocol of 2mm core and 12GA stab injuries

Image catalogue:

1-11) 2mm core visualization, "on" slices, no load and load conditions

12-22) 12GA stab visualization, "on" slices, no load and load conditions

Note:

* White arrow indicates both injury detection and injury position
* Positive DTI injury visualization indicated by arrow on TraceADC map
* SI measurements in image captions refer **ONLY** to top row (no load condition)

Figure E1. 2mm core "on" slice, no load (top row) and load (bottom row) conditions. 2mm injury 151 SI, normal AF 54 SI, DTI threshold 120 SI.

Figure E2. 2mm core "on" slice, no load (top row) and load (bottom row) conditions. 2mm injury 81 SI, normal AF 57 SI, DTI threshold of 67 SI.

Clin. AxT2 HiResAx T2 Proton Density TraceADC Eigenvalue 1 Eigenvalue 2 Eigenvalue 3 FA Clin. SagT2

Figure E3. 2mm core "on" slice, no load (top row) and load (bottom row) conditions. 2mm injury 140 SI, normal AF 55 SI, DTI threshold of 120 SI.

Figure E4. 2mm core "on" slice, no load (top row) and load (bottom row) conditions. 2mm injury 118 SI, normal AF 60 SI, DTI threshold of 100 SI.

Clin. AxT2 HiResAx T2 Proton Density TraceADC Eigenvalue 1 Eigenvalue 2 Eigenvalue 3 FA Clin. SagT2

Figure E5. 2mm core "on" slice, no load (top row) and load (bottom row) conditions. 2mm injury 107 SI, normal AF 61 SI, DTI threshold of 100 SI.

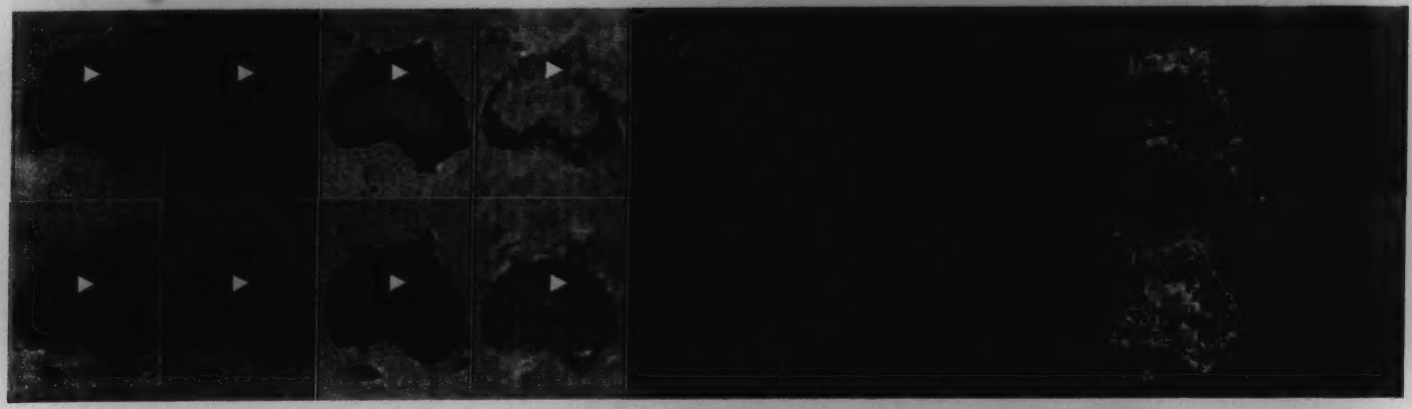

Figure E6. 2mm core "on" slice, no load (top row) and load (bottom row) conditions. 2mm injury 227 SI, normal AF 65 SI, DTI threshold of 75 SI.

Clin. AxT2 HiResAx T2 Proton Density TraceADC Eigenvalue 1 Eigenvalue 2 Eigenvalue 3 FA Clin. SagT2

Figure E7. 2mm core "on" slice, no load (top row) and load (bottom row) conditions. 2mm injury 86 SI, normal AF 85 SI, DTI threshold of 76 SI.

Figure E8. 2mm core "on" slice, no load (top row) and load (bottom row) conditions. 2mm injury 123 SI, normal AF 58 SI, DTI threshold of 100 SI.

Figure E9. 2mm core "on" slice, no load (top row) and load (bottom row) conditions. 2mm injury 89 SI, normal AF 55 SI, DTI threshold of 60 SI.

Figure E10. 2mm core "on" slice, no load (top row) and load (bottom row) conditions. No 2mm injury, normal AF 55 SI, DTI threshold of 85 SI.

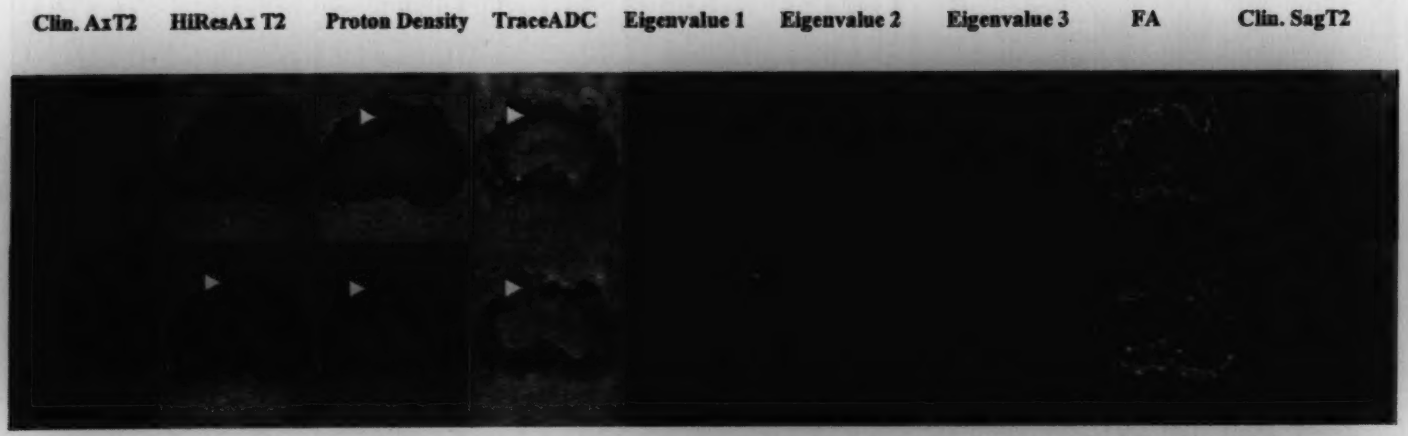

Figure E11. 2mm core "on" slice, no load (top row) and load (bottom row) conditions. 2mm injury 115SI, normal AF 83 SI, DTI threshold of 65 SI.

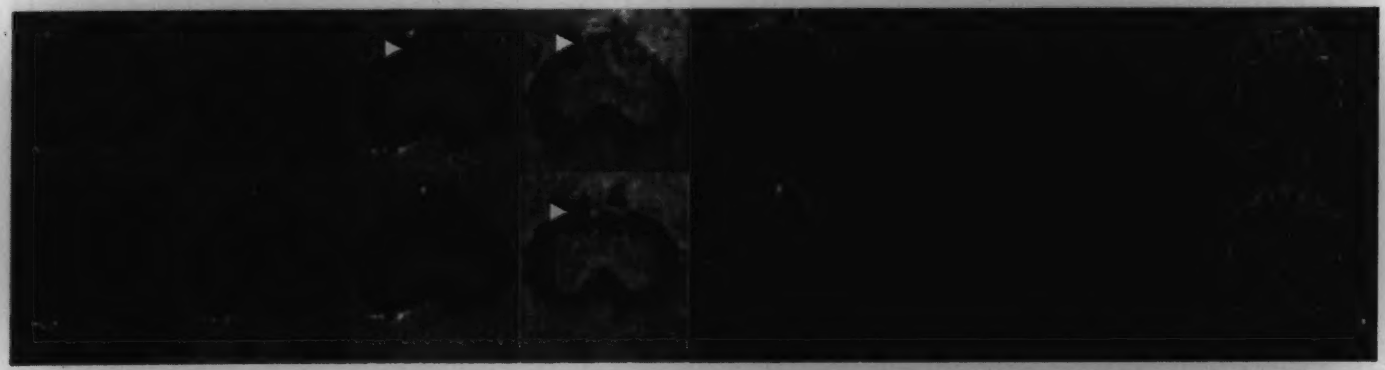

Figure E12. 12GA stab "on" slice, no load (top row) and load (bottom row) conditions. 12GA stab injury 143 SI, normal AF 54 SI, DTI threshold 127 SI.

Figure E13. 12GA stab "on" slice, no load (top row) and load (bottom row) conditions. No 12GA stab injury, normal AF 57 SI, DTI threshold 67 SI.

Clin. AxT2 HiResAx T2 Proton Density TraceADC Eigenvalue 1 Eigenvalue 2 Eigenvalue 3 FA

Figure E14. 12GA stab "on" slice, no load (top row) and load (bottom row) conditions. 12GA stab injury 161 SI, normal AF 55 SI, DTI threshold 99 SI.

Figure E15. 12GA stab "on" slice, no load (top row) and load (bottom row) conditions. 12GA stab injury 68 SI, normal AF 60 SI, DTI threshold 85 SI.

Clin. AxT2 HiResAx T2 Proton Density TraceADC Eigenvalue 1 Eigenvalue 2 Eigenvalue 3 FA

Figure E16. 12GA stab "on" slice, no load (top row) and load (bottom row) conditions. 12 GA injury 73 SI, normal AF 61 SI, DTI threshold of 55 SI.

Figure E17. 12GA stab "on" slice, no load (top row) and load (bottom row) conditions. No 12GA injury, normal AF 64 SI, DTI threshold of 72 SI.

Clin. AxT2 HiResAx T2 Proton Density TraceADC Eigenvalue 1 Eigenvalue 2 Eigenvalue 3 FA

Figure E18. 12GA stab "on" slice, no load (top row) and load (bottom row) conditions. No 12GA injury, normal AF 85 SI, DTI threshold of 76 SI.

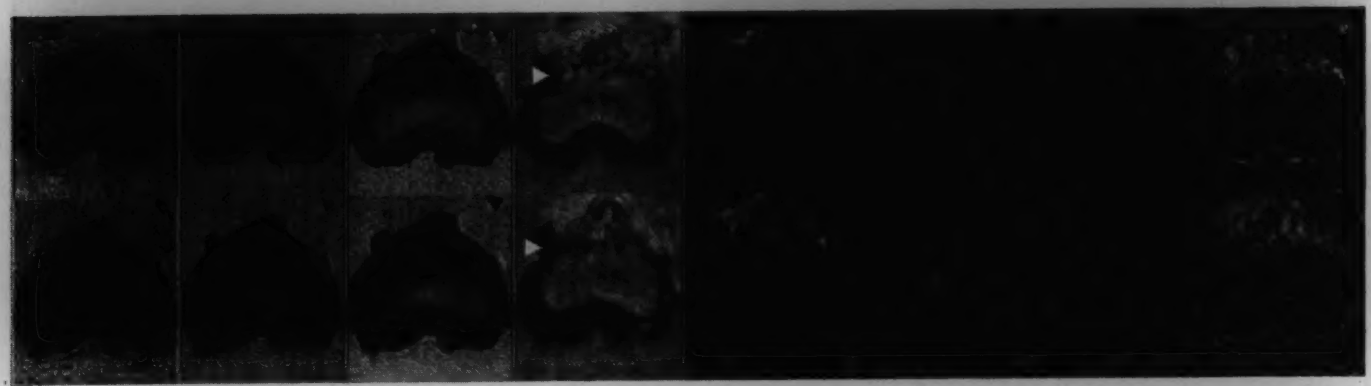

Figure E19. 12GA stab "on" slice, no load (top row) and load (bottom row) conditions. 12GA injury 123 SI, normal AF 58 SI, DTI threshold 115 SI.

Clin. AxT2 HiResAx T2 Proton Density TraceADC Eigenvalue 1 Eigenvalue 2 Eigenvalue 3 FA

Figure E20. 12GA stab "on" slice, no load (top row) and load (bottom row) conditions. 12GA injury 77 SI, normal AF 55 SI, DTI threshold 64 SI.

Figure E21. 12GA stab "on" slice, no load (top row) and load (bottom row) conditions. 12GA injury 150 SI, normal AF 55 SI, DTI threshold of 131 SI.

Clin. AxT2 HiResAx T2 Proton Density TraceADC Eigenvalue 1 Eigenvalue 2 Eigenvalue 3 FA Clin. SagT2

Figure E22. 12GA stab "on" slice, no load (top row) and load (bottom row) conditions. 12GA injury 93 SI, normal AF 82 SI, DTI threshold of 67 SI.

Appendix F: Diffusion Weighting Contrast to Noise Measurements of the IVD

Diffusion weighting of IVD:

The raw SI data from each of the six diffusion gradient directions that generate the DTI maps (Table 1) confirmed the diffusion weighting of the 2 injuries, the NP and AF tissues. A graphical description of the extent of diffusion weighting for each ROI during the no load and load conditions can be seen in Figures 1 and 2.

	b0 (0, 0, 0)	DW1 (1, 0, 1)	DW2 (-1, 0, 1)	DW3 (0, 1, 1)	DW4 (0, 1, -1)	DW5 (1, 1, 0)	DW6 (-1, 1, 0)
[illegible]							
Mean	110.6	75.8	77.6	87.5	85.6	84.9	78.2
Stnd. Error	9.8	4.6	5.3	8	6.4	7.4	6.3
N = 17							
[illegible]							
Mean	104.2	68.3	69.5	77.7	73.9	80.2	79.1
Stnd. Error	9.8	6.5	4.3	6.6	6.2	3.9	6.2
N = 14							
[illegible]							
Mean	63.9	54.2	54.5	53.3	55.1	59.7	55.8
Stnd. Error	2.9	2.1	1.8	1.6	2	2.1	2
N = 21							
[illegible]							
Mean	478.6	271.4	278.1	275.1	256.2	271.3	275.1
Stnd. Error	26.1	14.6	14.5	14.2	15.1	15	15.1
N = 22							

Table F1. SI intensity means (no load, and with compressive loading) from the 2 injuries, AF and NP tissue ROIs for b0 and each of the 6 diffusion gradient directions.

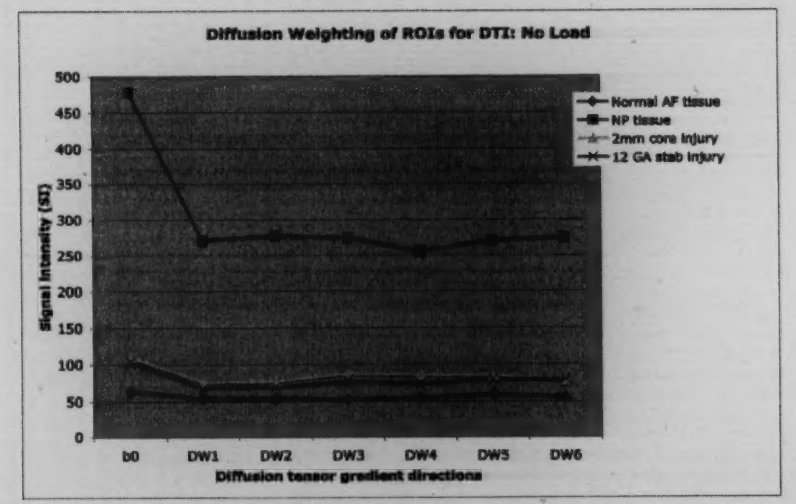

Figure F1. Diffusion weighting of IVD in six gradient directions for DTI.

	b0	DW1	DW2	DW3	DW4	DW5	DW6
[illegible]							
Mean	110.3	75.3	73.7	79	74.3	81.7	79.8
Stnd. Error	5.9	4	3.8	3.9	3.6	3	3.4
N = 22							
[illegible]							
Mean	101.3	65.9	65.9	70	71.8	73.4	73.1
Stnd. Error	7.7	3.8	3.8	4.5	3.9	5	3.8
N = 16							
[illegible]							
Mean	64.6	56.1	52.8	57.3	56.8	56	56.3
Stnd. Error	2.4	2.1	1.5	2.4	2.2	1.9	2
N = 22							
[illegible]							
Mean	460.2	261.5	270.1	263.3	250.9	259.7	266.5
Stnd. Error	27.9	16.2	16.4	16.5	15.5	15.8	15.9
N = 17							

Table F2. SI means from the 2 injuries during compressive loading, AF and NP tissue ROIs for b0 and each of the 6 diffusion gradient directions.

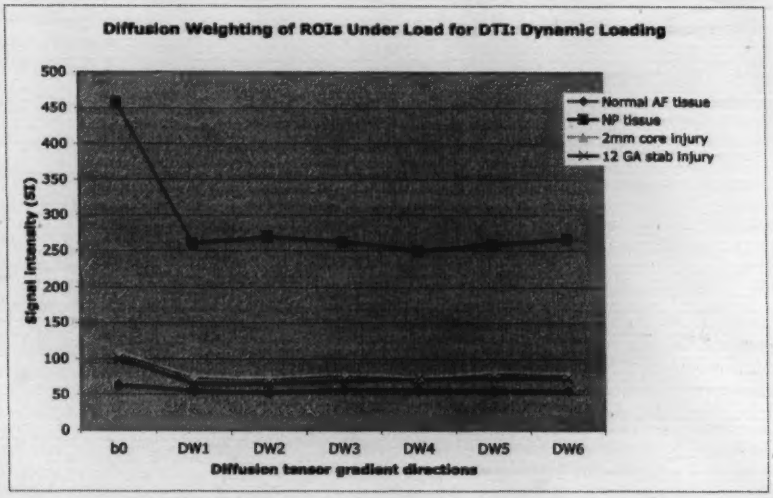

Figure F2. Diffusion weighting of IVD under dynamic loading in six gradient directions for DTI.

Contrast to noise (CNR) of IVD ROIs:

Because normal AF tissue does not consistently provide good SNR for MRI visualization (under 10 for this experiment), it was decided that the NP, which is well visualized and traditionally has good SNR (over 50 for this experiment), would be used as a standard to quantitatively compare the SI changes in the 2mm core and 12 GA stab injuries with diffusion weighting. The CNR values for b0 and the six diffusion gradients can be found for both the 2mm core and 12 GA stab injuries in Tables 2 and 3. A graphical representation of the average values can be viewed in Figure 3 and 4.

	CNR b0	CNR DW1	CNR DW2	CNR DW3	CNR DW4	CNR DW5	CNR DW6
Std Error	3.9	2.1	2.0	2.0	2.0	2.2	2.2
Minimum	9.5	2.6	3.5	4.2	4.6	3.6	5.1

Table F3. Descriptive statistics for CNR between NP and 2mm core injury at DTI diffusion gradients.

	CNR b0	CNR DW1	CNR DW2	CNR DW3	CNR DW4	CNR DW5	CNR DW6
Std Error	4.4	2.5	2.5	2.5	2.4	2.6	2.4
Minimum	11.6	5.4	4.0	3.3	4.2	2.5	6.0

Table F4. Descriptive statistics for CNR between NP and 12 GA stab injury at DTI diffusion gradients.

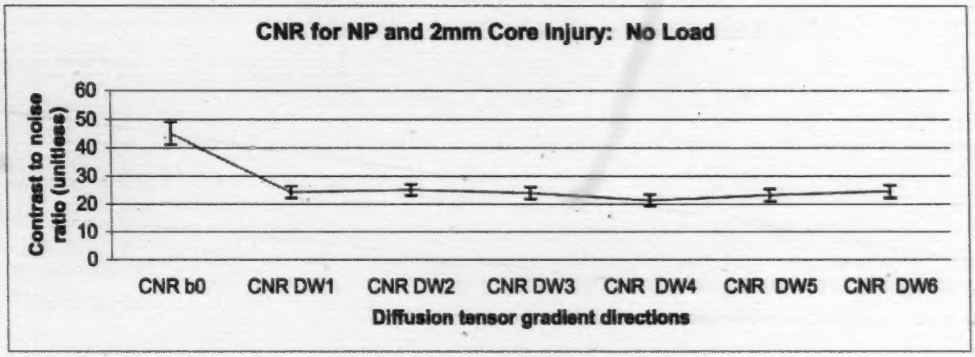

Figure F3. CNR for NP and 2mm core with standard error bars, at DTI diffusion gradients.

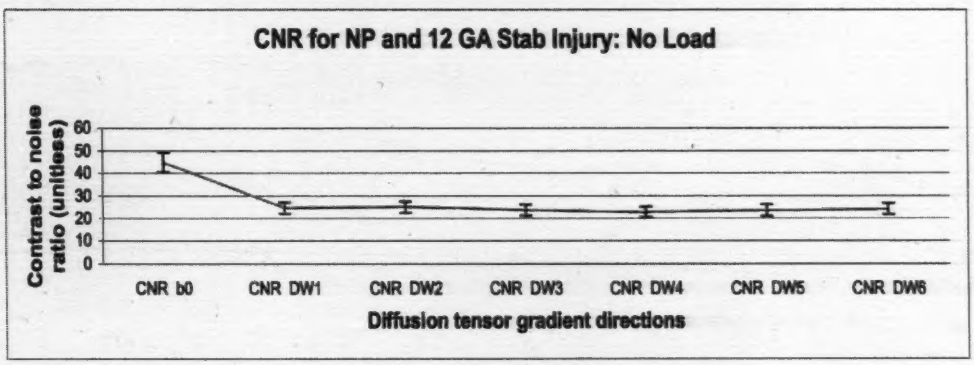

Figure F4. CNR for NP and 12 GA stab with standard error bars, at DTI diffusion gradients.

Dynamic Loading:

While loading slightly reduced the contrast between the NP and 2mm core injury, a general increase in contrast between the NP and 12 GA stab was observed (see Tables 4 and 5, and Figures 5 and 6).

CNR NP to 2mm core with load							
	CNR b0	CNR DW1	CNR DW2	CNR DW3	CNR DW4	CNR DW5	CNR DW6
Mean	41.5	23.2	24.5	23.2	22.2	22.1	23.2
Std Error	3.4	2.0	2.0	2.0	1.8	2.0	1.9
Std Dev	10.1	7.2	7.0	7.0	6.6	7.2	6.7
Minimum	12.8	5.6	7.8	7.4	3.4	5.5	8.1
Maximum	55.2	37.3	37.0	37.2	35.3	35.1	37.9

Table F5. Descriptive statistics for CNR between NP and 2mm core injury at DTI diffusion gradients, under loading conditions.

CNR NP to 12 GA stab with load							
	CNR b0	CNR DW1	CNR DW2	CNR DW3	CNR DW4	CNR DW5	CNR DW6
Mean	42.6	25.0	26.2	25.1	25.0	25.6	25.4
Std Error	4.5	2.4	2.3	2.5	2.4	2.3	2.4
Std Dev	18.0	9.7	9.4	10.1	9.5	9.2	9.7
Minimum	10.8	5.8	10.8	7.7	2.9	5.9	8.4
Maximum	80.9	52.5	50.3	49.2	47.6	49.4	47.6

Table F6. Descriptive statistics for CNR between NP and 12 GA stab injury at DTI diffusion gradients, under loading conditions.

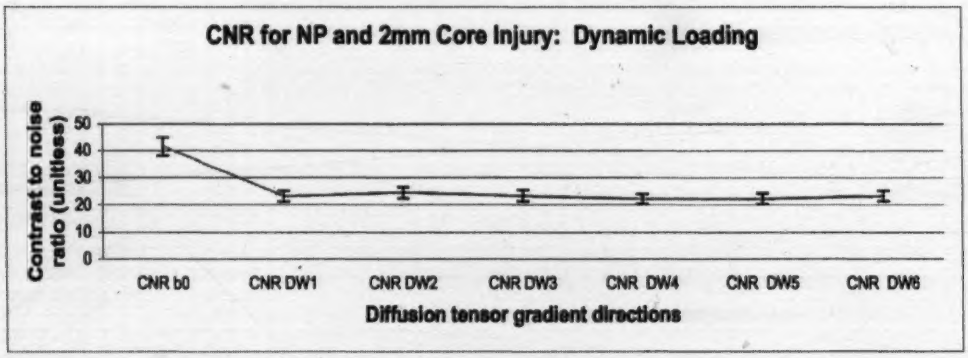

Figure F5. CNR for NP and 2mm core at DTI diffusion gradients under load, with standard error bars.

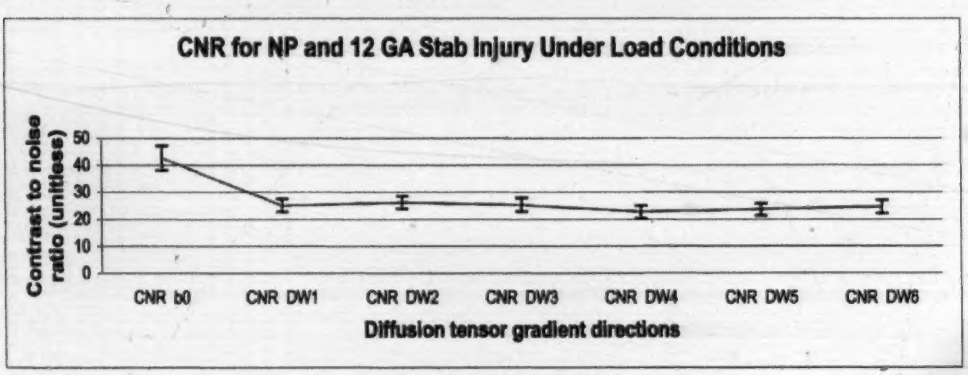

Figure F6. CNR for NP and 12 GA stab at DTI diffusion gradients under load, with standard error bars.

Appendix G: Statistical Considerations for Quantitative Analysis

Statistical Considerations for Quantitative Analysis:

Preliminary statistics showed that specimen was not a significant factor for any of the ROIs, and that IVD level was a factor for only the NP (see Table 1).

Specimen (x) Load MANOVA. A single * denotes specimen significance at alpha = 0.05					
	p – values				
ROI	TraceADC	Eigenvalue1	Eigenvalue2	Eigenvalue3	FA
2mm core	0.793	0.826	0.889	0.971	0.971
12 GA slab	0.862	0.36	0.51	0.19	0.165
NP	0.458	0.158	0.161	0.376	0.424
IVD Level (x) Load MANOVA. A single * denotes IVD level significance at alpha = 0.05					
	p – values				
ROI	TraceADC	Eigenvalue1	Eigenvalue2	Eigenvalue3	FA
2mm core	0.071	0.163	0.072	0.135	0.087
12 GA slab	0.335	0.345	0.493	0.599	0.663
NP	0.719	0.000*	0.097	0.109	0.003*

Table G1. Preliminary statistics indicating that specimen was a non-significant factor, and that IVD level was a significant factor for only the NP.

The presence of compressive loading did have an impact on the 2mm core injury. A specimen (x) load MANOVA of the 2mm core DTI data set, indicated significant differences for the TraceADC and eigenvalue 1 variables ($p = 0.035$ and 0.012). The same analysis on the other ROIs did not result in Load being identified as a significant factor. In the IVD level (x) load analysis, load was significant for only the eigenvalue 1 measure ($p = 0.015$) for the 2mm core. These results can be seen on Table 2.

Specimen (x) Load MANOVA. A single * denotes load significance at alpha = 0.05					
	p – values				
ROI	TraceADC	Eigenvalue1	Eigenvalue2	Eigenvalue3	FA
2mm core	0.035*	0.012*	0.072	0.096	0.25
[illegible]	[illegible]	[illegible]	[illegible]	[illegible]	[illegible]
NP	0.396	0.814	0.968	0.811	0.888
IVD Level (L) Load MANOVA. A single * denotes load significance at alpha = 0.05					
	p – values				
ROI	TraceADC	Eigenvalue1	Eigenvalue2	Eigenvalue3	FA
2mm core	0.061	0.015*	0.162	0.164	0.55
[illegible]	[illegible]	[illegible]	[illegible]	[illegible]	[illegible]
NP	0.609	0.818	0.488	0.455	0.521

Table G2. Preliminary statistics indicating that load was a significant factor for only the 2mm core injury, and then only for only one DTI measure.